



AFRL-OSR-VA-TR-2011-0405

**(MURI-05) DYNAMIC FLIGHT MANEUVERING USING
VIRTUAL CONTROL SURFACES GENERATED BY TRAPPED
VORTICITY**

Glezer, Ari,
Allen, Mark G.
Calise, Anthony J.
Leonard, Anthony
McMichael, James M.
Moser, Robert D.
Pearlstein, Arne J.

Georgia Institute of Technology, Atlanta GA
California Institute of Technology, Pasadena Ca
University of Texas at Austin, Austin TX
University of Illinois at Urbana-Champaign, Urbana-Champaign, Illinois

DECEMBER 2010
Final Report

DISTRIBUTION A: Distribution approved for public release.

**AIR FORCE RESEARCH LABORATORY
AF OFFICE OF SCIENTIFIC RESEARCH (AFOSR)/RSL
ARLINGTON, VIRGINIA 22203
AIR FORCE MATERIEL COMMAND**

Report Documentation Page			Form Approved OMB No. 0704-0188	
<p>Public reporting burden for the collection of information is estimated to average 1 hour per response, including the time for reviewing instructions, searching existing data sources, gathering and maintaining the data needed, and completing and reviewing the collection of information. Send comments regarding this burden estimate or any other aspect of this collection of information, including suggestions for reducing this burden, to Washington Headquarters Services, Directorate for Information Operations and Reports, 1215 Jefferson Davis Highway, Suite 1204, Arlington VA 22202-4302. Respondents should be aware that notwithstanding any other provision of law, no person shall be subject to a penalty for failing to comply with a collection of information if it does not display a currently valid OMB control number.</p>				
1. REPORT DATE 31 DEC 2010	2. REPORT TYPE	3. DATES COVERED 01-06-2005 to 30-09-2010		
4. TITLE AND SUBTITLE (MURI-05) Dynamic Flight Maneuvering Using Virtual Control Surfaces Generated By Trapped Vorticity			5a. CONTRACT NUMBER	
			5b. GRANT NUMBER	
			5c. PROGRAM ELEMENT NUMBER	
6. AUTHOR(S)			5d. PROJECT NUMBER	
			5e. TASK NUMBER	
			5f. WORK UNIT NUMBER	
7. PERFORMING ORGANIZATION NAME(S) AND ADDRESS(ES) Georgia Institute of Technology, Atlanta ,GA,30332			8. PERFORMING ORGANIZATION REPORT NUMBER ; AFRL-OSR-VA-TR-2011-0405	
9. SPONSORING/MONITORING AGENCY NAME(S) AND ADDRESS(ES)			10. SPONSOR/MONITOR'S ACRONYM(S)	
			11. SPONSOR/MONITOR'S REPORT NUMBER(S) AFRL-OSR-VA-TR-2011-0405	
12. DISTRIBUTION/AVAILABILITY STATEMENT Approved for public release; distribution unlimited				
13. SUPPLEMENTARY NOTES				
14. ABSTRACT				
15. SUBJECT TERMS				
16. SECURITY CLASSIFICATION OF:			17. LIMITATION OF ABSTRACT Same as Report (SAR)	18. NUMBER OF PAGES 74
a. REPORT unclassified	b. ABSTRACT unclassified	c. THIS PAGE unclassified	19a. NAME OF RESPONSIBLE PERSON	

DYNAMIC FLIGHT MANEUVERING USING VIRTUAL CONTROL SURFACES GENERATED BY TRAPPED VORTICITY

AFOSR Grant FA9550-05-1-0411

Final Technical Report

Ari Glezer^a, Mark G. Allen^a, Anthony J. Calise^a, Anthony Leonard^b, James M. McMichael^a,
Robert D. Moser^c, and Arne J. Pearlstein^d

^aGeorgia Institute of Technology, ^bCalifornia Institute of Technology,
^cUniversity of Texas at Austin, ^dUniversity of Illinois at Urbana-Champaign

Program Summary

This MURI program addressed integrated closed-loop control of flow and dynamic maneuvering for small UAVs without moving control surfaces. Forces and moments were varied using synthetic jet actuators to effect vorticity generation/accumulation near lifting surfaces, with sensing provided by surface-mounted pressure and flow-direction sensors, and a reduced-order model (ROM) of vorticity dynamics coupled to and integrated with a vehicle dynamics model in an adaptive control architecture.

Both linear and novel output feedback adaptive controller designs, based on an analytical vortex model for predicting the forces and moments produced by flow actuators, were developed and evaluated in a series of wind tunnel experiments. It was shown that advanced adaptive control approaches, based on reduced-order vortex modeling of the fluid dynamics, is essential to realizing the full potential of high-bandwidth flight control afforded by flow actuation. Trimmed free-flight experiments of a nominally 2-D airfoil model representative of a variable-mass and variable-stability aircraft were achieved in the wind tunnel through the design of a traverse support mechanism that permits controlled forces and moments to be externally applied in both pitch and plunge. The formation, evolution, and regulation of controlled trapped vorticity concentrations engendered by hybrid flow control actuators to effect bi-directional changes in the pitching moment and lift for 2-DOF maneuvering of the airfoil model were investigated in detail. It was shown that the vehicle dynamics and the fluid dynamics (under actuation) are closely coupled and simultaneously affect each other. As a result, the aerodynamic forces effected by flow control actuation during a prescribed maneuver are significantly different than the corresponding forces during a similar maneuver effected by external (non-aerodynamic) forces. It was demonstrated that flow control actuation effects aerodynamic forces and moments on time scales commensurate with the convective time scale, indicating that such actuation can be exploited for maneuvering so rapid as to be limited only by the platform's inertia, in contrast to actuation by conventional control surfaces, which is limited by the much slower dynamics of the actuation.

A vortex-based low-order model for the arbitrary motion of a thin airfoil with trailing-edge fluidic control or virtual control surfaces was derived from basic fluid mechanics principles of vortex dynamics with substantial guidance from the results of laboratory and computational experiments. The dynamics of all relevant vortex structures in the near wake and in the boundary layer of the airfoil, including the trapped control vorticity, are approximated by the model. Implementation of the model is reduced to solution of a single ordinary differential equation with a special treatment of a vortex shedding criterion. The model was compared with experimental and high-order numerical simulations, and the results give a reasonably accurate, robust means

of predicting the lift and moment on a thin airfoil including control due to synthetic jet actuation near the trailing edge. The model was implemented successfully in the adaptive control scheme. Vorticity-based ROMs were developed by performing a proper orthogonal decomposition (POD) on the spanwise vorticity obtained from particle-image velocimetry measurements of the streamwise and cross-stream velocity components in the Georgia Tech wind tunnel. Since spanwise velocities introduced by nonuniformity of the synthetic jet actuation introduced significant "errors" when the 2-D continuity equation was used, an alternate approach was developed in which POD was used in the frequency domain to develop a reduced-order model of flow over the actuated airfoil. The ROM based on this approach was used to predict the flow past an actuated airfoil, and the results compared favorably with wind tunnel and CFD velocity and vorticity data. Finally, an approach was developed in which surface measurements of the pressure field were used to construct a ROM consisting of a set of quadratically-nonlinear ODEs.

Computational models accounting for the flow past airfoils modified with trailing-edge synthetic jet actuators, airfoil pitch-and-plunge dynamics, and the adaptive controller were developed and validated, using data from the wind tunnel experiments. Simulations were performed to provide data for reduced-order modeling, to characterize actuation in flows for control or maneuver, to assess controller efficacy, and to perform computational "experiments" under conditions not accessible in the laboratory. It was found that different actuator configurations worked in fundamentally different ways, that actuator performance was sensitive to small variations in geometry, and that for light free-flight airfoils, the integrated controlled system was sensitive to fluctuations caused by vortex shedding.

Large-area, flexible arrays of polymeric flow sensors using integrated multiplexing interconnect for individual sensor addressing were developed along with processes for their mass-manufacturing. These cilia-based sensors are used for the detection of flow direction and magnitude on aerodynamic surfaces. Near-surface velocity distributions were successfully mapped on an airfoil surface in wind tunnel testing, along with the implementation of a drift-resistant algorithm for array readout.

Finally, aerodynamic flow control actuation using a variety of adaptive controller designs that have emerged from the wind tunnel experiments were evaluated in radio-controlled flight tests of a modified Dragon Eye UAV. These tests illustrated the possibility of controlled flight using open-loop flow control actuators. Future research will focus on performing both wind tunnel and UAV flight tests of existing and more advanced adaptive flow controller designs.

Table of Contents

Program Summary	i
I. Overview	1
II. Closed-Loop, Adaptive Flight and Flow Control.....	2
III. Experimental Flow Physics.....	13
IV. Reduced order Models.....	26
IV.1 Discrete-Vortex Based Reduced-Order Model.....	26
IV.2 POD-Based Reduced-Order Models	35
V. Computational Fluid Dynamics.....	43
VI. Large-Area, Polymeric flow Sensors	52
VII. Flight Tests	57
VIII. References	64
IX. Ancillary Information.....	66
Personnel Supported	
Publications	
AFRL Points of Contact	
Transitions	
Honors and Awards Received	

I. Overview

The AVOCET MURI Program provides the foundations for development of flight control for highly maneuverable small UAVs, using a vorticity-centric approach to unsteady aerodynamics and low-order models, together with an adaptive control approach. By definition, the rapid maneuver and gust rejection capabilities sought for small UAVs mean that ***the maneuver time scales associated with vehicle dynamics are of the same order as the flow time scales***. This condition becomes the norm for small UAVs designed for maneuvering in close quarters in urban environments.

Because the flow is driven by both flow actuation and vehicle motion, and the vehicle dynamics is, in turn, driven by the forces and moments generated by the flow, the problem of supermaneuver is one of highly coupled vehicle and flow dynamics. Hence, the desired performance inherently requires an approach that ***simultaneously controls the flow and the vehicle***. Measurements of the flow states and the vehicle states must feed back to the controller, and the system to be controlled is the ***closely coupled dynamical system of flow and the vehicle***. Under these conditions, when the vehicle dynamics and the fluid dynamics (under actuation) are closely coupled and simultaneously affect each other, measurements of both should be provided to an integrated system controller that must be designed using an ***integrated low-order model for the coupled system of actuated flow plus vehicle dynamics***. In addition, adaptive feedback must be used to compensate for intrinsic unmodeled dynamics as well as parametric uncertainty. To compensate for unmodeled ***interactions*** between the flow and vehicle dynamics, the error signal used for adaptation is derived from differences between the ***actual coupled system*** and a ***low-order model of the coupled system***.

Figure I-1 illustrates the integrated control design approach that served as the basis of the work. In this approach, it is assumed that the actuator characteristics are intimately coupled with the flow state, and cannot be viewed as simply in series with the controlled process. This approach requires a fully integrated vehicle/flow control design. A reduced-order reference model approximately representing the vehicle dynamics interacting with the actuated flow is required, in order to model the influence of the nominal controller on regulated output variables. In this architecture, $y(t)$ consists of a subset of the sensed aircraft states *and* the sensed flow variables. A reduced-order model is used to design the nominal controller, so that the nominal controller together with the reference model defines the desired closed-loop performance.

Following the Overview in §I, the present report includes six additional sections that describe the main elements of the MURI Project. Section II describes closed-loop, adaptive flight control architecture developed specifically to exploit the coupling of flow control with vehicle dynamics. Section III discusses experimental investigations of closed-loop aerodynamic flow control for maneuvering a 2-DOF wind tunnel model. Section IV describes the development of reduced order models based on discrete vortices (IV.1) and proper orthogonal decomposition (IV.2). Section V focuses on CFD of the implemented flow control and ROMs. Section VI describes the development of novel, surface-mounted flow sensors. Finally, §VII describes flight tests of flow control technologies on a small-scale UAV.

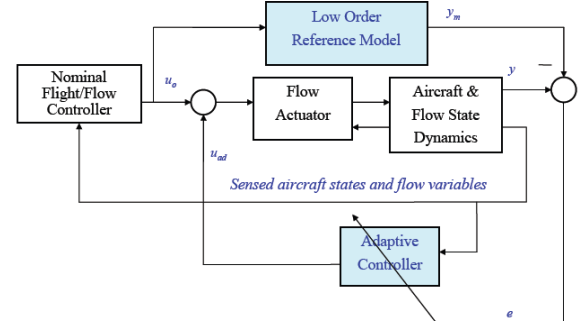


Figure I-1 Integrated adaptive control architecture

II. Closed-Loop, Adaptive Flight and Flow Control

The goal of closed-loop control is to realize the highest attainable bandwidth in feedback control design that is afforded by the use of synthetic jet actuators, through feedback of both conventional position and inertial sensors, and surface-mounted pressure and flow-direction sensors. Since control design bandwidth is limited primarily by the accuracy of the models employed to represent the actuators, adaptive control design is viewed as an enabling technology for overcoming the limitations inherent in conventional linear control design with respect to trading performance for robustness to modeling errors. While adaptive methods represent the most advanced approach for dealing with modeling error, they should be married with the best methods for developing models of the actuated flow dynamics in a form suitable for control design purposes. This marriage has been the primary collaborative field of endeavor for this effort.

Initially a linear controller was designed for a rigid-body approximation to the physical test model by modeling the actuators as linear static devices. With that approach, successful closed-loop control of pitch motion of a 2-DOF wind tunnel model using flow control actuators was achieved (Muse 2008). This controller worked well for slower maneuvers where the static actuator assumption holds. For faster maneuvers, requiring higher bandwidth controller design, interactions between the flow and vehicle dynamics become more important and the linear rigid-body model can no longer be used for control design purposes. In these regimes, linear controllers that ignore the dynamic effects of flow actuation have limited and possibly destabilizing performance. A neural network (NN) based adaptive controller was introduced to improve the controller performance by compensating for the modeling errors in the design including the unmodeled dynamics of actuation (Muse 2008). In comparison to our initial effort, quantifiable differences between flow actuation and torque motor actuation can now readily be observed. An LQR controller was designed to regulate plunge position by pitching the airfoil, with the assumption that a static linear actuator can generate a pure pitching moment in response to controller commands (Muse 2008). The system obtained by closing the loop around the linear model with the designed controller forms the reference model for the adaptive controller design. This model constitutes the ideal closed-loop response of the system. Figure II-1 shows high-bandwidth experimental results for a sample step command tracking maneuver. The reference model trajectories are shown with red dotted lines. The response of the airfoil when the loop is closed through the torque motor (blue line) agrees with the reference model extremely well both in pitch and plunge. When the loop is closed with the flow actuators (red line), the response of the system is significantly less stable than the reference model, even though the difference in the static gain of the actuator has been taken into account in the controller design. This can be attributed to the dynamic and nonlinear

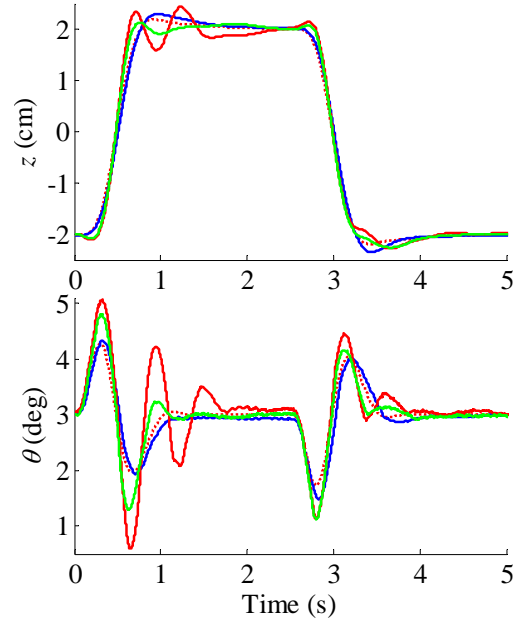


Figure II-1 Step command tracking in plunge:
 ideal reference model response,
 — linear controller response with torque motor
 actuation, — linear controller response with
 flow actuators, — adaptive controller response with
 flow actuators.

that a static linear actuator can generate a pure pitching moment in response to controller commands (Muse 2008). The system obtained by closing the loop around the linear model with the designed controller forms the reference model for the adaptive controller design. This model constitutes the ideal closed-loop response of the system. Figure II-1 shows high-bandwidth experimental results for a sample step command tracking maneuver. The reference model trajectories are shown with red dotted lines. The response of the airfoil when the loop is closed through the torque motor (blue line) agrees with the reference model extremely well both in pitch and plunge. When the loop is closed with the flow actuators (red line), the response of the system is significantly less stable than the reference model, even though the difference in the static gain of the actuator has been taken into account in the controller design. This can be attributed to the dynamic and nonlinear

characteristics of the flow actuators, which are coupled with the fluid dynamics, and which become more evident when a high-bandwidth control design is used. These oscillations increase in amplitude and duration when higher-bandwidth designs are implemented, and eventually cause instability. Therefore, one of the major goals of adaptive control in this application is to accommodate actuator modeling error, and permit higher-bandwidth controller design. The same controller design augmented with a NN based adaptive control (green line) yields a much more stable response, which is closer to that of the reference model. For a given bandwidth, the adaptive controller also provides improved response to larger amplitude maneuvers.

II.1 Evaluation of Vortex Model Based Controller Designs

As part of the MURI effort, a low-order vortex model for a pitching and plunging airfoil with trailing edge synthetic jets was developed at Caltech (Tchieu 2009). Unlike many other low-order or reduced order models, this model was built from physical principles, i.e., conservation of momentum. The next step was to make use of the this vortex model to improve the linear control-law design, and to design augmenting adaptive controllers for 2DOF maneuvers which could theoretically provide better performance than the designs obtained used a static actuator model. Therefore, it was necessary to linearize the vortex model. The vortex model also captures dynamics that are negligible on the time scales of a flight control system. Therefore, we further reduced the order of the vortex model for control design purposes. The next step was to experimentally validate both the original vortex model and the simplified linear vortex model used for control design.

In order to evaluate the static actuator model, the nonlinear vortex model, and the linear vortex model, simulations using a single-degree-of-freedom model were performed and these results were compared with experimental results. The experimental results were obtained with the ball screws locked in position so that the wing model was only allowed to pitch. The airfoil was then trimmed at an angle of attack of 3 degrees, and the torque motor was used to stabilize the pitch response of the wing. Then a series of doublets with an amplitude of ± 10 volts and of increasing duration were applied to the flow actuator, as shown in Figure II-2a. In this setting, the flow actuators are being used to introduce a disturbance torque. The corresponding pitch response of the experiment was then compared to the simulated responses. As seen in Figure II-2b, the simulated response obtained using a static flow actuator model deviates significantly from the experimental pitch response. This is consistent with our previous observation that the static actuator model does not adequately capture the response of the flow actuator. Figure II-2b also shows that the simulated responses obtained using the linear vortex actuator model and the nonlinear vortex actuator model responses are

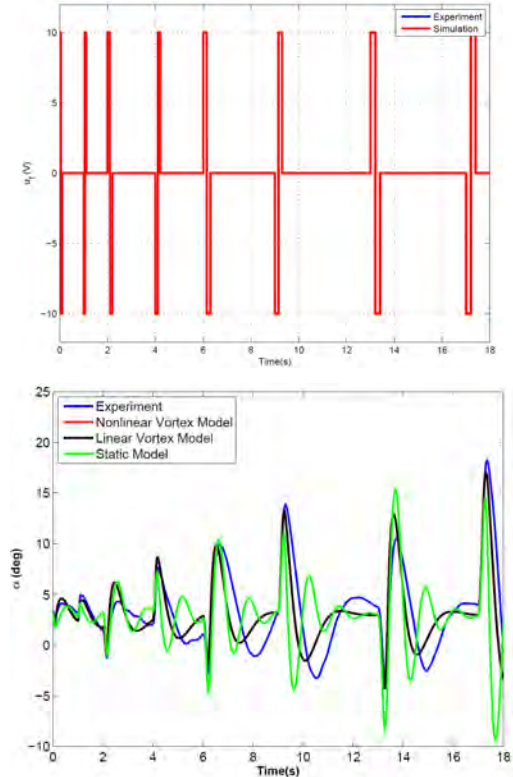


Figure II-2 (a) (top) Pulse input applied to flow actuator, and (b) (bottom) Pitch angle comparison of models with experiment.

nearly identical, and both more accurately predict the experimental response in comparison to the simulated response obtained using the static actuator model. This justifies use of the linear reduced vortex model for control design purposes.

The linear vortex model was used to redesign the LQR controller, which in turn was augmented with a NN-based adaptive controller. Due to linearization, the control variable for the linear vortex model is a non-physical term that is related to the flow control voltage is the system states. One other issue was that all the states in the model is not available for feedback. The nominal control design consisted of a robust servomechanism LQR projective control law with an augmented feed forward term to improve transient error tracking response (Muse 2009). The feedback gains were *projected* to obtain a solution in output feedback form. The control architecture for the robust servomechanism controller is given in Figure II-3. The linear vortex model ignores nonlinearities and unmodeled dynamics associated with the actual flow actuation process. In order to compensate for this, the baseline linear controller mentioned above was augmented with an adaptive controller. A nonlinear, whose weights are adapted online, was used to approximate the ignored nonlinearities. To construct such an approximation in an output feedback setting, it is necessary to use delayed values of sensed and known variables as inputs to the NN.

To test the effectiveness of the linear controllers designed using the static actuator model, the linear vortex model, and the adaptive versions of these designs, a series of experiments was conducted in the wind tunnel. To evaluate improvements in performance, we slowly reduced the

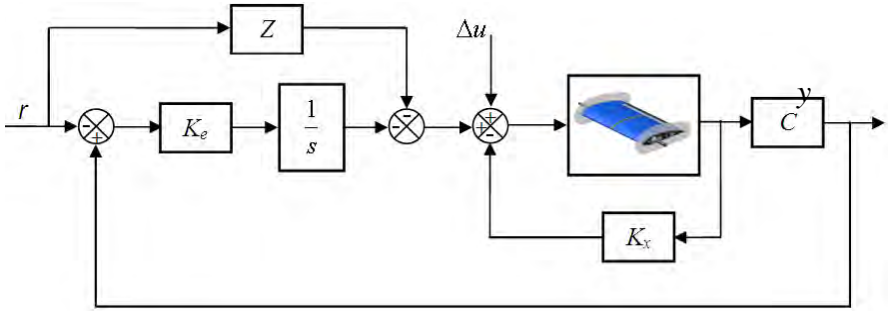


Figure II-3 Robust servomechanism LQR with feed forward element and adaptive control signal

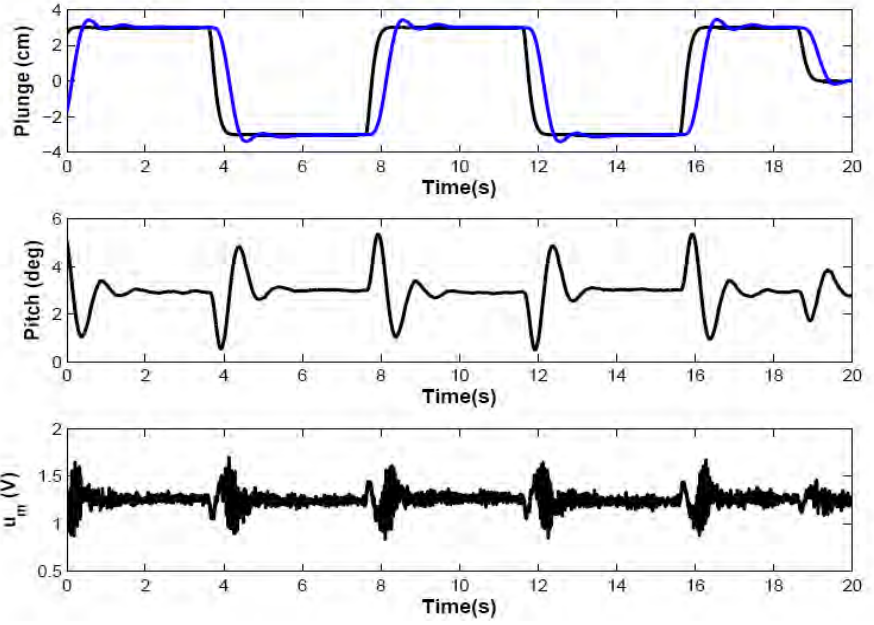


Figure II-4 Comparison of linear control responses based on a static actuator model: (—) response with torque motor actuation, (—) response with flow actuators.

response rise time of each design until the controller failed to stabilize the airfoil. Each controller was tuned based solely on a simulated linear design model. The controllers were not tuned in the experiment. Figure II-4 compares two experimental responses obtained using a linear controller design based on a static model for the actuator. The black line is the response with torque motor actuation and the blue line is the response obtained using the flow actuators. The torque motor output was scaled to have the same control effectiveness as the measured gain of the flow actuators. Therefore the same controller gains were used in each experiment. The lag due to flow actuation is evident in these responses. The response with flow actuation is very close to

actuation and the blue line is the response obtained using the flow actuators. The torque motor output was scaled to have the same control effectiveness as the measured gain of the flow actuators. Therefore the same controller gains were used in each experiment. The lag due to flow actuation is evident in these responses. The response with flow actuation is very close to the reference model response (not shown). Hence, the traverse is functioning as expected for this controller design bandwidth. Figure II-5 compares the response of the vortex model based linear control design to a control design obtained using the static model, for a design bandwidth corresponding to achieving a rise time of 0.63 seconds (rise time is defined as 10 percent to 90 percent of the final command).

The controller design based on a static actuator

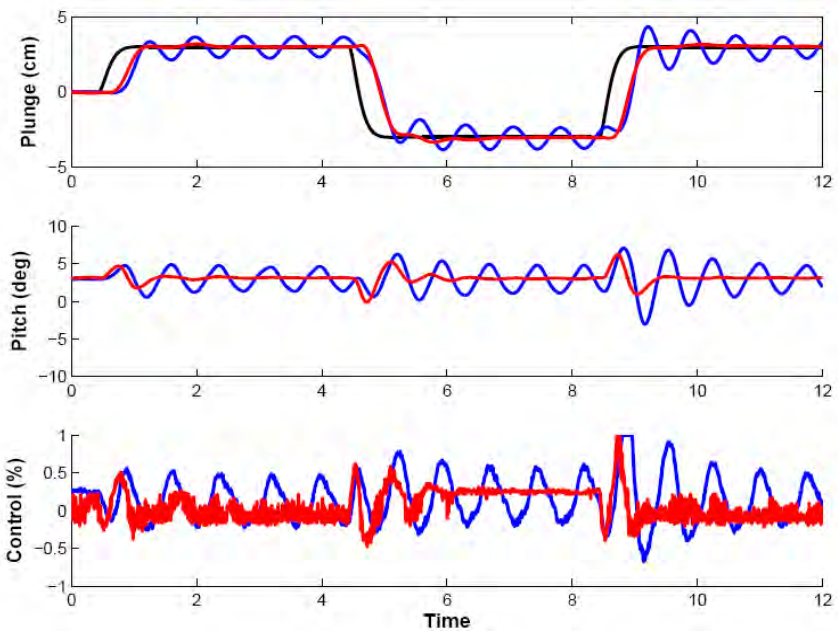


Figure II-5 Comparison of linear controller responses: (—) design based on a static actuator model, (—) design based on the linear vortex model.

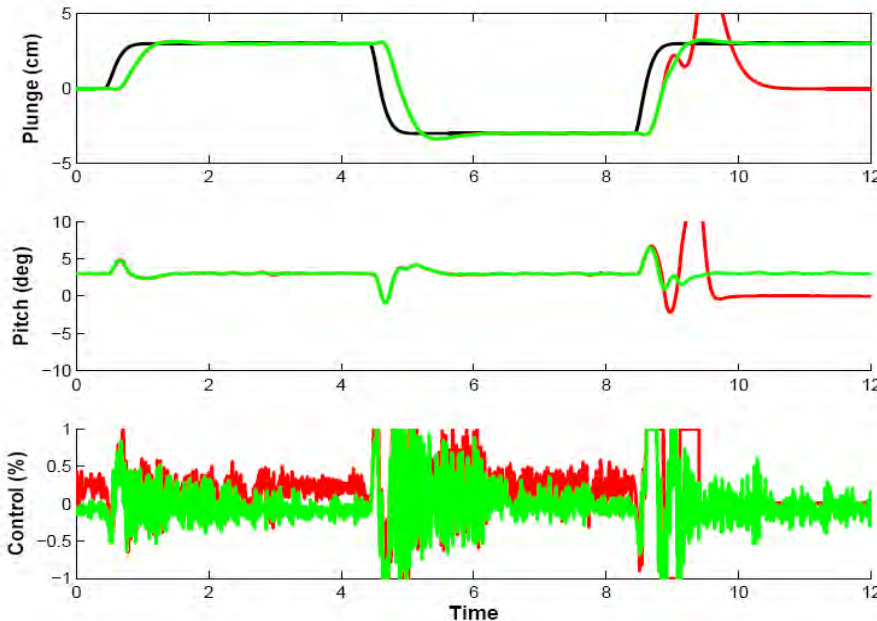


Figure II-6 Comparison of controller responses: (—)linear controller based on the linear vortex model, (—) linear controller augmented with NN adaptive controller.

model in this case exhibits a limit cycle behavior that does not decay. However, the response employing the controller designed on the basis of the linear vortex model remains close to the reference model response. In Figure II-6, the bandwidth of the vortex model based linear control law design is further increased. The effective rise time for this design is 0.43 sec. The vortex model response (shown in red) is stable for a while, but

suddenly goes unstable. However, when this same design is augmented with the NN adaptive control law, it remains stable. Figure II-7 gives a visual comparison of the experimentally achievable rise time performance for each controller design. The linear controller design based on a static actuator model achieved a rise time of 0.60 seconds. When this design is augmented with an adaptive controller, the achievable rise time was further reduced to 0.49 seconds. The linear controller design based on a linear vortex model achieved a rise time of 0.43 seconds. When this design was augmented with an adaptive controller, the rise time was further reduced to 0.41 seconds. We were not able to explore further reductions in rise time due to the limitations of the present force controller design for the traverse, described in Section II.3.

II.2 Norm Minimization Adaptive Control

A new adaptive control methodology that merges ideas from linear robust control theory and nonlinear control theory, called H_∞ -Norm Minimization (H_∞ -NMA) was developed and applied to closed-loop flow control (Muse 2010 a,b). It enables bandwidth limiting of the adaptive control signal using linear control design methods, and is able to handle both unmatched and matched uncertainty in a single design framework. In addition, it provides notions of transient performance bounds. This new architecture was implemented and evaluated for 2DOF maneuvers in the wind tunnel. It was used to adaptively augment the same baseline LQR linear controller described in the previous section. A series of experiments was then carried out and the resulting performance was compared with that of the more conventional adaptive controller described previously.

Two test cases were evaluated in the wind tunnel for closed-loop flow control. The first evaluated effectiveness of H_∞ -NMA adaptive control in rejecting an externally applied disturbance of increasing magnitude, in comparison to a linear controller design that makes use

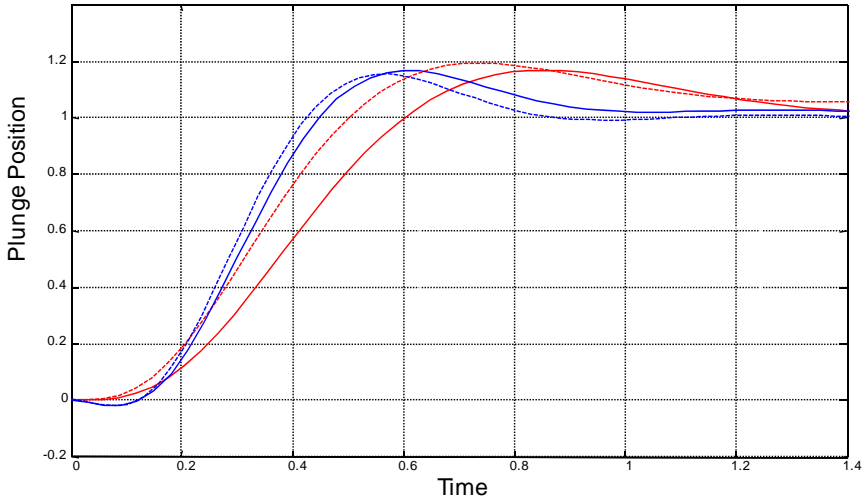


Figure II-7 Rise time stability barriers: (—) linear controller based on static actuator model, (---) adaptive controller based on static actuator model, (—) linear controller based on vortex model, (---) adaptive controller based on vortex model.

of the vortex model, and to that of the same controller with conventional adaptive control augmentation. Theoretically, since the disturbance is bounded and not state-dependent, each control law should have a bounded output response. However, due to control authority limits, the system will eventually destabilize. One advantage of H_∞ -NMA is its ability to avoid the level of control authority needed to achieve a given level of adaptation. Instability occurs when the pitch angle of the wing deviates too far and too fast for the system to recover.

Figure II-9 shows that the limit of performance was not improved when the same linear controller is augmented with the standard output feedback adaptive control law. Figure II-10 shows that a significant improvement in the limit of performance was obtained when the linear controller is augmented using the H_∞ -NMA output feedback adaptive control law. This figure shows that the system remains stable for a disturbance sweep from 1.0 kg to 4.0 kg in 1.0 kg increments. Long-term

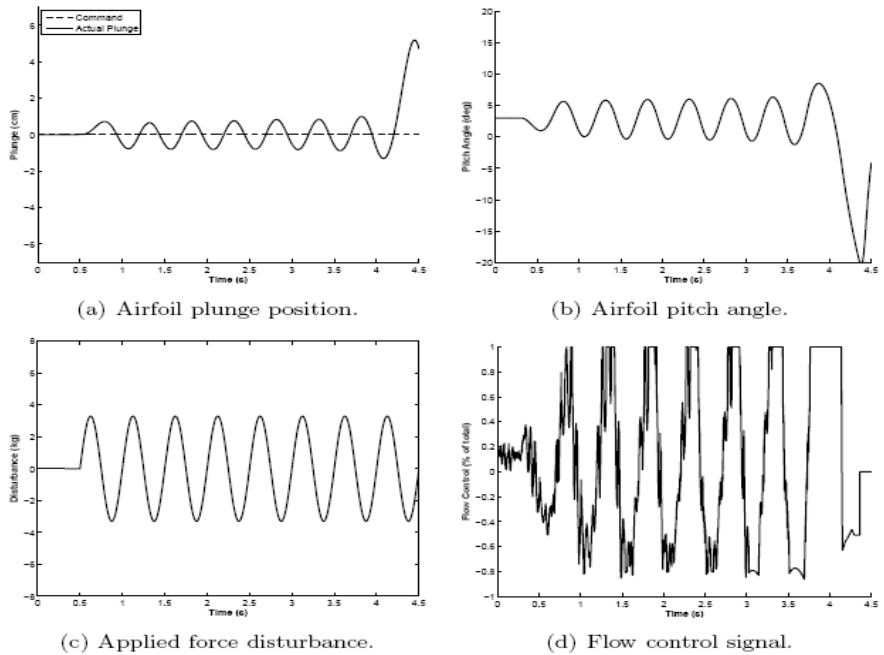


Figure II-8 Vortex model based linear control law response for 2Hz sine wave disturbance at 3.3kg Amplitude.

Figure II-8 examines the ability of the linear vortex model based control law to reject a sine wave disturbance. The system goes unstable when the disturbance amplitude is increased to 3.3 kg. Note the growth in saturation in the flow control signal shown in part (d) of this figure.

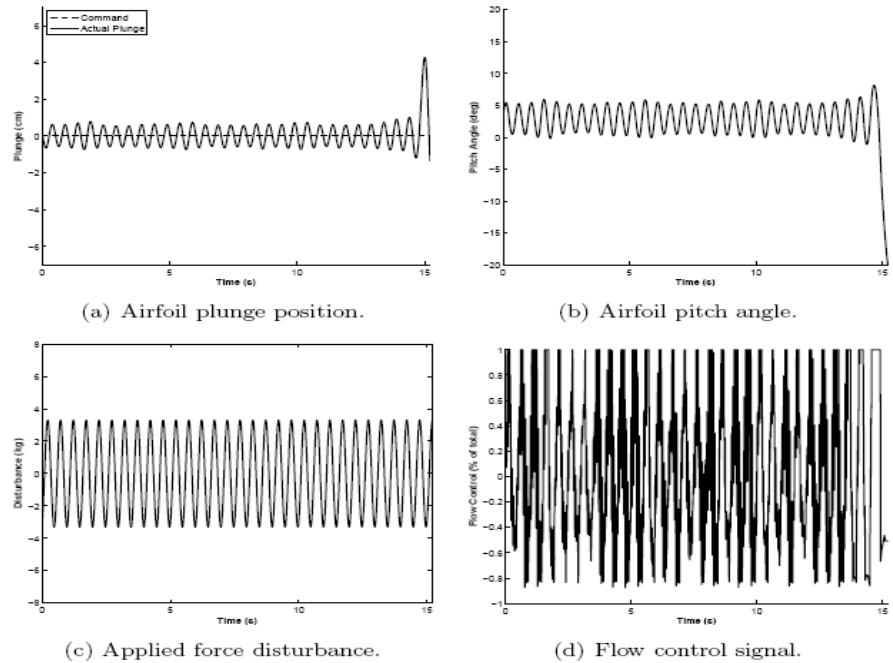


Figure II-9 Output Feedback Adaptive control law response for 2Hz sine wave disturbance at 3.3kg Amplitude

tests were repeated at the 4.0 kg level to confirm that the system remained stable.

Next, the plunge command tracking performance of both output feedback adaptive control laws was explored under an applied disturbance. The plunge command to the system was a 0.5 Hz, 10 cm peak-to-peak sine wave. The disturbance applied to the system was a 2.0 Hz sine wave whose amplitude was varied. In each test, the system was trimmed at 0.0 cm at a pitch angle of 3.0°. The disturbance was first applied for a few seconds and then the plunge command was engaged. Figure II-11 shows that the linear vortex model based controller is stable for a disturbance amplitude below 2.7 kg, but goes unstable when the plunge command was injected. Figure II-12 shows that a similar result was obtained when the same linear controller was augmented with the standard output feedback adaptive control law. Figure II-13 shows that a significant improvement in tracking performance for the same disturbance level was obtained when the linear controller was augmented using the H_∞ -NMA output feedback adaptive control law.

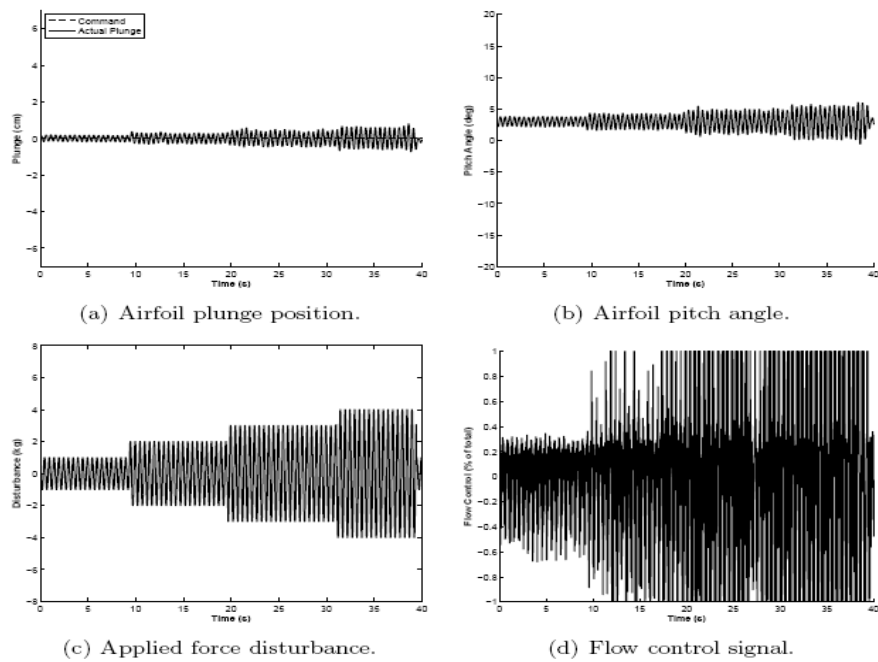


Figure II-10 H_∞ -NMA control law response for 2Hz sine wave disturbance sweep from 1 to 4.0 kg Amplitude

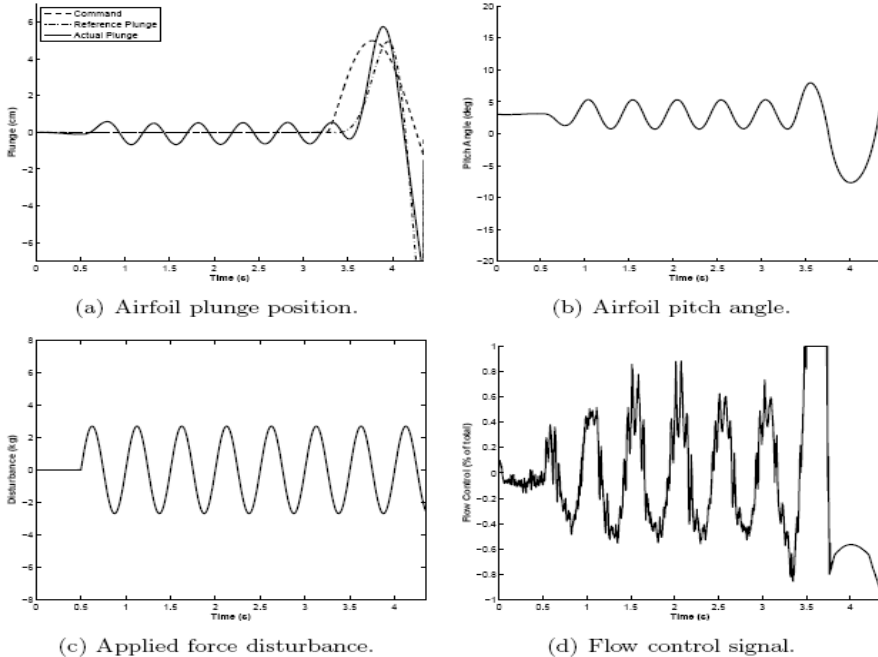


Figure II-11 Vortex based linear control law failure with a 0.5 Hz sine wave command with a 2.7 kg applied disturbance.

similar result was obtained when the same linear controller was augmented with the standard output feedback adaptive control law. Figure II-13 shows that a significant improvement in tracking performance for the same disturbance level was obtained when the linear controller was augmented using the H_∞ -NMA output feedback adaptive control law.

II.3 Emulating Free Flight in the Wind Tunnel

One of the limiting factors in evaluating the performance of active flow control in the wind tunnel is the inability to emulate free flight using the traverse mechanism and a force controller (Muse 2008 b). Over the years, we have improved the design of the force controller to emulate free flight at increasing bandwidths. In order to be able to represent the complete longitudinal

dynamics of an arbitrary aircraft configuration, we control the forces and moments that are applied to a wing model suspended in the tunnel through a traverse mechanism. The techniques used in this application are different than those used in robotics because controlled force and moments must be applied on a system while in motion, and the control system must restrict the model to stay in the longitudinal plane

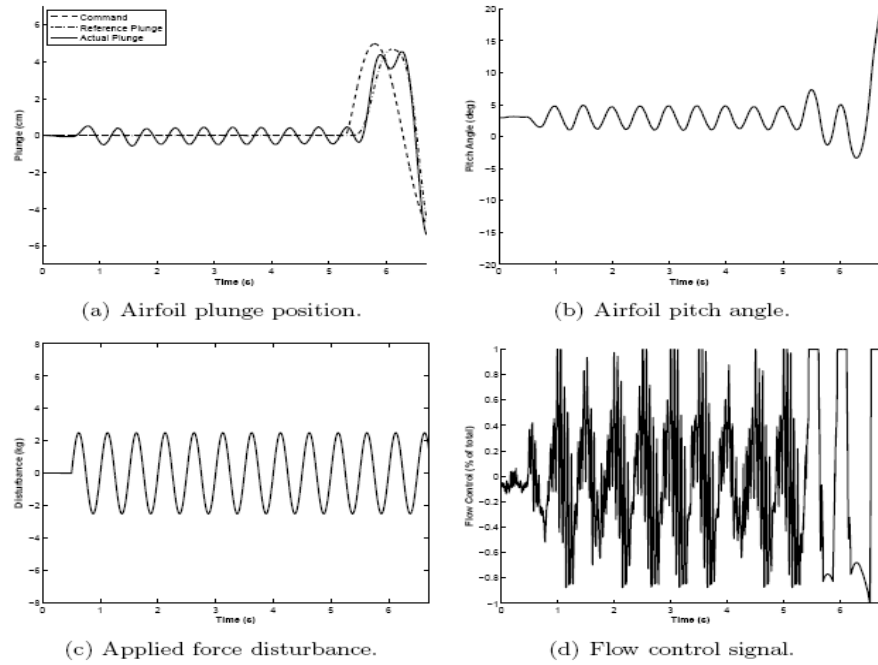


Figure II-12 standard adaptive control law failure with a 0.5 Hz sine wave command with a 2.5 kg applied disturbance

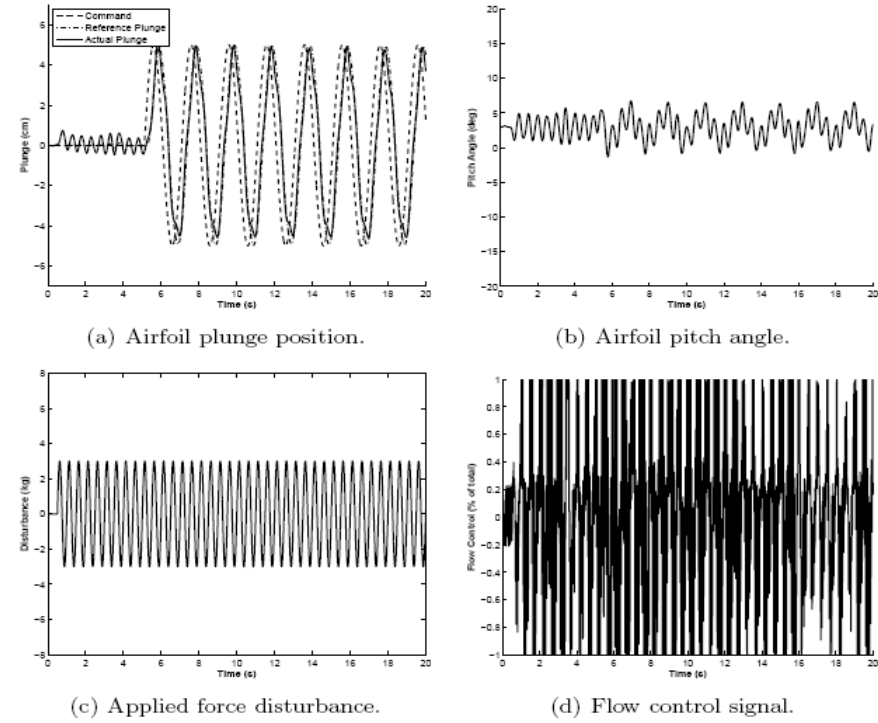


Figure II-13 H_{∞} -NMA Output Feedback Architecture tracking a 0.5 Hz sine wave command with a 3.0 kg applied disturbance.

regardless of the commands and applied disturbance forces on the plunge axis. The control objective was achieved by manipulating the forces applied by two servo-driven ball screws and the moment applied by a servo motor in the pitch axis. Applying a prescribed force to the model was difficult due to the large mass and high friction of the linear drives in relation to the model. The limitations in force control arose from the lack of compliance between the model and the linear actuator. Having a stiff coupling between the actuator and the point of force application can cause a chattering effect. This is due to a large stiffness at the force measurement point. Furthermore, a stiff coupling results in poor force tracking. This is due to the actuators not being able to respond quickly enough to maintain an acceptable level in force tracking error. To overcome these limitations, linearly compliant springs were mounted between the model and each ball screw carriage. The contact force between the actuator and the model can then be precisely regulated through control of the spring deflections.

To study aircraft flight in a wind tunnel on a traverse heavy enough to carry all of the support and measurement equipment, the control system must serve three fundamental purposes: removing the effect of the high traverse mass, modifying the stability characteristics of the model, and restricting the motion of the traverse to the longitudinal plane. To meet these requirements, a three-loop control architecture was used, consisting of the carriage control loop, the force control loop, and the stability modification loop. The carriage control loop is the innermost loop. Since modeling the friction effect in ball screws is difficult, high-gain, manually-tuned PID control laws were used to control the carriage positions. The response of each side of the traverse was tuned to have a unit gain response over a wide range of frequencies. This approach has several benefits. First, manually tuning a ball screw for position tracking is a relatively straightforward task. It also serves the effect of *hiding* the large friction-type nonlinearities of the traverse, allowing precise modeling of the rest of the traverse dynamics. From a control design standpoint, this allows removal of the carriage state from the equations of motion, which simplifies the control design. Finally, the motion of the model on the springs has a negligible effect on the carriage positions. This allows one to assume that the spring-traverse system can be modeled as a cascaded linear dynamical system. Using a cascaded model of the traverse dynamics, the carriages are commanded to maintain a wings-level bank angle, and a force control law was designed to regulate the total applied force from both spring sets. It should be noted that the open-loop spring-carriage dynamics were modified with integrators in cascade to the carriage command. This was done to shape the open-loop frequency response to achieve good force command tracking. From a practical perspective, this serves to convert a force command to a position command (position is the second integral of a function of the applied force). It also allows a straightforward method for limiting the position and velocity of the ball screws via saturation limits on each integrator. This prevents the system response from violating carriage position and ball screw rate limits. The force control law consists of two control loops. The carriage control loops consist of two independent, high-bandwidth, manually-tuned PID control laws (referred to as the carriage control loop) that are used to regulate the linear slide positions. The force control loop was designed using a standard LQR control law. This loop receives force commands in the plunge axis and generates carriage acceleration commands to the inner loop to achieve the desired applied forces. Applied moments are generated directly from a servo motor in torque mode.

The first generation force controllers were based on rigid-body dynamics which ignored the effects of wing bar bending. As the project progressed, it was necessary to simulate free flight in the wind tunnel at higher and higher bandwidths. Since the original force controller was

designed ignoring bar bending, it did not provide accurate force tracking at higher frequencies. The first generation force controller was limited to simulating free flight up to a bandwidth of around 3 Hz, due to the presence of the bar bending mode. In order to overcome this limitation, the physical model was re-designed to move the bar bending mode to around 15 Hz. Once the redesigned model was tested in the wind tunnel, the bandwidth of the force controller was increased to around 10 Hz as shown in Figure II-14. The force controller was designed using a rigid-body model of the traverse mechanism, which restricted the usable frequency range of operation of the model to this frequency. In order to simulate free flight at frequencies greater than 10Hz, where the unsteady aerodynamic effects dominate, an improved model of the traverse was needed. Modeling of the traverse bending dynamics based on Lagrangian dynamics did not yield a model that adequately represented the actual physical model, due to the complexity of the traverse. This necessitated development of a low-order model consisting of multiple lumped masses, and fitting the parameters of that model to experimental data (Chandramohan 2010).

In order to obtain data from the traverse for modeling purposes, specialized hardware was used to generate the excitation signals that were used to excite the traverse and obtain the frequency response function. Digital signal processing (DSP) based hardware (SigLab) along with a Matlab-based toolbox was used to excite the system. Initially, the signal generated from the SigLab hardware was directly fed to the servo motors connected to the ball screws, to excite the system. This did not produce good results due to the inherent friction and backlash associated with the ball screws. To overcome this, a random signal with frequencies between 0 and 50 Hz and a resolution of 0.03 Hz was generated using the SigLab hardware and fed into the system as a commanded position for the carriage controllers. An accelerometer was used to measure the resultant acceleration experienced by the system along six different locations on the bar on which the airfoil was mounted. A frequency-response function was obtained using the software provided with Siglab. Two such sets of data were obtained from the experimental setup. In the first set, only the front-side carriage was excited using the signal generated from SigLab, while the back-side carriage was held fixed at the reference position by setting to zero the position command input to it. The next set of frequency-response functions was obtained by exciting the back-side carriage using the signal from SigLab and holding the front-side carriage fixed at the reference position by setting the position command input to it to zero. The model obtained using acceleration measurements along the bar provided an accurate representation of the system dynamics, but unfortunately was not useful for building a model that could be used to design the force controller. This necessitated obtaining another set of frequency response functions with another set of available sensors as the output. As before, SigLab was used to generate the carriage position commands used to excite the system, and the outputs this time consisted of the forces measured by the load cells in series with the spring sets, and the strain gauge mounted at the center of the bar. Six different frequency-response functions were obtained from the two inputs (the front and back carriage positions), and the three outputs (front load cell, back load cell and strain gauge). The frequency response functions obtained from the system were then

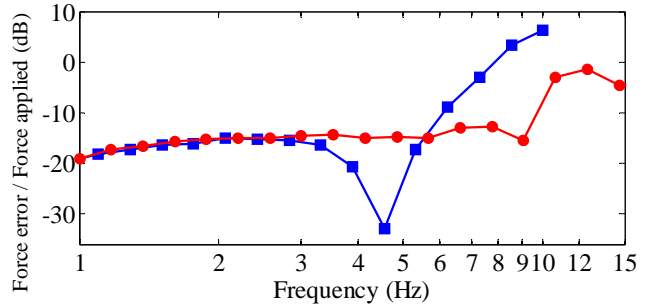


Figure II-14 Force controller performance, —■— old design, —●— new design.

used to obtain a useful model for designing the force controller. Several force controllers were designed using this improved model, which will be used to simulate free flight out to around 15 to 20 Hz bandwidth. These force controller designs are presently being evaluated.

II.4 Summary

Both linear and novel output feedback adaptive controller designs, based on an analytical vortex model for predicting the forces and moments produced by flow actuators, have been developed and evaluated in a series of wind tunnel experiments. It has been shown that advanced adaptive control approaches, based on reduced-order vortex modeling of the fluid dynamics, is essential to realizing the full potential of high-bandwidth flight control afforded by flow actuation. Trimmed free-flight experiments representative of a variable-mass and variable-stability aircraft were achieved in a low-speed wind tunnel through the design of a traverse support mechanism that permits controlled forces and moments to be externally applied in both pitch and plunge. Flexibility in the wing support structure is presently the limiting factor in our ability for explore higher-bandwidth adaptive flow control designs in the tunnel. Future research will focus on improving the traverse force controller design to account for flexibility, and on performing both wind tunnel and UAV flight tests of existing and more advanced adaptive flow controller designs.

III. Experimental Flow Physics

Closed-loop adaptive, flow control for aerodynamic maneuvering of flight platforms in the absence of conventional, moving control surfaces was demonstrated in wind tunnel experiments and later on implemented in flight tests of a small-scale UAV. The present investigations focused on maneuverability and coupled platform and flow dynamics in two degrees of freedom (pitch and plunge) that was effected by exploiting bi-directional control of the pitching moment using trapped vorticity near the trailing edge of a free airfoil model (Muse et al., 2008, and Brzozowski et al. 2008). The research was divided into two overlapping phases that included characterization of the open-loop aerodynamic response to flow control actuation, followed by demonstration of commanded, closed-loop control for trajectory tracking and disturbance rejection.

III.1. Experimental Setup

The Airfoil Model

The experiments were conducted in an open-return low-speed wind tunnel having a square test section measuring one meter on the side. The airfoil model has a constant cross-section based on a NACA 4415 (Figure III) with a chord $c = 457$ mm and maximum thickness to chord ratio of $t/c = 0.15$. The model, which spans the entire width of the wind tunnel test section, is comprised of multiple sections of composite skin wrapped over an aluminum frame. Measurements of distributions of circumferential surface pressure are obtained using a cross sectional segment that can be inserted between adjacent sections. This segment (fabricated using stereolithography) includes integrated, internal conduits for 73 static pressure ports and several additional collocated ports for simultaneous measurements of time-dependent pressure using high-frequency sensors (Figure III-1c). The assembled model is mounted on a hollow shaft (outer diameter $D_o = 1.625'$) and installed in the test section with the ends of the shaft protruding through vertical slots in the side walls.

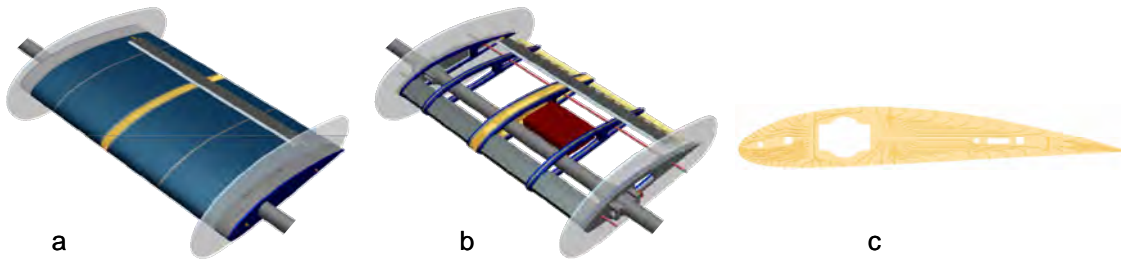


Figure III-1. Wind tunnel model shown (a) fully assembled and (b) with the fiberglass skin removed. (c) An SLA insert is integrated with 73 static pressure ports and 4 high-frequency pressure sensors.

Flow Control Actuators

Bi-directional pitching moments on the model are effected by movable, surface-mounted hybrid synthetic jet actuators (DeSalvo and Glezer, 2007) that are located just upstream of the trailing edge on the pressure side (PS) and suction side (SS) of the airfoil (Figure III-2a). The hybrid actuators have a characteristic height of $0.017c$ above the airfoil surface, and cover its entire span. The synthetic jets are spanwise-segmented and are each driven by a 33 mm diameter composite piezoelectric membrane that is integrated into an individual cavity to form an array of 17 adjacent actuators. The jets issue through a 0.4 mm wide, 33 mm long rectangular orifice where the long side is parallel to the trailing edge of the airfoil, and the spacing between adjacent

orifices is about 2 mm. The piezoelectric membranes of each spanwise (*PS* or *SS*) actuator are driven simultaneously by a bank of external amplifiers at $f_{act} = 2050$ Hz (the actuator assembly has a relatively flat response around the characteristic resonance frequency of the piezoelectric membrane). As discussed in Section II and further below, the controller is designed so that operation of the *SS* and *PS* actuator arrays is mutually exclusive, and the actuators may be modeled as a traditional control surface (at low maneuvering frequencies), where *SS* and *PS* operation correspond to nose-down and up, respectively. In the present investigations, a single dimensionless parameter describes the actuation state:

$$u_f = \frac{\varepsilon_{disk}}{\varepsilon_{max}} \delta_{act} \text{ where } \delta_{act} = \begin{cases} -1 & PS \text{ actuation} \\ 0 & \text{no actuation} \\ +1 & SS \text{ actuation} \end{cases}$$

where ε_{disk} is the RMS voltage applied to the piezoelectric disks and $\varepsilon_{disk} = 100$ V_{RMS} is the maximum rated driving voltage (i.e., $-1 \leq u_f \leq 1$ with $u_f = -1$ and $u_f = 1$ corresponding to full *PS* and full *SS* actuation, respectively). The actuators were calibrated using hot wire anemometry and, as shown in Figure III-2b, the RMS jet exit velocity scales approximately linearly with the driving voltage.

The 2-DOF (Pitch/Plunge) Traverse

In the present experiments, the wind tunnel model executes commanded flight maneuvers in two degrees of freedom (pitch and plunge) that are exclusively effected by flow control actuation within the constraints of the tunnel's test section. The model is mounted on a programmable, 2-DOF traverse that is constructed on an I-beam frame around the test section of the wind tunnel (Figure III-3) and enables pitch and plunge motions (some roll can also be provided). The traverse is driven electromechanically (using an angular pitch drive and two linear motors for plunge motion) by a dedicated ("inner loop") feedback controller that removes the effect of parasitic mass and rotational inertia of the dynamic support system. The inner-loop controller is enforces a prescribed angle of attack $\alpha(t)$ trajectory. It also serves as a virtual variable tail surface by providing the torque required to trim the model at any given condition, and by modifying its dynamic characteristics by changing its

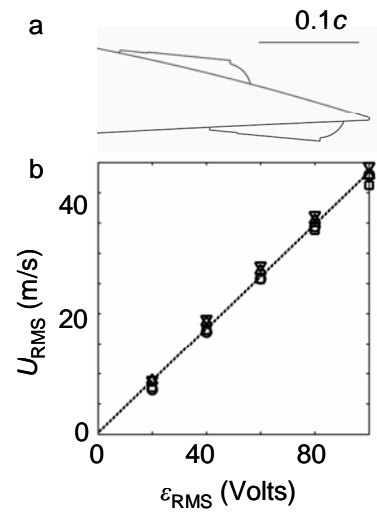


Figure III-2. (a) Actuator placement on either side of the trailing edge, and (b) Actuator calibration curve.

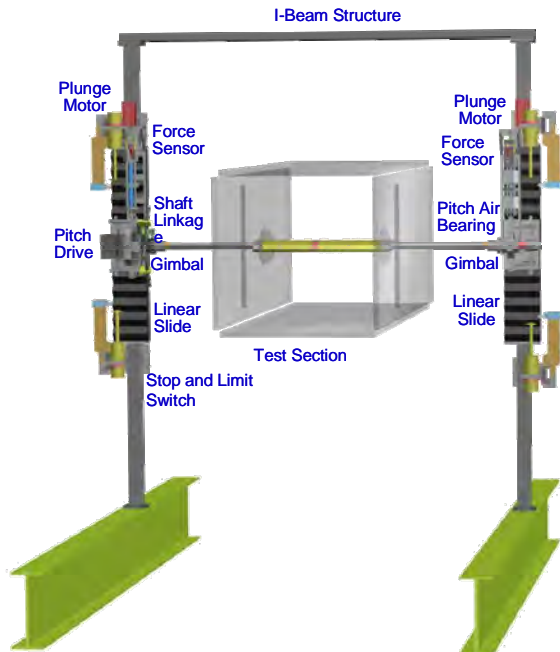


Figure III-3. The 2-DOF (pitch/plunge) traverse.

stiffness and damping properties. The application of torque τ_s , pitch($\alpha, \dot{\alpha}, \ddot{\alpha}$) effectively alters $\partial C_M / \partial \alpha$ and $\partial C_M / \partial \dot{\alpha}$, and the moment of inertia of the model. The controller allows for control of a range of ‘virtual’ air vehicles, all having the same wing as the wind tunnel model, but with static margins that can be adjusted by the traverse controller, including unstable configurations for high maneuverability. The wing model is mounted on a rotating hollow shaft (for wiring and pressure tubes) and is rotated by AC servo motor (that is carried by the vertical stage) on one end, while at the opposite end the pitch shaft is supported by an air bearing that allows both rotational and axial motions. The axial shaft motion allows the wind tunnel model to bank while it is maneuvered in pitch and plunge since the two plunge drives are controlled independently on each side of the tunnel. Both ends of the pitch axis are connected to the linear slides through gimbals that allow free rotation about axes in the streamwise and cross stream directions, and prevent misalignment from binding the plunge slides. Each slide includes a carriage that is moved along rails by a ball screw turned by an AC servo motor with an integrated encoder and an electromagnetic release brake that prevents load on the carriage when the traverse is not in operation. The travel of each linear slide is constrained by adjustable stops and limit switches. In the present work, the linear motion of the model is limited to speed and acceleration of up to 0.5 m/sec and 2g, respectively (the maximum design speed and acceleration in the present configuration are 2.5 m/sec and 5g). Model position, speed, and acceleration are monitored using optical encoders, and the aerodynamic forces (lift and drag) and moment (pitch) are inferred from force transducers between the model and the support system.

III.2 Quasi-Steady Actuation

Modification of the Aerodynamic Forces

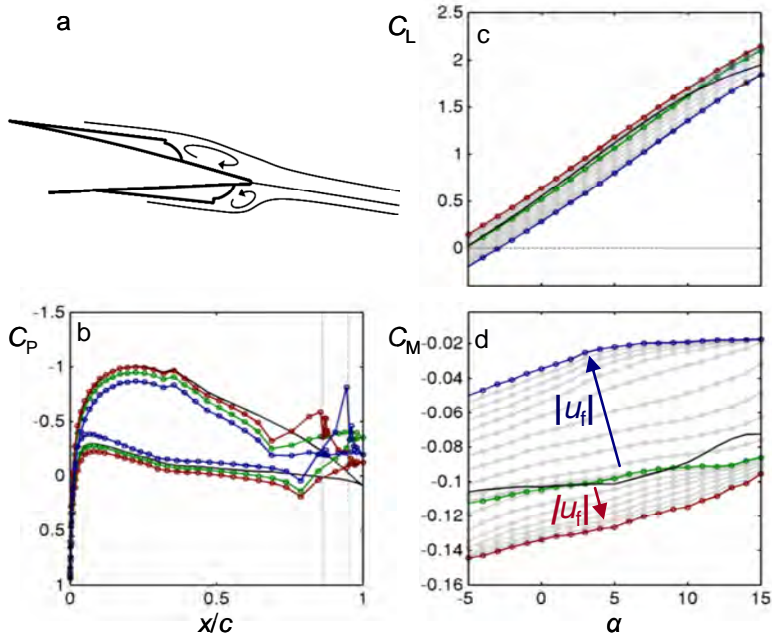


Figure III-4. (a) Schematic of the flow over the trailing edge; (b) Pressure distributions: modified, unactuated (green); full SS actuation (red); and full PS actuation (blue), gray lines show actuator locations; (c) and (d) Variation with α of C_L and C_M for a range of actuation levels.

The effects of continuous actuation were characterized over a range of angles of attack, actuation levels, and streamwise actuator locations. Typical distributions of surface pressure are shown in Figure III-4b for $\alpha = 0^\circ$ for the airfoil with the installed, but inactive actuators, full SS actuation, and full PS actuation (the location of the SS and PS actuators are marked by gray lines). The installation of the actuator modules (Figure III-4a) results in some changes in the pressure distribution of the smooth airfoil

primarily near the trailing edge. On the suction surface, the pressure increases slightly (i.e., decreasing suction) near the upstream edge of the *SS* actuator and then decreases monotonically as the flow accelerates over the surface of the actuator. Similarly, on the pressure surface, there is a local pressure peak just upstream of the *PS* actuator which is followed by a steep, nearly linear decrease in pressure over the surface of the actuator. The trailing edge pressure for the modified, unactuated airfoil is substantially lower than for the smooth airfoil ($\Delta C_p = 0.5$) as a result of the local formation of separation bubbles downstream of the inactive actuators.

Perhaps the most remarkable effects of *SS* and *PS* actuation are the induced, bi-directional changes in pitching moment. Actuation on the suction or pressure surfaces of the airfoil induces flow acceleration over the actuator and a local low-pressure domain on either the top- or bottom-side of the trailing edge (Figure III-4b, $x/c = 0.85$ and 0.92, respectively). As a result, *SS* or *PS* actuation result in either nose-down or nose-up changes in the pitching moment as shown in Figure III-4d. These changes are proportional to the magnitude of the actuation as depicted in the gray traces between the pitching moment for the unactuated flow (in green) and full *SS* or *PS* actuation. The asymmetry between the magnitudes of the pitching moments induced by the *PS* and *SS* actuation is noteworthy. As shown in Figure III-4d, it appears that *PS* actuation is more effective as a result of the thinner boundary layer on the pressure side of the airfoil which enables the *PS* actuator to interact more strongly with the shear layer above the jet's exit plane. This asymmetry becomes more pronounced with increasing angle of attack. The changes in pitching moment are associated with corresponding changes in lift that are nearly uniform over the range of angles of attack considered here (Figure III-4c): *SS* actuation results in a small (about 0.1) increase in lift, while *PS* actuation results in a (potentially larger) reduction in lift (up to about 0.2).

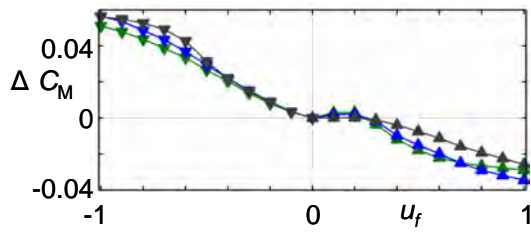


Figure III-5 The variation of the induced pitching moment increment ΔC_M with (normalized) actuation level u_f (*PS* \blacktriangledown , *SS* \blacktriangle) at $\alpha = -2^\circ$, 3° and 10°

noted above, the effectiveness of the actuation on the suction side decreases with increasing α and the magnitude of the maximum nose-down moment increment is about 60% of the corresponding nose-up moment on the pressure side.

The coupling between the actuators and the flow over the trailing edge is investigated using particle image velocimetry (PIV) measurements in the immediate vicinity of the actuator and the near wake. Figure III-6 shows time-averaged PIV images acquired at $\alpha = 3^\circ$ for the unactuated flow (Figure III-6b,e,h), and in the presence of full *SS* actuation ($u_f = 1$, Figure III-6a,d,g), and full *PS* actuation ($u_f = -1$, Figure III-6c,f,i). The fields plotted include concentrations of spanwise vorticity ω (Figure III-6a-c), 2D turbulent kinetic energy k (Figure III-6d-f), and the anisotropic turbulent fluctuations, $\overline{u'v'}$ (Figure III-6g-i) all of which are overlaid with velocity vectors. In the absence of actuation (Figure III-6b,e,h), the baseline flow separates locally over

The variation of the pitching moment (about $c/4$) with the amplitude of the actuation waveform u_f (normalized by the maximum actuation amplitude) over a range of angles of attack is shown in Figure III-5 ($-2^\circ < \alpha < 10^\circ$). While ΔC_M increases almost monotonically with u_f for *PS* actuation ($u_f < 0$), *SS* actuation ($u_f > 0$) exhibits some latency for $u_f < 0.2$ indicating a possible threshold in effectiveness that is presumably associated with the thicker boundary layer on the suction surface. As

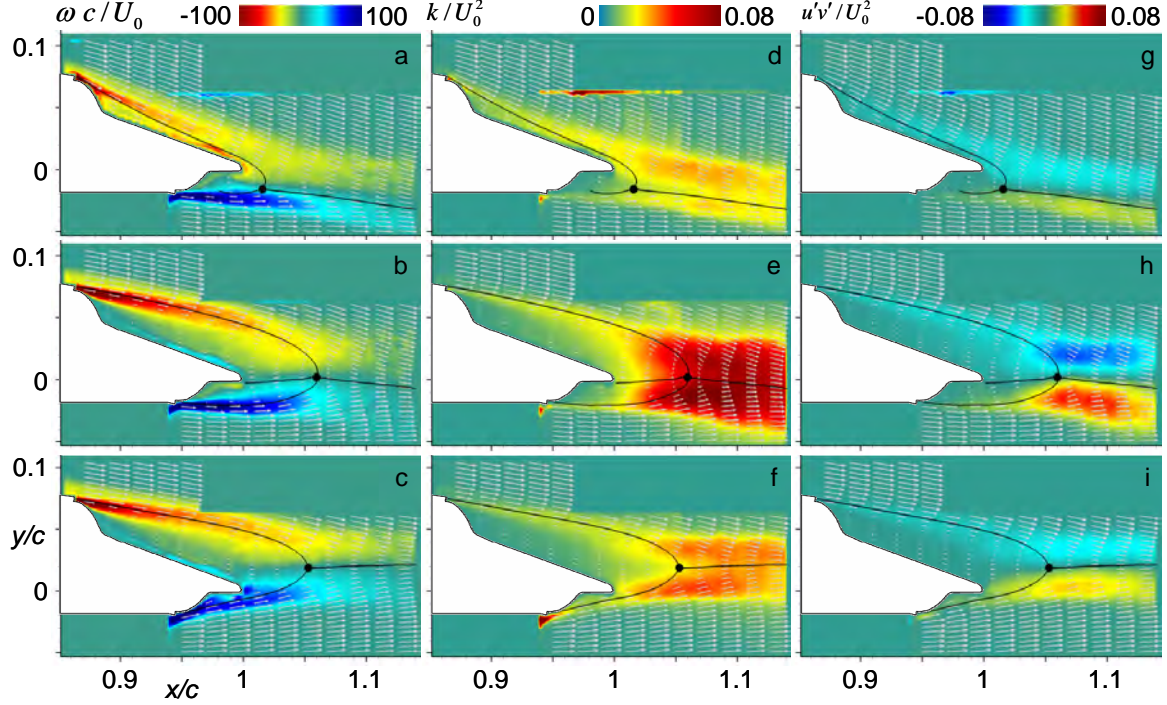


Figure III-6. Color raster plots of the time-averaged vorticity (a-c), turbulent kinetic energy (d-f) and anisotropic turbulent fluctuation (g-i) fields in the near wake with overlaid velocity vectors and stagnation streamlines at $\alpha = 3^\circ$ for SS actuation (a,d,g), no actuation (b,e,h), and PS actuation (c,f,i).

the downstream edge of each of actuators and forms a trapped vortex within the closed recirculation domains between each actuator and the trailing edge having the same sense (clockwise, CW in red or counter-clockwise CCW in blue) as in the upstream boundary layer. Although the flow near the surface of the airfoil upstream of the trailing edge is not fully resolved, it is possible to identify a CCW and CW vorticity layers near the suction and pressure surfaces, respectively that are induced by the upstream flow. As shown, these domains are bounded by a stagnation point downstream of the trailing edge. By regulating the size and strength of these trapped vortices it is possible to alter the pitching moments on the airfoil (cf., Figure III-4).

The (quasi-steady) actuation has a profound effect on the near wake. To begin with, when the SS actuators are engaged, the separated shear layer becomes attached to the curved (Coanda-like) surface downstream of the actuator, and the extent and strength of the recirculating (trapped) CW vorticity domain diminishes significantly. The near wake and the stagnation point are deflected downward (Figures III-6a) signifying an increase in lift (cf., Figure III-4b). The effect of PS actuation is symmetrically similar. As can be seen in Figure III-6c, PS actuation results in a significant reduction in the CCW vorticity domain upstream of the trailing edge and the near wake along with the stagnation point are deflected upward resulting in a decrease in lift. It is remarkable that both the SS and PS actuation leads to a significant reduction in the turbulent fluctuations in the near wake compared to the unforced flow (Figures III-6d-f). The turbulent kinetic energy k is diminished both in terms of its magnitude and also in terms of its cross stream extent indicating that the actuation leads to dissipative effects within the near wake and perhaps a significant reduction in shedding of discrete vorticity concentrations that are present in the absence of actuation. Similarly, the magnitude of the anisotropic turbulent fluctuations, $\bar{u}'v'$

diminishes compared to the distribution in the unactuated flow. This diminution (by nearly an order of magnitude) is more pronounced during *SS* actuation and may indicate that the near wake is more stable to external perturbations in the presence of the actuation. The vectoring of the wake as a result of the actuation is demonstrated by the “residual velocity” or the vector difference between the time-averaged velocity fields in the presence and absence of actuation (Figures III-7a and b). These data show that actuation results in acceleration of the flow over the actuator while slowing the flow on the opposite (unactuated) side of the trailing edge. These changes in momentum flux into the wake accompany the significant changes in the pitching moment that are induced by the actuation similar to the deflection of a conventional flap.

Sensitivity to Chordwise Actuator Position

The earlier investigations of DeSalvo and Glezer (2007) have indicated that the magnitude of the changes in pitching moment induced by *PS* actuation is sensitive to the streamwise (or chordwise) location of the actuators. This sensitivity was investigated in order to determine a locally-optimal actuation position with the goal of maximizing the control authority as may be measured for examples by pitching moment increment $\Delta C_M|_{u_f=1} - \Delta C_M|_{u_f=-1}$. An example of such optimization is shown in Figure III-8. While keeping the *PS* actuator in its reference configuration ($x_{PS} = 0.98c$), the *SS* actuator position is varied within the range $x_{SS} = c$ (i.e. flush with the trailing edge) and $x_{SS} = 0.83c$. Figures III-8a and b shows the variation of the pitching moment and pitching moment increment (relative to the unactuated airfoil) with the position of the *SS* actuator. These measurements are taken for a range of actuation power (showed in gray traces) up to full *SS* and *PS* actuation levels. As the *SS*

actuator is moved upstream from the trailing edge, the magnitude of the baseline pitching moment decreases nearly monotonically (i.e., becoming more nose-down). However, the magnitude of the actuation-induced pitching decreases faster with x_{SS} so that the net change relative to the unactuated airfoil increases with distance from the trailing edge and reaches a maximum $x_{SS} = 0.88$. It is noteworthy that moving the *SS* actuator affects not only its own performance but that of the *PS* actuator as well owing to the changes in the flow field near the trailing edge. In fact, as the *SS* actuator is moved upstream from trailing edge, the net nose-up pitching moment induced by the *PS* actuators increases as is evident in Figure III-8b,

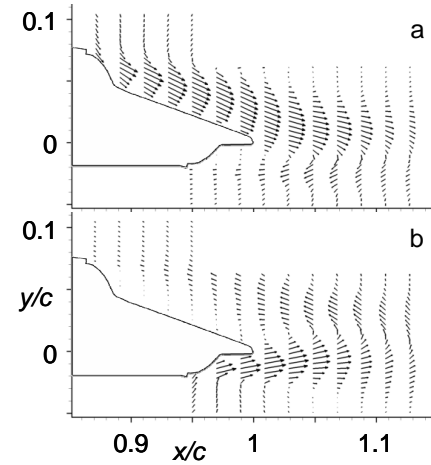


Figure III-7. Residual velocity vectors for (a) *SS* and (b) *PS* actuation.

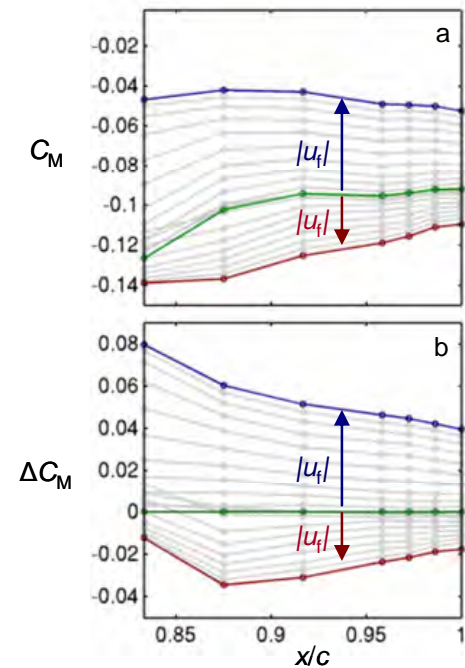


Figure III-8 Variation of C_M (a) and ΔC_M (b) with streamwise location of the *SS* actuator.

highlighting the coupling of the actuation effects across the trailing edge. Following these investigation, the actuators were placed at $x_{SS} = 0.88c$ and $x_{PS} = 0.97c$.

The corresponding lift and pitching moment increments ΔC_L and $\Delta C_{M,c/4}$ (relative to $c/4$) are plotted in Figure III-9 for all the available data (about 3,000 points) within the range $-1 \leq u_f \leq 1$; $-2^\circ \leq \alpha \leq 10^\circ$; $0.83 \leq x_{SS}/c \leq 1$; $0.96 \leq x_{PS}/c \leq 1$. It is remarkable that the entire data set collapses on a single linear distribution with a slope of $\Delta C_L/\Delta C_{M,c/4} = -3.2$. That different actuation effects, as manifested by changes in actuation position and actuation strengths at all angles of attack, collapse on a single curve, indicates that the increments in the lift and pitching moment are primarily affected by the strength of the trapped vorticity.

III.3. Transitory Actuation

The characteristic time scale associated with response of the flow to actuation is a crucial parameter for the implementation of real-time control and is investigated using step transitions between PS and SS actuation. Figures III-10a-f are a sequence of phase-averaged PIV images of spanwise vorticity maps (within the domain $0.16c \times 0.16c$ between the SS actuator and the trailing edge of the airfoil) following the onset of SS actuation from a previously unforced state. In the unactuated state (Figure III-10a), a shear layer extends roughly from the actuator orifice out over the trailing edge and exhibits a change in vorticity concentration that is commensurate with the change in surface geometry associated with the downstream end of the Coanda surface. Following the step onset of SS actuation, the upstream boundary layer over the actuator is pulled toward the surface causing the recirculating flow domain to partially collapse and significantly diminish. The collapse causes severing of the shear layer which is visible at $t = 0.13 T_{conv}$ (Figure III-10c). The severed shear layer rolls up and is advected downstream past the trailing edge (Figure III-10d-e, $0.2 T_{conv} < t < 0.26 T_{conv}$), and the flow downstream of the actuator

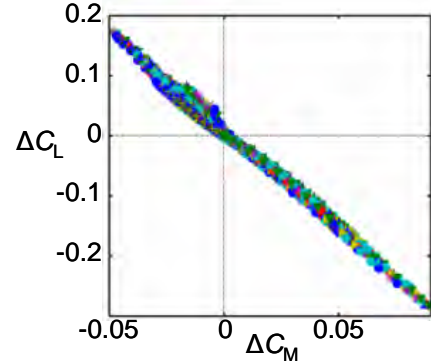


Figure III-9. Variation of actuation-induced increments in lift and pitching moment (about $c/4$) for a 3,000-point data set over a range of u_f , α , x_{PS} and x_{SS} .

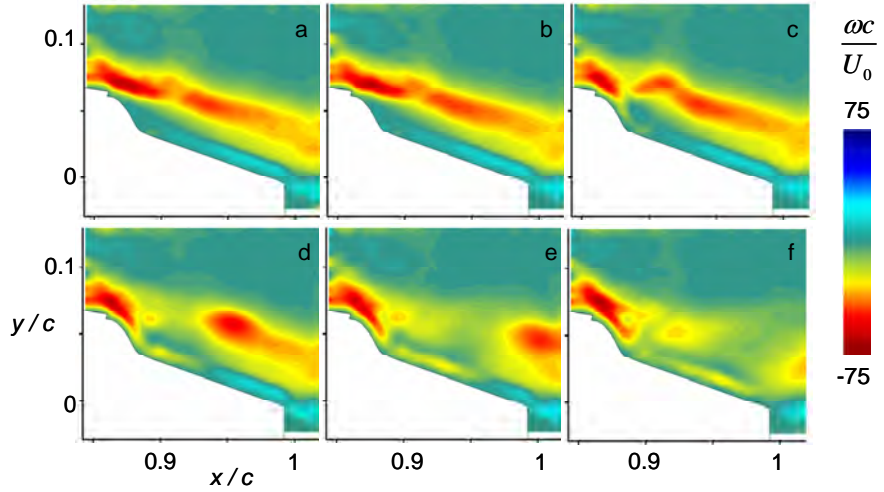


Figure III-10. Phase-averaged vorticity field downstream of the SS actuator following transition during stepped actuation from unactuated state to full SS actuation at $t/T_{conv} = 0$ (a), 0.07 (b), 0.13 (c), 0.2 (d), 0.26 (e), and 0.33 (f).

relaxes to the new “forced” state in which a thin boundary layer forms on the surface of the airfoil (Figure III-10f, $t = 0.33 T_{\text{conv}}$).

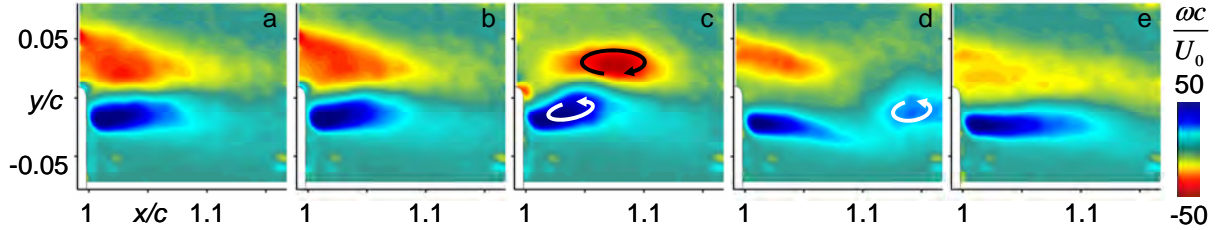


Figure III-11. Phase-averaged vorticity field in the near wake at $t/T_{\text{conv}} = 0$ (a), 0.2 (b), 0.4 (c), 0.6 (d), and 0.8 (e) following transition from no actuation to full SS actuation.

Additional details of the flow are observed just downstream of the trailing edge (Figure III-11, where the $0.16c \times 0.16c$ measurement domain is centered vertically on the trailing edge of the airfoil). As shown in connection with Figure III-6, in the unactuated state (Figure III-11a), the recirculation domains downstream of the actuators extend into the near wake and are manifested by concentrations of CW (red) and CCW (blue) vorticity. Following the onset of SS actuation and the collapse of the recirculation domain, the severed shear layer rolls up to a CW vortex which is shed and is advected downstream (Figure III-11c). Owing to the coupling between the recirculation domains downstream of the actuators, the shedding of the CW vortex is followed by the shedding of a CCW vortex (Figure III-11d), consistent with the lift increment associated with operation of SS actuators and the induced change in the nose-down pitching moment. In the last image (Figure III-11e, $t = 0.8 T_{\text{conv}}$), the shedding is complete and “trapped” CW and CCW vorticity concentrations are re-established downstream of the actuators as the wake relaxes to its new state.

In order to assess the time scales associated with the actuation process, the phase-averaged vorticity flux is computed by integrating the product of the streamwise velocity and spanwise vorticity in the cross-stream (y) direction at each streamwise (x) location for all times t . The resulting x - t diagram is shown in Figure III-12. The shed CW vortex is disconnected from the trailing edge at $0.25 T_{\text{conv}}$, is advected downstream at a speed (celerity) of $0.7 U_0$ and exits the measurement domain at $0.5 T_{\text{conv}}$. The x - t diagram also shows evidence of alternate shedding of weaker CW and CCW vorticity concentrations for the duration of the phase-averaged measurements. It is noteworthy that the shedding frequency corresponds to a dimensionless frequency of 3.8, which is the shedding frequency of the airfoil in the absence of actuation.

The vorticity flux downstream of the trailing edge ($x/c = 1.03$ (Figure III-13a) is integrated forward in time to obtain the time-history of the change in circulation about the airfoil during the

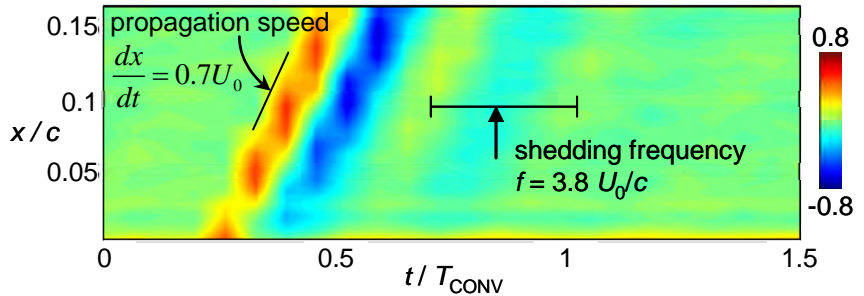


Figure III-12. x - t diagram of phase-averaged vorticity following the transition from unforced to full SS actuation.

The x - t diagram is shown in Figure III-12. The shed CW vortex is disconnected from the trailing edge at $0.25 T_{\text{conv}}$, is advected downstream at a speed (celerity) of $0.7 U_0$ and exits the measurement domain at $0.5 T_{\text{conv}}$. The x - t diagram also shows evidence of alternate shedding of weaker CW and CCW vorticity concentrations for the duration of the phase-averaged measurements. It is noteworthy that the shedding frequency corresponds to a dimensionless frequency of 3.8, which is the shedding frequency of the airfoil in the absence of actuation.

The vorticity flux downstream of the trailing edge ($x/c = 1.03$ (Figure III-13a) is integrated forward in time to obtain the time-history of the change in circulation about the airfoil during the

step change in actuation (Figure III-13). The initial shedding of CW vorticity concentration (cf., Figure III-11c) is associated with an initial reduction in circulation (at about $0.5T_{\text{conv}}$) that is followed by shedding of CCW vorticity concentrations which are accompanied by a circulation buildup about the airfoil ($t > 0.5T_{\text{conv}}$) until and settling at a new steady level.

Perhaps the most salient feature of the circulation time history is the indication that the entire flow over the airfoil readjusts within about $1.5 T_{\text{conv}}$, which is about two orders of magnitude shorter than the characteristic time associated with the controlled maneuver of the wind tunnel model. This illustrates that flow-control actuation can be typically effected on time scales commensurate with the flow's convective time scale, and that the maneuver response is limited by the inertia of the platform.

III.4.2-DOF Closed-Loop Control

Trajectory Tracking

One of the primary goals of this research was to elucidate the physical mechanisms associated with the dynamic coupling between trailing edge actuation and airfoil motion. The 2-DOF traverse system (Section III.1) affords a unique opportunity to explore the unsteady aerodynamics of the airfoil in the absence of flow control, and when the airfoil motion is either coupled with or driven by flow control actuation. The coupling between the actuation and the airfoil's motion was compared between two configurations. In the first configuration, the airfoil is commanded by the controller to track a trajectory in closed-loop using the flow control actuators while in the second the same trajectory is effected by the servo motor in the absence of actuation. In a set of experiments reported here, the airfoil was commanded to track a sinusoidal trajectory given by $\alpha = \alpha_0 + \alpha_1 \cdot \sin(2\pi ft)$ where $\alpha_0 = 3^\circ$, $\alpha_1 = 0.5^\circ$, and $f = 6.25$ Hz. Various parameters associated with the motion were recorded including the instantaneous angle of attack, α , angular acceleration, $\ddot{\alpha}$, torque $\tau_{\text{s,pitch}}$, vertical force on each side of the model, and flow control actuator command, u_f .

Figure III-14a and b shows phase-locked PIV images (at $\alpha_{\text{nominal}} = 2.84^\circ$ nose-up motion) of the flow near the trailing edge of the airfoil during closed loop tracking in pitch that is effected by the flow control actuators (III-14a), closed loop tracking in pitch when the pitching moment supplied externally by the servo torque motor (III-14b). Corresponding time-averaged PIV images for the stationary airfoil at the same angle of attack as in Figures III-14a and b are shown in Figures III-14c and d, with actuation (III-14c, when u_f is the same as in III-14a), and in the absence of actuation (III-14d). These data allow comparison of the unsteady flow dynamics (between the moving and stationary airfoil) in the presence and absence of actuation.

Perhaps the most striking feature of these fields is that, while there are significant differences between the dynamic and static vorticity fields under flow control, there is almost no visible difference between the dynamic and static images when the model is under servo control. The vorticity fields in Figures III-14a and c indicate that, although the actuation level of the SS actuators (at this phase) is the same ($u_f = 0.41$), the CW vorticity layer on the model is closer to the surface and the streamwise decay of the vorticity towards the trailing edge is stronger when

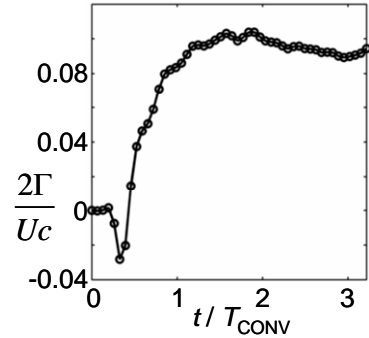


Figure III-13. Time history of change in circulation computed from integrated vorticity flux.

the airfoil is stationary (Figure III-14c). Note that the CW vorticity layer near the surface indicates a smaller recirculation domain. Furthermore, in concert with the nose-up motion of the airfoil, the CCW vorticity layer is tilted upward and the wake is wider compared to the stationary airfoil. In Figures III-14b and d, the actuators are inactive and the uncontrolled recirculation domains downstream of the actuators are clearly visible and appear to be almost identical regardless of the motion.

The dynamic effects of the two actuation modes on the velocity field in the near wake are assessed from the relative (or “residual”) velocity fields between the dynamic and the corresponding static distributions $\bar{u}_{\text{res}} = \bar{u}_{\text{dynamic}} - \bar{u}_{\text{static}}$ for flow and servo control (Figures III-14e and f, respectively). These data show that there are virtually no dynamic effects when the airfoil is controlled with the servo (cf., Figures III-14b and d). In contrast, under flow control, the wake is shifted upward and there is a reduction in the velocity over the suction side of the airfoil upstream of the trailing edge. Given that the SS actuators (which statically result in a downward vectoring of the wake) are active during this part of the maneuver, the upward tilting indicates a time lag between the actuator command and the aerodynamic forces that is indicative of the controller’s anticipation of the need to slow down the airfoil at the top of the sinusoidal trajectory. (Such a time lag is also evident in Figure III-16d.)

The differences between flow control and servo control are evident from measurements of (phase-averaged) cross stream distributions of the vorticity flux into the wake as shown in Figure III-15. These data are measured at $x/c = 1.06$ and for the four configurations in Figures 14a-d at five equally-spaced phases during the oscillation cycle. The most striking observation is that for all the phases shown the flux distribution is nearly identical for both the static and dynamic servo cases. This indicates that, in the absence of actuation, the structure of the near wake is not significantly affected by the motion of the airfoil. This is clearly not the case in the presence of actuation where in several cases, the flux distributions are substantially different between the

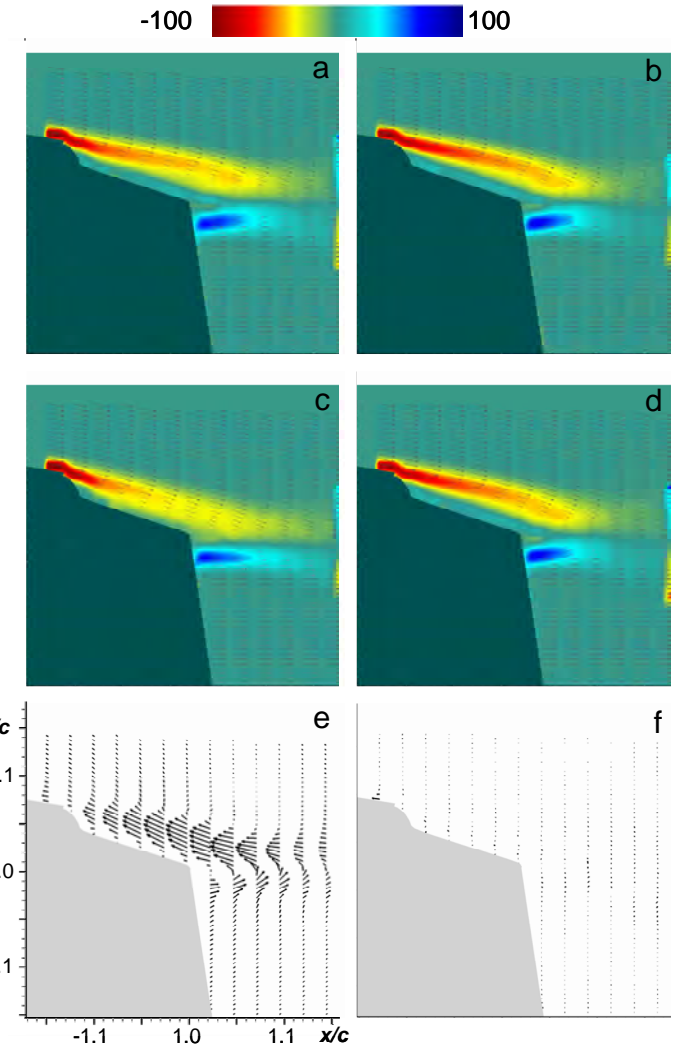


Figure III-14. Phase-averaged vorticity maps when the model is driven in pitch by flow control (a) and the servo (b) along with the corresponding maps for the static model (c and d, respectively). The relative velocity vector fields between the dynamic and static cases are shown in (e) and (f), respectively.

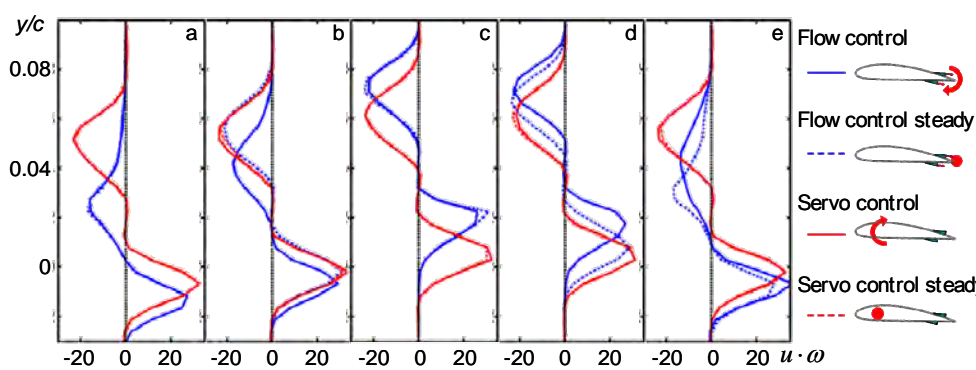


Figure III-15. Cross stream distributions of the vorticity flux through the wake at $x/c = 1.06$ for the dynamic (solid) and static (dashed) configurations of flow (blue) and external torque (red) control at five equally spaced phases during the cycle.

dynamic and static configurations (e.g., Figure III-15b, d, and e). Of particular note is Figure III-15b where the actuation command is nearly zero (i.e., neither actuator operational). As expected, the

vorticity flux for the static airfoil are nearly identical and coincide with the distribution of the dynamic servo control. However, even in the absence of (active) actuation, the vorticity flux for the airfoil that is moving under flow control deviates from the distributions for the static and servo-controlled model indicating that the actuation effects are sustained for some time when the actuation is turned off.

The time-dependent aerodynamic response of the airfoil to actuation with flow control and with external torque are shown in Figures III-16 a-e and f-j, respectively, during three cycles of the commanded attitude $\alpha(t)$. The realized attitude is shown in Figures III-16a and f, and the command signals to the actuators and torque motor are shown in Figures III-16b and g. Note that in both cases the instantaneous angular acceleration is used to reduce the effective moment

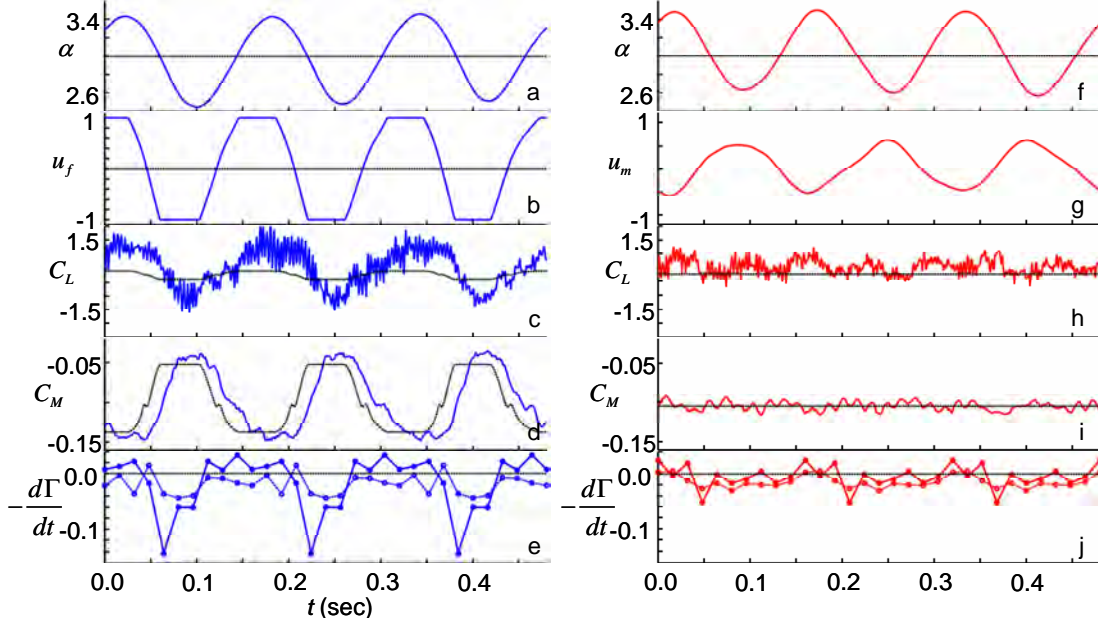


Figure III-16. Comparison of the time-dependent aerodynamic response of the airfoil to actuation with flow control (left column, a-e) and with external torque (right column, f-j): attitude α (a,f); actuator command u_f (a,g); lift $C_L(t)$; and pitching moment $C_M(t)$ (d,i). Phase-averaged: vorticity flux (e,j). Dotted black lines in (c,d,h,i) denote corresponding static values.

of inertia of the model (cf., Section III.2). The corresponding aerodynamic performance of the static airfoil (for each of the two actuation configurations) are also shown (in dashed lines) by using a look-up table of the static $C_M(\alpha, u_f)$ and $C_L(\alpha, u_f)$ that correspond to instantaneous $\alpha(t)$ and $u_f(t)$ of the dynamic configurations.

The instantaneous lift (Figure III-16c and h) is estimated from measurements of the reaction forces and the linear accelerations of the model $F_L = m \cdot \ddot{y}_{CM} - F_R$ where m is the mass suspended on the plunge servos (accounting for the airfoil model, pitch servo, and other hardware). These data show that the lift that is effected by flow control on the dynamically moving airfoil is significantly higher than the static lift at the same angles of attack and actuation amplitude. Furthermore, the lift obtained with servo pitch control has nominally the same magnitude (although not the same magnitude as the static lift). The instantaneous aerodynamic pitching moment (Figures III-16d and i) is estimated from the servo torque and angular acceleration, $M_{aero} = I_z \ddot{\alpha} - \tau_{s,pitch}$, where I_z is the moment of inertia about the pitch axis. The flat extremae in static C_M (e.g., $60 < t < 103$ ms and $146 < t < 186$ ms in Figure III-16c) correspond to the saturation of the control signal to the actuators (Figure III-16b). The dynamic pitching moment lags the static values by about $1.2T_{conv}$. This is indicative of the characteristic time scale that is needed for the flow to adjust to the changes in actuation. The corresponding traces for the servo-controlled model clearly show vanishingly small dynamic pitching moment which is produced by the actuators for the flow-controlled maneuver. Finally, the corresponding vorticity fluxes (computed from the PIV data) are shown in Figures III-16e and j. Note that the vorticity flux for the static airfoils (shown as dashed traces) should vanish, and the fluctuations reflect the measurement error. While there is little variation between the fluxes of the servo-controlled traces, there is a strong (negative) peak immediately following the transition from *SS* to *PS* actuation, which is consistent with a shedding of CW (negative) vorticity into the wake as the *SS* actuators are disengaged and the trapped vorticity is shed away.

Disturbance Rejection

An important aspect of the present work is the ability to demonstrate controlled rejection of momentary aerodynamic disturbances (e.g., gust) that is accomplished exclusively by flow control actuation. In the present experiments this was demonstrated using an external momentary force that was applied asynchronously through the force controller to simulate a sudden gust.

The applied disturbance corresponds to a momentary change in lift $\Delta C_L = 0.52$ (corresponding to a static change in angle of attack of $\Delta\alpha = 5.9^\circ$) with a nominal duration of $10T_{conv}$. The disturbance waveform is generated by applying a second order low-pass filter with a natural frequency of 25 rad/sec to a square-wave type pulse with the desired amplitude and duration. The response of the wind tunnel model to an upward disturbance is shown in Figure III-17. The filtered pulse disturbance command, $C_{L,cmd}$, is shown in Figure III-17a. The peak force applied by the force controller ($\Delta C_L = 0.52$) is delayed by approximately $4T_{conv}$ relative to the disturbance command. As the model begins to accelerate upward (Figure III-17b), the flight controller responds by commanding pitch down using *SS* actuation ($5 < t/T_{conv} < 15$, Figure III-17d) to decrease the angle of attack (Figure III-17c) and the corresponding lift force. After the model is accelerated upwards by the disturbance force, it begins to move down at $t/T_{conv} = 20$ and the controller rapidly commands pitch up using the *PS* actuation ($20 < t/T_{conv} < 40$) to stabilize the model at the original trim condition.

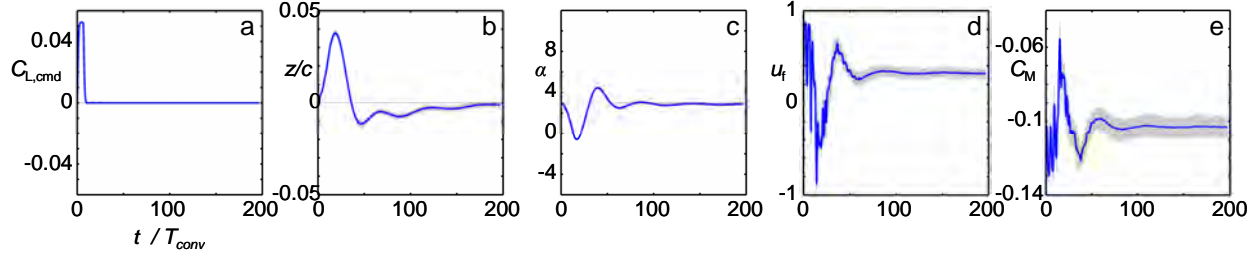


Figure III-17. System response to a disturbance input: (a) disturbance waveform (b) plunge (c) pitch angle (d) actuation input and (e) pitching moment.

The response time of the actuators is critical for maintaining stability under strong and rapid disturbance forces. These data show that while the total settling time is about $150T_{\text{conv}}$, the full change in pitching moment effected by the actuators in response to the disturbance is achieved within $3T_{\text{conv}}$ of the onset of the disturbance. Throughout the response, it is remarkable how closely the dynamic pitching moment tracks the actuator input command.

III.6. Summary

Closed-loop feedback control was used in a wind tunnel investigation to effect commanded 2-DOF maneuvers of a free airfoil *without moving control surfaces*. The airfoil model is free to move in pitch and plunge, and an inner closed-loop controller is used to reduce its apparent inertia and prescribe its aerodynamic characteristics. Bi-directional changes in the pitching moment over a range of angles of attack are effected by controllable, nominally-symmetric trapped vorticity concentrations on both the suction and pressure surfaces near the trailing edge. Attitude stabilization and position control of the model is achieved by closing the position loop through the flow control actuators using a model reference adaptive controller designed to maintain a specified level of tracking performance in the presence of disturbances, parametric uncertainties and unmodeled dynamics associated with the flow.

The formation, evolution, and regulation of controlled trapped vorticity concentrations that are engendered by hybrid flow control actuators were investigated in detail using high-resolution phase-locked PIV and force and moment measurements. The resulting changes in pitching moment and lift were used to effect maneuvering of an airfoil model in two degrees of freedom, and the dynamic interaction of the flow control actuation and the unsteady flow about the maneuvering airfoil was investigated in detail. It was shown that the vehicle dynamics and the fluid dynamics (under actuation) are closely coupled and simultaneously affect each other, and consequently the aerodynamic forces and vorticity flux affected by flow control actuation during a prescribed maneuver are significantly different than the corresponding forces during a similar maneuver that is effected by external forces. The characteristic transitory response to rapid (step) change in actuation was investigated and it was demonstrated that the changes in aerodynamic forces and moments owing to flow control actuation are effected on time scales that are commensurate with the flow's convective time scale. This and the controller's response to dynamic disturbance rejection indicate that flow control actuation can be typically applied much faster than with conventional control surfaces and therefore can be exploited for rapid maneuvering that is only limited by the platform's inertia.

IV. Reduced-Order Models

Two classes of vorticity-based reduced-order models (ROMs) of the flow to be controlled have been developed. The discrete-vortex (DV)- and proper orthogonal decomposition (POD)-based models both use dynamical variables directly related to the vorticity distribution. The choice of vorticity as a dependent variable is appealing for flows in which vorticity is confined to a) separated vortex structures near the airfoil, b) trapped vorticity concentrations resulting from control inputs, and c) vorticity in the boundary layer. For both the DV- and POD-based approaches, the starting point is the vorticity transport equation (obtained by taking the curl of the Navier-Stokes equations) describing the evolution of the vorticity field in an incompressible fluid.

IV.1 Discrete-Vortex Based Reduced-Order Model

IV.1.1 Introduction

Two-dimensional unsteady airfoil theory for incompressible flows has had a history that spans nearly a century. The primary motivation for this work stems from a long interest in the prediction of unsteady forces and moments for the flight control of aircraft and understanding and suppression of aeroelastic phenomena, for example the flutter of aircraft wings. Although the use of two-dimensional potential theory, including wake vorticity, is a major simplification for the actual aerodynamics of thin bodies, it nevertheless gives insight into the underlying aerodynamic mechanism of unsteady aerodynamics. The simplifications in complexity lead to a tractable problem that can usually be handled by standard mathematical approaches and limited computing resources.

Building on earlier work of Wagner (1925), Theodorsen (1935), and others, von Kármán and Sears (1938) developed a consistent method to compute unsteady lift and moment based on the integral equation for the instantaneous strength distribution of a continuous vortex sheet in the wake. Sears (1941) applied the method to several applications. A thorough review of the theories of von Kármán and Sears, Wagner, and Theodorsen, and can be found in Bisplinghoff et al. (1955).

More recently there has been renewed interest centered on using approximations of Wagner and Theodorsen functions. In particular, Edwards et al. (1979) derived generalized Theodorsen functions relating motions of the circulatory part of the airloads to the motion of the airfoil and applied it to subcritical and supercritical flutter conditions. Peters (2008) gives additional information on several finite-state models predicting forces and moments in the frequency domain, although one major drawback of these methods is that they cannot be integrated into a fully coupled simulation of the fluid-structure interaction. In addition, these models are rather mathematically complicated and in most cases are only manageable for prescribed or assumed oscillatory motions.

Here, we describe the development of a vortex-based discrete-order model for arbitrary thin airfoil motion with trailing edge control using synthetic jet actuators (Glezer and Amitay, 2002; Brzozowski, 2009). The goal was to produce a model suitable for use in an adaptive control scheme. Therefore, the model had to have reasonably accurate predictive capabilities at a very modest computational cost. First, a tractable and simple aerodynamic model is presented that predicts the forces and moment on a thin airfoil undergoing arbitrary motions in the absence of any actuation. This model is reduced to the solution of a single nonlinear ODE, and is validated with both experimental results and detached-eddy simulation numerical testing. Extensions to

the model are then given that allow for trailing-edge actuation and results from this extended model are compared to experimental results using an experimental apparatus that simulates free flight of an airfoil.

IV.1.2 Aerodynamic Model

Here, a model that is capable of predicting the forces and moments on an unactuated two-dimensional airfoil in motion is developed. We follow closely the theory outlined in von Kármán and Sears (1938) to make the development as concise and clear as possible, but include important modifications to account for *any* airfoil motion as long as it remains small amplitude, as explained later in this subsection.

Consider the incompressible flow around a thin airfoil of chord length c in a free-stream with an upstream velocity U_∞ that flows from left to right. The airfoil undergoes an arbitrary motion in both plunge and pitch defined by the body variables y_b and α , respectively. The pivot point for the rotational degree of freedom is located at $x = -a$ as shown in Figure IV.1-1.

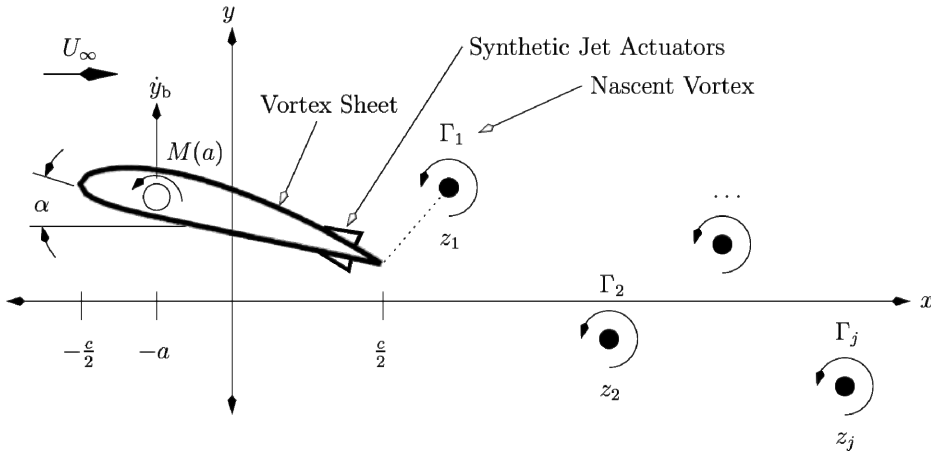


Figure IV.1-1 Schematic (not to scale) of the unsteady vortex dynamics model of an airfoil undergoing arbitrary motion in the presence of a freestream velocity and trailing edge actuation. The trailing edge actuation consists of a synthetic jet actuator oriented tangent to the ramp-like structure depicted. We note that the vortex strengths will typically have alternating signs although here they are depicted to clarify the convention that positive circulation results in a vortex that rotates in the counter-clockwise sense.

We model the unsteady motion of the airfoil by allowing the shear layer to separate into the wake as discrete and singular elements of vorticity with circulation strength Γ_j at location $z_j = (x_j, y_j)$. Trailing-edge actuation is represented by the two ramp-like structures shown in Figure IV.1-1. When switched on, the actuation traps a local concentration of circulation near x_c on the respective side of the airfoil near the synthetic jet being actuated, inducing a local suction peak and global pressure change due a shift in the location of the Kutta condition as discussed in §IV.1.4.

Several assumptions are made so that a simple, closed-form, low-order model can be created to predict the forces and moment on a thin airfoil. The assumptions are listed and explained as follows:

- i. The flow is considered high Reynolds number flow so that the boundary layer is sufficiently thin and viscous effects can be neglected. It is also assumed that the fluid

outside the boundary layer remains irrotational except at the discrete points z_j . Vorticity is shed into the wake to satisfy the unsteady Kutta condition at a specific separation point on the airfoil. Except for actuation of trailing-edge control, the separation point is at the trailing edge of the airfoil. With actuation, the separation point is slightly shifted from the trailing edge (see §IV.1.4).

- ii.* Motions of the thin airfoil are considered small-amplitude so that leading-edge separation does not occur. This means that the characteristic motions in plunge must be $h/c \ll 1$ and $1/U_\infty dh/dt \ll 1$, where h is a characteristic length of the maneuver. In pitch, this translates to $\alpha \ll 1$ and $d\alpha/dt \ll U_\infty/c$. Even when this is not the case, evidence in Lewin and Haj-Hariri (2005) suggests that for a range of high-frequency parameters (say with reduced frequency $k > 5$, where $k = 2\pi c f / U_\infty$ and f is the frequency of oscillation) leading-edge separation, although present, becomes reabsorbed into the boundary layer and subsequently separates off the trailing edge. Leading-edge separation in these instances does not affect the lift and moment characteristics as critically as does trailing-edge separation. In addition, the small-amplitude assumption allows another drastic reduction in complexity. For small-amplitude motions, the departure of any wake vortex elements in the transverse direction are considered small, and thus the effect of transverse motion can be justifiably neglected. Thus, the wake vortex dynamics can be sufficiently restricted to their advection in a single dimension, and the bound vorticity can be assumed to lie on the x -axis.
- iii.* It is assumed that the leading-order unsteadiness of the thin airfoil can be modeled by the motion of a flat plate. To take into account the effects of thickness and camber, the lift and moment are modified in a quasi-steady fashion, that is, steady characteristics versus angle of attack (AOA) are superimposed on the unsteady results for nonideal airfoil shapes. This allows a general theory that is applicable to the entire class of thin airfoils with very minor modification using tabulated data, for instance, from Abbott and Deonhoff (1959).
- iv.* The effect of actuation can be modeled by the trapping of one macro control vortex element with strength Γ_C located at x_C and a shift in the location of the Kutta condition. When the pressure side (suction side) actuator is switched on, $\Gamma_C > 0$ ($\Gamma_C < 0$).

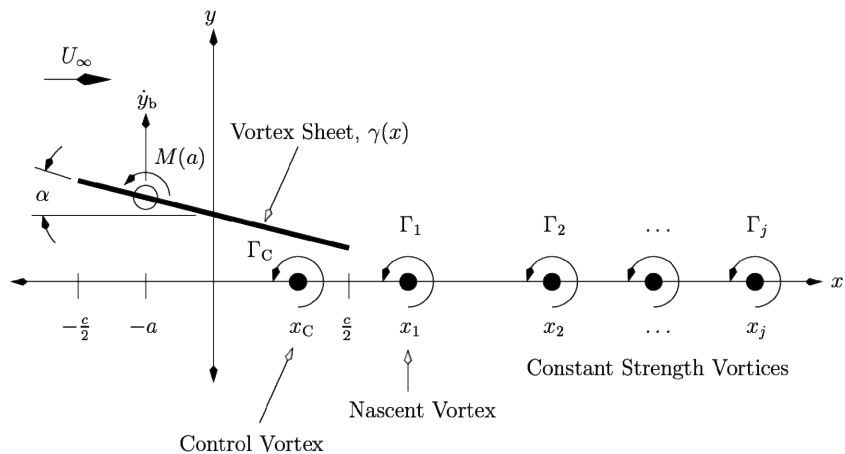


Figure IV.1-2 Schematic of the quasi one-dimensional simplification of Figure IV.1-1 after the application of assumptions given in §IV.1.2.

These assumptions allow us to solve the drastically simplified problem depicted in Figure IV.1-2, where the flat-plate airfoil and its subsequent separated vortex elements now effectively lie on the x -axis. The details of the control vortex will be discussed in §IV.1.4, and are omitted from the model description until then.

The subsequent analysis may be summarized as follows. Full details are given in Tchieu and Leonard (2011). The distribution of bound circulation on the flat plate may be decomposed into three components, due to (1) wake vorticity, (2) pure rotational motion about midchord, and (3) pure plunging motion. The no-through-flow condition on the plate yields three integral equations for these three components. Imposition of the Kutta condition at the trailing edge allows the determination of a unique analytical solution for each of these component distributions. All wake vortices for $j \geq 2$ (i. e., except for the nascent vortex $j = 1$) travel downstream with speed U_∞ relative to the airfoil and have constant circulation. The time-dependent circulation of the nascent vortex is determined by satisfying the constraint that the circulations of all vorticity components must sum to zero. In the model, circulation that is shed from the airfoil to satisfy this constraint immediately appears at the location of the nascent vortex at $x = x_1$, rather than at the trailing edge, $x = c/2$. To compensate for this, so that zero net lift is experienced by the airfoil due to this assumption, the speed of the nascent vortex is adjusted away from U_∞ accordingly (see Tchieu and Leonard, 2011). The consequence is that only a single nonlinear ODE for $x_1(t)$ must be solved to implement the model. New nascent vortices are formed when $d\Gamma_1/dt$ is such that the amplitude of the nascent vortex is no longer increasing, i. e., vortices are not allowed to “unwind”. Finally, the lift and moment on the airfoil are found by using conservation of linear and angular impulse in vorticity form.

As a result the lift and moment coefficients predicted by the uncontrolled, discrete-vortex reduced-order model are given by

$$C_L = \pi \left(-\frac{c}{2U_\infty^2} \ddot{y}_b - \frac{2}{U_\infty} \dot{y}_b + \frac{ac}{2U_\infty^2} \ddot{\alpha} + \frac{2a+c}{U_\infty} \dot{\alpha} + 2\alpha \right) - \frac{1}{U_\infty} \sum_{j=1}^N \frac{\Gamma_j}{\sqrt{x_j^2 - \frac{c^2}{4}}} \quad (1)$$

$$C_M(a) = -\frac{a}{c} C_L + \pi \left(-\frac{\pi}{2U_\infty} \dot{y}_b - \frac{c^2}{64U_\infty^2} \ddot{\alpha} - \frac{a}{2U_\infty} \dot{\alpha} - \frac{1}{2} \alpha \right) - \frac{1}{4U_\infty} \sum_{j=1}^N \frac{\Gamma_j}{\sqrt{x_j^2 - \frac{c^2}{4}}} \quad (2)$$

IV.1.3 Validation of the Uncontrolled Reduced-Order Model

The reduced-order model is compared to experimental results and numerical results of a NACA 4415 airfoil undergoing unsteady pitch and plunge (see Muse et al., 2008, for experimental details). The nominal values used here are $C_{L,0} = 0.4$ and $C_{M,0} = -0.1$.

For the experimental test performed at Georgia Tech, the airfoil was pitched near quarter-chord at a free-stream Reynolds number, $Re = 9 \cdot 10^5$, on a prescribed trajectory with the amplitude and frequency both functions of time, as seen on the left side of Figure IV.1-3.

As seen in Figure IV.1-3(left), a sinusoidal chirp signal was fed into the experiment such that the reduced frequencies spanned the range from $0.057 < k_{pitch} < 0.068$ ($0.60 \text{ Hz} < f_{pitch} < 0.71 \text{ Hz}$). The angular speed of the airfoil was kept constant. Given in Figure IV.1-3(right) is the comparison of lift and moment between the model and experimentally measured quantities. The agreement between the experimental measured lift and the model lift is excellent. The experimentally measured moment (low-pass filtered), shows slight departures from the model

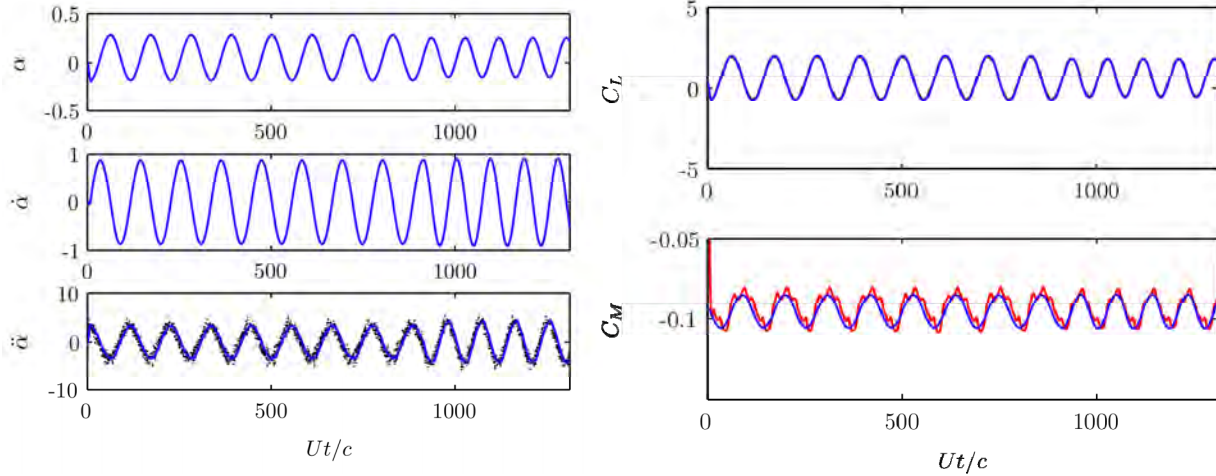


Figure IV.1-3 Comparison with experimental results for lift and moment for a NACA 4415 airfoil pitching about its quarter chord. Left: Input data (in radians) from experiment (dotted, unfiltered $d^2\alpha/dt^2$). Reduced frequencies range from $0.057 < k_{pitch} < 0.068$ ($0.60 \text{ Hz} < f_{pitch} < 0.71 \text{ Hz}$). Right: The experimental response (red) and the current model response (blue). Experimental results for C_M were filtered with a Butterworth filter to remove high frequency noise. Experimental results for C_L are nearly identical to the model results.

although the magnitude, frequency, and phase of the dominant mode of oscillation is very well predicted. The differences between the two probably originate from excessive noise in measuring the angular acceleration. The agreement seen here is typical for frequencies $f_{pitch} < 1 \text{ Hz}$.

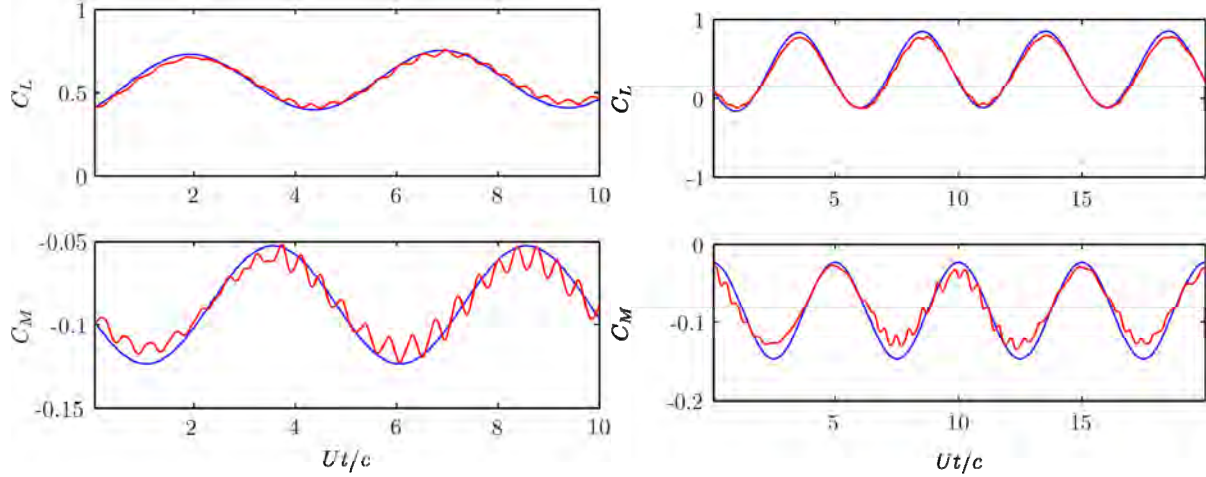


Figure IV.1-4 Comparison of the model response (blue) to DDES (red) for lift and moment for a NACA 4415 airfoil. Left: purely pitching about its quarter chord with $k_{pitch} = 1.256$ and $0^\circ < \alpha < 2^\circ$. Right: purely plunging with $k_{plunge} = 1.256$ and $h = 0.2$.

Due to the limitations of the experimental facilities, numerical simulations were used to validate models in situations not realizable by experimentation. In particular, much higher pitch and plunge rates were investigated. The numerical simulations presented here were computed at the University of Texas at Austin using delayed detached-eddy simulations (DDES) by Lopez (2009) (see also Lopez et al., 2009).

Figure IV.1-4(left) shows the comparison between numerical simulation and the low-order model pitching sinusoidally at a fixed frequency, $k_{pitch} = 1.256$, which is more than two orders of magnitude higher than the experimental case. The agreement here is quite acceptable given the simplifications made. We notice that the simple low-order model cannot capture the small-scale

oscillations that lie on top of the gross lift and moment signatures. These high-frequency oscillations can be explained by high-frequency vortex shedding off the nonsharp trailing edge. This causes a small-amplitude von Kármán street to be shed from the trailing edge for all our operating conditions, and typically introduces a small asymmetry in the small-scale waveform due to its turbulent nature. The low-order model does not capture such an effect because of the prior assumptions made in §IV.1.2, but the model does capture the salient features, accurately reproducing the lift and moment amplitudes, phase, and phase shift at the dominant frequency.

Figure IV.1-4(right) similarly shows the comparison for a fixed plunge angular frequency, where the airfoil heaves sinusoidally with an amplitude $h = y_{b,\max}/c = 0.2$. Again, the same trend is seen where we have the small-scale von Kármán shedding producing a small-scale, high-frequency signature in the lift and moment. The results are still quite satisfactory in producing the essential characteristics in the lift and moment due to the plunging motion.

IV.1.4 Extension of the Model to Include Control

The effect of synthetic jet actuators can be viewed as trapping vorticity in the boundary layer near the actuation location, with consequent changes in the local and global behavior of the flow. Since the product of the actuation frequency and the convective time is much greater than unity, this trapped vorticity is modeled as a macro vortex element, held stationary to represent the localized confinement observed in experiments. Thus, we place a control vortex at $x = x_C$ to reproduce the effect of the actuator. When the *SS* actuator is turned on, a negative (clockwise) vortex is formed on the *SS*. When the *PS* actuator is turned on, a positive vortex is formed on the *PS*. The circulation of the control vortex depends on the control variable, u_C , for example,

$$d\Gamma_C/dt = J(u_C, \Gamma_C)$$

From experiments (see DeSalvo and Glezer 2006 and the §II above), it is known that the formation time of the control vortex is much less than the convective time scale. Thus, we assume that the control vortex strength is given by the functional form, $\Gamma_C = \Gamma_C(u_C)$, with a possible dependence on the AOA as well. The determination of this function will be addressed later in this subsection.

In addition, we argue that the Kutta condition for the sharp trailing edge of the model is violated slightly due to actuation. Given in Figure IV.1-5(left) is a C_p plot from DDES computations of Lopez (2009). Not only is the airfoil pressure near the actuator affected by the actuator device, but there is apparently a shift in the separation point at the trailing edge that affects the global pressure distribution around the airfoil as seen in the figure. To substantiate this assertion, we determined analytically the change in pressure distribution observed on a Joukowski airfoil due to an added bound circulation or, equivalently, a shift in the location of the Kutta condition. The result is shown in Figure IV.1-5(right) to display the same global trend evident in the simulations shown on the left. Thus, it is found necessary to add an additional bound circulation in the model such that the location of the Kutta condition is shifted slightly to match the computational and experimental results.

The distribution of circulation on the airfoil to satisfy these constraints can be written as

$$\gamma_C(x) = \Gamma_C \delta(x - x_C) + \frac{\lambda \Gamma_C}{\pi \sqrt{\frac{c^2}{4} - x^2}}$$

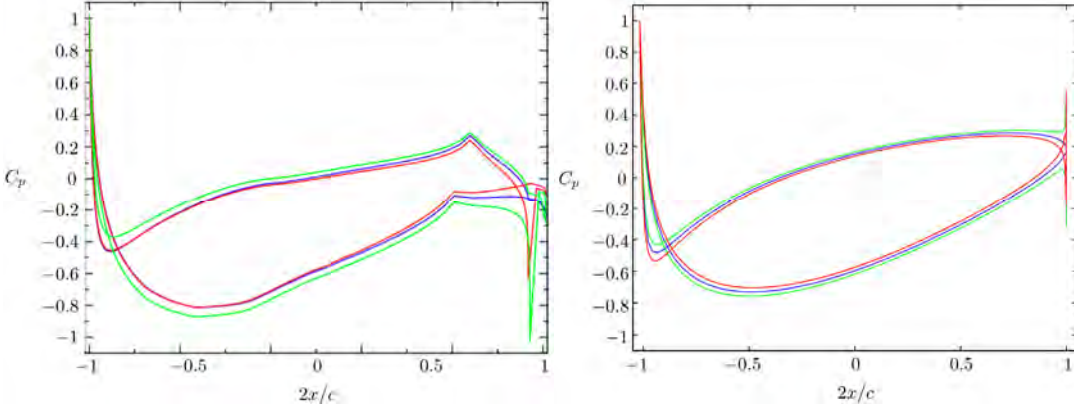


Figure IV.1-5 Numerical and theoretical evidence for shift in the location of the Kutta condition due to synthetic jet actuation. Airfoil at $\alpha = 8^\circ$. Left: Pressure distributions around the airfoil with and without actuation from the simulations of Lopez (2009). Right: The theoretical pressure distributions around the airfoil with and without shifts in the location of the Kutta condition for a Joukowski airfoil in potential flow. Given is the baseline case with no actuation or shift (blue), suction side actuation turned on or slight clockwise shift (red), and pressure side actuation turned on or slight counterclockwise shift (green).)

where λ is a fitting parameter. Note that the distribution of circulation on the airfoil represented by the first term on the RHS violates the necessary boundary conditions, but its effect is small since the strength of the control vortex is also small. The second term adds a uniform rotation of the flow that slightly shifts the location of the Kutta condition in the model to account for fluid motion, to wrap around a nonsharp trailing edge in the physical flow. It is only present for the control vortex and is absent in all subsequently shed vortices.

Subsequent analysis shows that with the addition of the control vortex, the lift and moment equations are also modified to include the effect of the actuation so that Eqs. (1) and (2) become

$$C_L = \pi \left(-\frac{c}{2U_\infty^2} \ddot{y}_b - \frac{2}{U_\infty} \dot{y}_b + \frac{ac}{2U_\infty^2} \ddot{\alpha} + \frac{2a+c}{U_\infty} \dot{\alpha} + 2\alpha \right) - \frac{1}{U_\infty} \sum_{j=1}^N \frac{\Gamma_j}{\sqrt{x_j^2 - \frac{c^2}{4}}} - \frac{2(1+\lambda)\Gamma_C}{U_\infty c} \quad (3)$$

$$C_M(a) = -\frac{a}{c} C_L + \pi \left(-\frac{\pi}{2U_\infty} \ddot{y}_b - \frac{c^2}{64U_\infty^2} \ddot{\alpha} - \frac{a}{2U_\infty} \dot{\alpha} - \frac{1}{2}\alpha \right) - \frac{1}{4U_\infty} \sum_{j=1}^N \frac{\Gamma_j}{\sqrt{x_j^2 - \frac{c^2}{4}}} + \frac{2x_C\Gamma_C}{U_\infty c^2} \quad (4)$$

To determine the parameter λ and the relationship between voltage input, u_C , and the trapped circulation strength, Γ_C , static tests were performed. First, λ was determined by performing experiments to measure the change in moment and lift due solely to the actuation. In steady state, Eqs. (3) and (4) show that the ratio of the incremental lift coefficient to the incremental moment coefficient is given by

$$\frac{\Delta C_L}{\Delta C_{M,\frac{c}{4}}} = \frac{(1+\lambda)}{(1+\lambda)\frac{a}{c} + \frac{x_C}{c}}$$

and therefore gives a means of determining λ .

From experimental data given in Figure IV.1-6(left), we find indeed that the slope depicted is nearly constant for all conditions when varying the control input from $-1 < u_C < 1$ and AOA's in the range $-10^\circ < \alpha < 10^\circ$. This is not only true for the current configuration, but for several configurations with different actuator locations (Brzozowski, 2009). The slope of the least-

squares linear fit of the data provided in this figure is $\Delta C_L / \Delta C_{M,c/4} = -2.59$. Solving for λ (recall $a/c = 1/4$ and $x_C/c = 0.45$) leads to the value of $\lambda = 2.31$. This parameter is held constant for all operating conditions as long as the configuration of the airfoil remains the same.

A functional relationship for $\Gamma_C(u_C, \alpha)$ is obtained using the same data for generating Figure IV.1-6(left). Note that the actuators are not simultaneously turned on. Therefore a convention is chosen such that $u_C > 0$ turns on the SS actuator and $u_C < 0$ turns on the PS actuator. From Eq. (4), we can use steady data to determine the necessary vortex strength as

$$\frac{\Gamma_C}{U_\infty c} = \frac{\Delta C_{M,\frac{c}{4}}(u_C, \alpha)}{2[(\frac{1}{4}(1 + \lambda) + \frac{x_C}{c}]]}$$

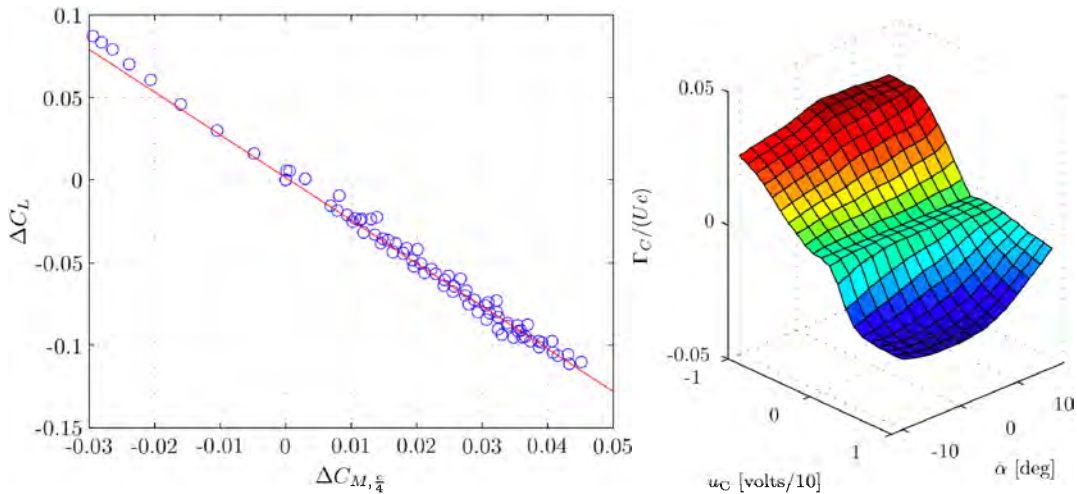


Figure IV.1-6 Detail plots for the determination of λ and Γ_C . Left: Change in lift versus the change in moment due to a control input for various control input strengths ($-1 < u_C < 1$) and AOAs ($-10^\circ < \alpha < 10^\circ$). Shown are the results from the experiments (blue circles) and a linear fit (red) given by $\Delta C_L / \Delta C_{M,c/4} = -2.59$. Right: Relationship between Γ_C , u_C , and α . A positive voltage turns on the SS actuator (negative turns on the PS actuator). Both actuators cannot be simultaneously on.

The functional relationship is plotted in Figure IV.1-6(right). For moderate AOA, $-10^\circ < \alpha < 10^\circ$, the dependence on α is slight compared to the dependence on u_C ; nevertheless, that dependence is retained to help counteract the unmodeled effects of leading-edge separation. From this data, a lookup table was constructed and then used to acquire $\Gamma_C(u_C, \alpha)$ for model simulations of the airfoil dynamics with control.

IV.1.5 Comparison Between Controlled Experiment and Model

The model equations with the control vortex effects are now compared to experimental results with control. For this case, the airfoil is controlled by the torque motor to hold a specific AOA, but with a loosely-tuned controller such that a sufficient control input produces an obvious response in the AOA of the airfoil. A simulation of the model was created in MATLAB Simulink, accounting for the airfoil dynamics described by the model presented in subsection IV.1.2 with the additional actuator modeling and parameters determined earlier in §IV.1.4. Additionally, the dynamics of the experimental setup undergoing pure pitching airfoil motion is included.

The controller is first set to hold the airfoil at $\alpha = 3^\circ$. Several doublet commands are given to the synthetic jet actuators, each of different duration as seen in Figure IV.1-7(left), and since the controller is nonaggressive, the airfoil moves substantially. The experimental response (red) and the model response (blue) are given in Figure IV.1-7(right). The model equations do a very good job of simulating the experimental response. A major difference between the simulation and the experiments is that the model airfoil dynamics tend to relax to the original position at a much faster rate. This is most likely attributable to the unmodeled and excessive damping in the experimental apparatus (Muse et al., 2009). Further application using adaptive control with a linearized version of the current model is discussed in Muse et al. (2009) and in §I above.

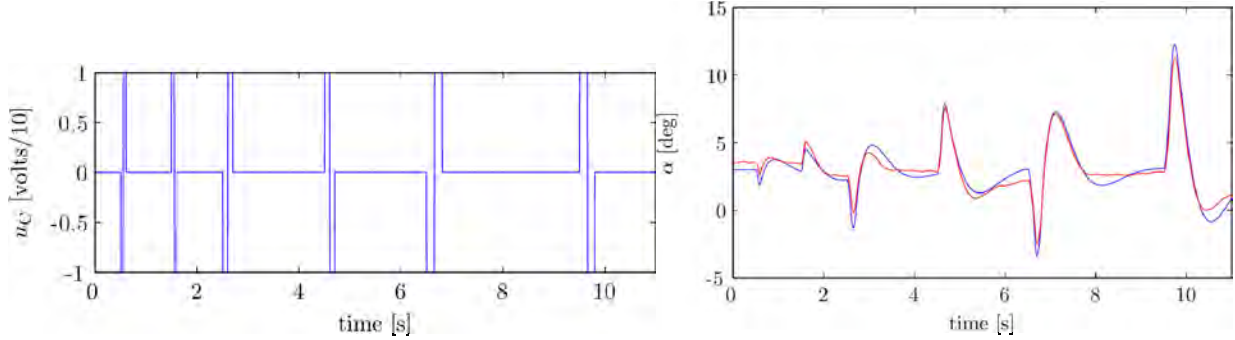


Figure IV.1-7. Comparison of test bed simulation with experimental results. Left: Input command signal given to both the simulation and the experiment (Tchieu et al., 2008). Right: Airfoil response due to control input: (blue) current model; (red) experiments.

IV.1.6 Summary

A one-equation aerodynamic model has been created for use in an adaptive control scheme. The model predicts the unsteady lift and moment of an airfoil undergoing arbitrary unsteady motions in pitch and plunge, with arbitrary time-dependent control input. The major assumptions are that the airfoil is at very high Reynolds number and that it does not experience leading-edge separation at any instant, thus allowing a simplified model for the wake dynamics. The wake dynamics and airfoil circulation distributions are then used to generate expressions for lift and moment. The resulting equations for lift and moment are then adjusted accordingly for application to airfoils with thickness and camber.

The model is compared to experiments performed at Georgia Tech and delayed detached-eddy simulations performed at UT Austin, both for a NACA 4415 wing section at high Reynolds number. The results are quite promising, given the number of assumptions used to simplify the model. For low reduced frequencies in pitch and plunge, the model gives a good prediction of the aerodynamic lift and moment. For high reduced frequencies, the agreement is still quite acceptable. Small-scale high-frequency vortex shedding is not captured because of the simplicity of the model. However, the impact of such a phenomenon is expected to be minimal from a controls standpoint.

The aerodynamic model is further extended using the concept of trapped vorticity to model the synthetic jet actuators for airfoil control. The augmented model is then implemented in a simulation of the experimental apparatus, and its comparison to experimental results give good agreement. As described in §I above, the vortex-based model was implemented into an adaptive control scheme with considerable success.

IV.2 POD-Based Reduced-Order Models

Several approaches were pursued in the context of POD-based ROMs. Here, we discuss time-domain and frequency-domain approaches, as well as an approach based on using temporal coefficients (of POD modes) extracted from experimental data to construct quadratically-nonlinear ODE models of the flow.

IV.2.1 Proper Orthogonal Decomposition (POD) in the Time Domain

We first attempted to construct an ROM from the flow field in the airfoil wake by performing a POD for the unsteady flow field in the time domain for one cycle of the airfoil motion, using phase-averaged PIV measurements of the streamwise and cross-stream velocity components. Using the spanwise vorticity component constructed from these measurements, the basic idea was to project the vorticity transport equation onto a series of vorticity POD modes computed from the experimental data, and to account for actuation by adding a source term in the resulting ODE system.

We computed vorticity POD modes using measurements of two velocity components from PIV data at Georgia Tech. Figure IV.2-1 shows the three fundamental POD modes computed from the vorticity data, and the corresponding velocity modes “slaved” to them through two-dimensional continuity and the definition of the spanwise vorticity. As POD modes, the vorticity modes are orthogonal, whereas the velocity modes are not. This approach allows us to substitute these vorticity modes and the associated velocity modes into a modified vorticity transport equation, and to obtain an ODE system by Galerkin projection.

The decomposition to POD modes has shown that more than 95% of both enstrophy and kinetic energy of the flow are captured by the first three modes. In the wake of the airfoil at one time instant, Figure IV.2-2 shows a comparison of the spanwise vorticity field a) extracted from

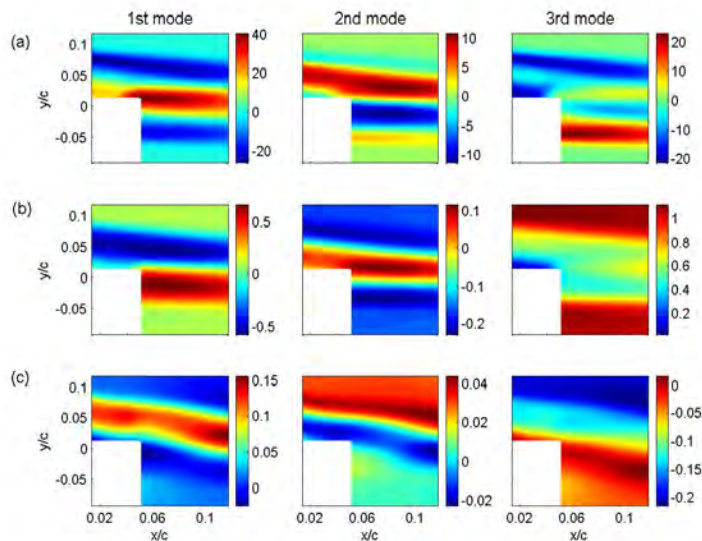


Figure IV.2-1 Three fundamental POD modes of (a) spanwise vorticity, (b) streamwise velocity and (c) cross-stream velocity.

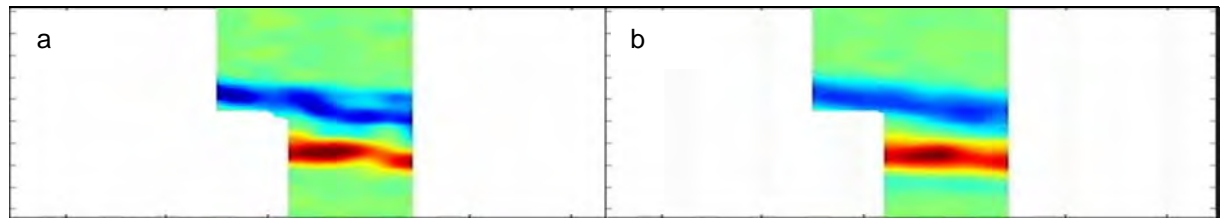


Figure IV.2-2 Vorticity from (a) experimental data and (b) reconstructed from three POD modes

experimental data and b) reconstructed from three POD vorticity modes. This result implied that an ODE system of size three might very well be sufficient for a reduced-order model.

Nevertheless, implementing the above approach had three problems. First, accounting for actuation due to the control inputs was not straightforward, since the POD modes were computed for a flow which was periodically forced. Second, it was noted

that the actuation had a small effect compared to the statistically stationary unactuated wake flow. Subtracting the time-averaged flow field (in a frame attached to the airfoil) from any instantaneous velocity field gave a result one order of magnitude smaller than the time-averaged field (Figure IV.2-3). Therefore, accounting for the complete flow field, a large part of which is the unactuated flow, would be a major source of error, given that the main objective was to focus on the effect of actuation on the flow rather. Finally, although the airfoil itself is essentially two-dimensional, the spanwise nonuniformity of the actuation introduces enough spanwise nonuniformity into the flow that neglect of the spanwise velocity component results in as much as a 30% “error” in using the two-dimensional continuity equation for even the phase-averaged flow. Since no data were available for the spanwise velocity component, this was not feasible. For these reasons, other approaches described below were pursued.

IV.2.2. POD in the frequency domain

Using a POD in the *frequency domain*, we have developed a new approach for constructing a forced ODE system for use as a ROM of flow over an actuated airfoil. The starting point of this approach is separating the time-dependent part of the flow in the airfoil wake, which is due to the actuation commands, from the mean (statistically stationary) wake flow. The approach is based on the realization that the effect of actuation on the flow field is small compared to the unactuated flow. Figure IV.2-3 shows the time-averaged vorticity field (in a frame attached to the airfoil), and an instantaneous field after subtraction of the mean. It is evident that the time-dependent part is about one order of magnitude smaller than the mean.

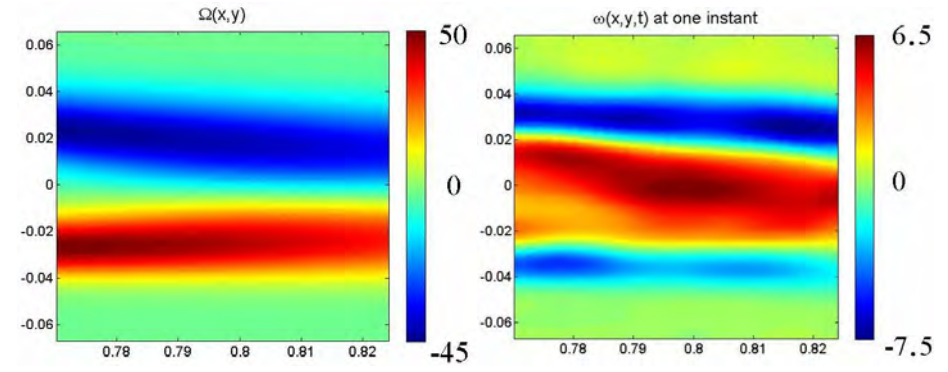


Figure IV.2-3 Mean vorticity field Ω (on left), and the instantaneous vorticity field after subtraction of the mean (on right).

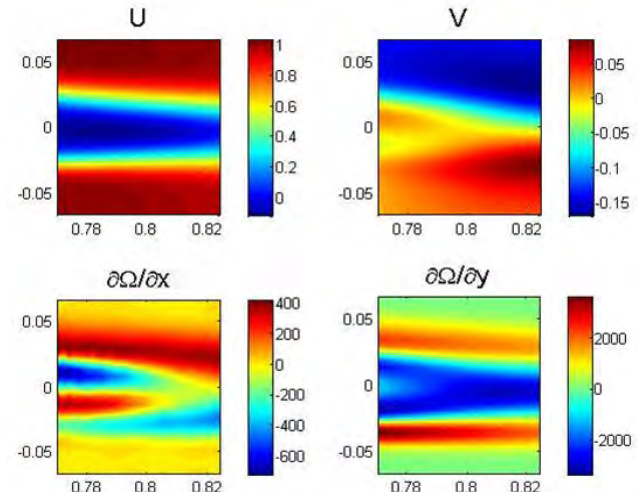


Figure IV.2-4 Mean flow velocity components U and V , and x,y -vorticity derivatives.

Linearizing about the mean flow results in a linear partial differential equation (PDE) system, consisting of the vorticity transport and continuity equations, with the unknowns being deviations of the velocity and vorticity components (and their derivatives) from the mean (given by the time-averaged flow fields obtained from Georgia Tech PIV data). Figure IV.2-4 shows time-averaged velocities and spatial derivatives of the spanwise vorticity used in the linearized vorticity transport equation for the actuated flow. Using instantaneous inlet conditions from the experimental data, we use a spectral method to compute the *impulse response* of that PDE system in the frequency domain for a wide range of frequencies. The numerical solutions are approximated by constructing a finite number of frequency-based vorticity POD modes, and the corresponding (slaved) velocity modes.

Figure IV.2-5 shows the three fundamental POD modes for the vorticity (top) and streamwise velocity (bottom), to the right of their corresponding inlet conditions. (As POD modes, the vorticity modes are orthogonal, whereas the velocity modes are not.) The decomposition allows us to substitute these vorticity and velocity modes into a forced, linearized, unsteady vorticity transport equation, and to obtain an ODE system by Galerkin projection, in which only the forcing terms are frequency-dependent (and can be parameterized from experimental data, based on the mechanism of vorticity-generation by the actuators).

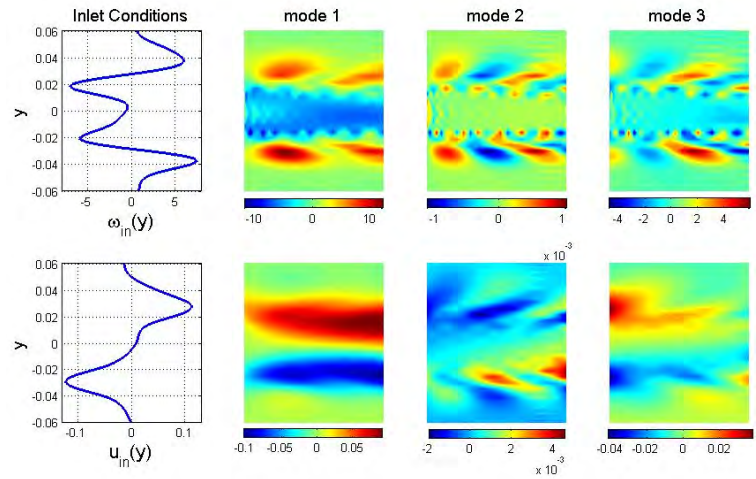


Figure IV.2-5 Three frequency-based POD modes from impulse response PDE solution (on right) with corresponding inlet conditions from experiment (on left) for spanwise vorticity (top) and streamwise velocity (bottom).

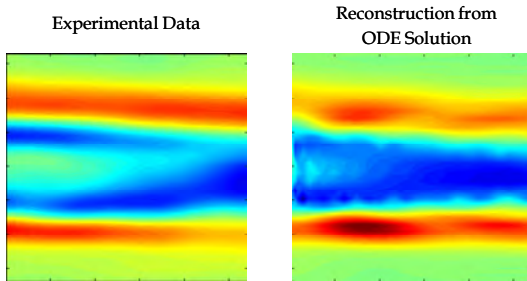


Figure IV.2-6 Validation of ODE model comparing reconstruction from ODE solution to experimental data of identical inlet conditions.

Figure IV.2-6 presents a validation of the ODE model, based on three POD modes and on three instantaneous inlet conditions. The left plot shows the experimental vorticity field (at one instant) for specific inlet conditions, while the right plot shows the vorticity field reconstructed from the solution of the ODE system forced by the same inlet conditions as in the experiment.

The reduced-order model discussed above has been developed based on two-dimensional flow measurements (for the mean flow representing the unactuated flow). In practice the actuation for the airfoil is three-dimensional since it is done by multiple piezo-disks along the airfoil span, as can be seen in Figure IV.2-7. However, the data from the experiments can be generalized to a three-dimensional model as well. To that end, three-dimensional effects in the flow have been examined by considering, for a fixed airfoil, the two measured (x and y) components of the velocity field from experimental data acquired at

three spanwise locations. Figure IV.2-7 shows these three spanwise locations when the cover plates of the piezo-disks are removed. A simple model that accounts for three-dimensionality has been considered, and provides good qualitative prediction of the vorticity at one of the spanwise locations, based on data at the two other locations. The model is based on the assumption that the spanwise variation of the flow is periodic in the spanwise direction, and the leading harmonic term of that periodicity is considered. Using measurements at two different spanwise locations, we calculate the vorticity due to actuation (ω_n) at a third location. Figure IV.2-8 shows a comparison between the calculated vorticity by using that model at such a third location (z_3), based on two given locations (z_1 and z_2) and the vorticity from measurements at that same location.

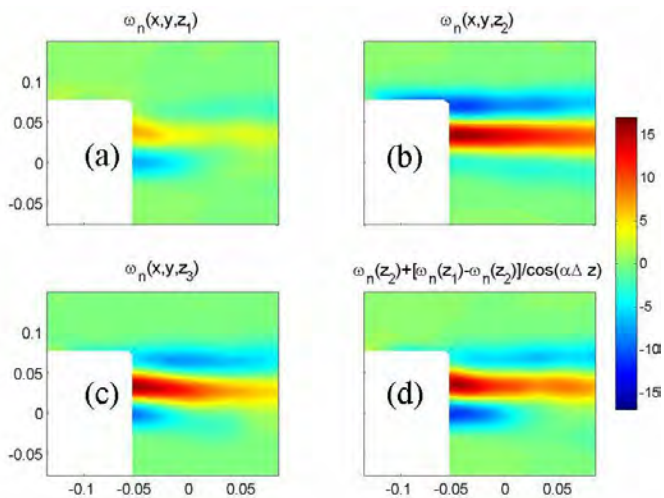


Figure IV.2-8. (a)-(c) Measured vorticity at spanwise locations z_1-z_3 , respectively. (d) Calculated vorticity at z_3 , using data at z_1 and z_2 with the proposed model (where the primary harmonic periodicity is $\pi/4$).

compute the *impulse response* of that PDE system in the frequency domain over a wide range of frequencies. The numerical solutions are approximated by constructing a finite number of spatially and frequency-based vorticity POD modes, each with its own (nonorthogonal) streamwise and cross-stream velocity modes. (As POD modes, the vorticity modes are orthogonal; the velocity modes, which are derived from them using a Poisson equation based on the relationship between velocity and vorticity in a two-dimensional solenoidal flow, are not orthogonal). This double decomposition allows us to adjust the size of the ODE system to accommodate flows with varying spatial and temporal complexity, depending on the strength and time-dependence of the actuation.

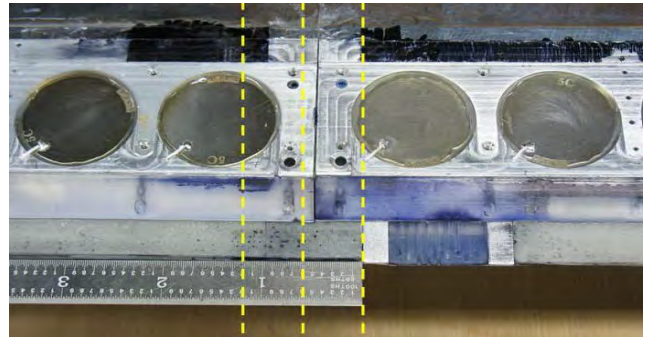


Figure IV.2-7 Coverplates removed showing piezo-disk locations along the airfoil span.

We have elaborated our frequency domain POD approach to POD in both the frequency domain and in space. As previously, we first separate the time-dependent part of the flow in the airfoil wake, due to actuation, from the mean (statistically stationary) wake flow. Using the vorticity transport and continuity equations (in which pressure does not appear), we linearize about the mean wake flow and get a linear PDE, in which the unknown dynamical variables are deviations of the velocity components and vorticity from the mean (given by time-averaged flow fields generated from PIV data at Georgia Tech). Using instantaneous upstream inlet conditions from the experimental data, we use a spectral method to

Figure IV.2-9 shows the first three POD modes for the primary spatially decomposed term. The vorticity (top) and streamwise velocity (bottom) are shown, to the right of cross-stream profiles of the corresponding streamwise velocity profiles at the upstream inlet. The decomposition allows us to substitute these vorticity and velocity modes into a forced linearized time-dependent vorticity transport equation, and to obtain an ODE system by Galerkin projection, in which only the forcing terms are frequency-dependent (and can be parameterized from

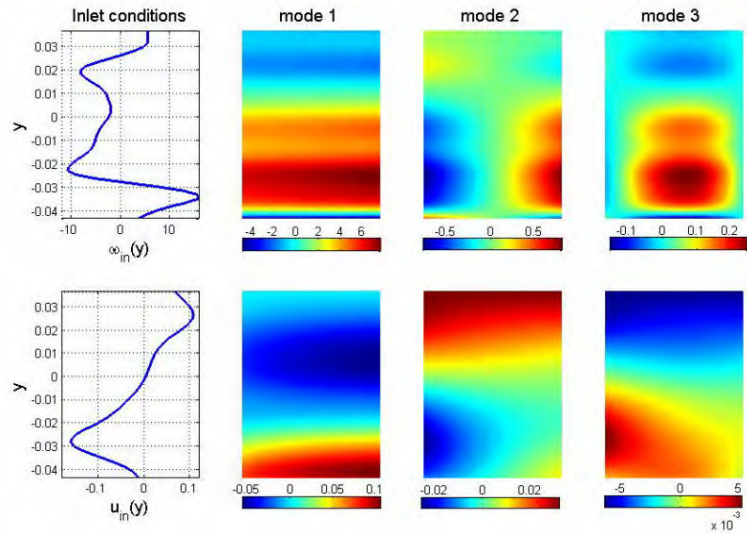


Figure IV.2-9. First three frequency-based POD modes from impulse response PDE solution (on right), with corresponding experimental inlet conditions (on left) for spanwise vorticity (top) and streamwise velocity (bottom).

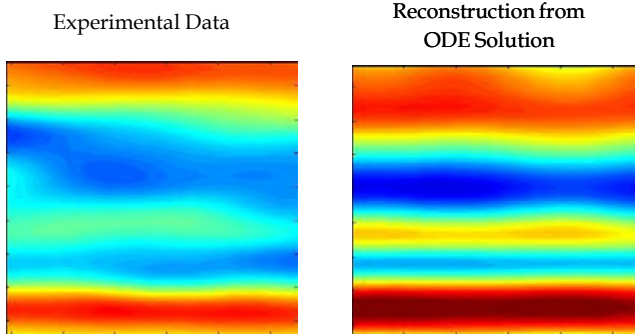


Figure IV.2-10. Validation of ODE model by comparing reconstruction from ODE solution to experimental data having identical inlet conditions.

experimental data, based on the mechanism of vorticity-generation by the actuators). The resulting ODE system has been validated by comparing the predictions of the flow it reconstructs to experimental data. Figure IV.2-10 presents a validation of the ODE model, based on six POD modes and on two instantaneous inlet conditions. The left plot shows the experimental vorticity field (at one instant) for specific inlet conditions, while the right plot shows the vorticity field reconstructed from the solution of the ODE system forced by the same inlet conditions as in the experiment.

IV.2.3. Construction of Reduced-Order Models from Measurements of POD Coefficients

Methods based on projection of the Navier-Stokes equations onto a functional basis obtained by proper orthogonal decomposition (POD) of a velocity field has become a popular technique for obtaining reduced-order models from the Navier-Stokes equations.

In many flows of interest (such as for the synthetic-jet actuated airfoil), however, experimental data are available only over a limited portion of the domain. For example, PIV data might be available only in (a small part of) the wake. Worse still, in some cases the only experimental data available are pressure measurements on the surface of a body. (This is especially likely to be true in flight applications, where measurements of the flow velocity in the volume of the fluid are problematic.) In such cases, development of reduced-order models of the flow, based on projection of the Navier-Stokes equations onto global POD modes, will require that the POD modes be determined either in separate experiments, or from computational results.

To address this problem, we have developed an approach that uses limited experimental data to generate quadratically-nonlinear ordinary differential equation (ODE) systems, that can be used as reduced-order models of the flow. A key point is that the resulting ODE system has as its dependent variables the same quantities whose experimental measurements were used to generate the model.

This section begins with a discussion of how the approach is used to generate a quadratically-nonlinear ODE system when the underlying dynamics are those of an autonomous (unforced) quadratically-nonlinear ODE system, and then discusses the situations in which the underlying dynamics are a quadratically-nonlinear differential-algebraic equation (DAE) system, and finally a system of nonautonomous (actuated) partial differential equations (PDEs).

First, we consider the situation where the underlying dynamics consists of an N -dimensional system of quadratically-nonlinear ODEs of the form

$$\frac{dx_i}{dt} = f_i(x_1, x_2, \dots, x_N), \quad 1 \leq i \leq N \quad (1)$$

where each f_i depends quadratically on the dependent variables. This is exactly the case corresponding to discretization of the incompressible Navier-Stokes equations, in which the only nonlinearity is associated with the convective acceleration term.

In experiments, we typically do not know the details (and sometimes not even the structure) of the right-hand side (RHS) of (1). For example, much of chemical kinetics is described by equations of the form (1), in which rate constants are typically not known. In what follows, we show how measurements of the dependent variables x_i can be used to systematically construct the RHS of (1).

We initially assume that the dependent variables can be measured without noise, and that the dimension N of the underlying dynamical system is equal to the number of variables measured, which we call N_m . In that case, we seek to determine the "best" choice for the coefficients a_i , b_{ij} , and c_{ijk} (referred to below as "the coefficients") in the system,

$$\frac{dx_i}{dt} = a_i + \sum_{j=1}^{N_m} b_{ij} x_j + \sum_{j=1}^{N_m} \sum_{k=1}^j c_{ijk} x_j x_k, \quad 1 \leq i \leq N_m \quad (2)$$

using measurements of variables at discrete times, denoted by $x_{i,e}(t_l)$, for $1 \leq i \leq N_m$ and $1 \leq l \leq N_t$. The number of coefficients is $N_m + N_m^2 + N_m^2(N_m + 1)/2$. We note that the inner summation of the last term on the RHS omits terms of the form $c_{ijk} x_j x_k$ for $k > j$, thus eliminating nearly half of the coefficients.

Conventionally, this is done by an iterative process, in which a) values of the coefficients are guessed or estimated, b) a set of initial conditions is chosen, c) the system (2) is integrated forward in time, and d) some measure of the difference between the computed trajectory and the experimental data, say

$$E_1 = \sum_{l=1}^{N_t} \sum_{i=1}^{N_m} [x_{i,e}(t_l) - x_i(t_l)]^2, \quad (3)$$

is used to iteratively adjust the coefficients, until E_1 is minimized.

This approach has several drawbacks. First, it requires a set of initial conditions, which is not always known. Second, it is an iterative approach and is essentially nonlinear, since each difference in the sum (3) depends nonlinearly on the coefficients. As a result, E_1 might have multiple local minima, and if it does, there is no guarantee that the global minimum will be found. Third, since the approach is essentially nonlinear, it is possible that convergence to the "correct" set of coefficients might be possible only for a very limited set of initial conditions and initial guesses/estimates for the coefficients. In other words, the "region of attraction" in the combined space of initial conditions and coefficients might be very small.

For these reasons, we seek a different approach to determining the coefficients in (2). Instead, we seek to minimize a different measure of the error, namely

$$E_2 = \sum_{l=1}^{N_t} \sum_{i=1}^{N_m} \left[a_i + \sum_{j=1}^{N_m} b_{ij} x_{j,e}(t_l) + \sum_{j=1}^{N_m} \sum_{k=1}^j c_{ijk} x_{j,e}(t_l) x_{k,e}(t_l) - \frac{dx_{i,e}(t_l)}{dt} \right]^2, \quad (4)$$

where $dx_{i,e}(t_l)/dt$ represents an approximation to the time derivative of the measured variable $x_{i,e}$ at time t_l . For economy of notation, we define $x_{i,l} = x_{i,e}(t_l)$ and $\dot{x}_{i,l} = dx_{i,e}(t_l)/dt$. This error represents the sum (over all times at which measurements were made) of the sum (over all of the ODEs) of the squared "residuals" in the differential equation system (2). As such, it is a measure of how well the experimental data (and their time derivatives) satisfy the differential equations (2), rather than how well the experimental data match numerical solutions of (2) subject to some set of initial conditions. We note that if the data are noiseless, and are generated by a quadratically-nonlinear ODE system of dimension N_m , then E_2 will vanish identically when the coefficients have been properly determined.

The approach (4) has several distinct advantages. First, as we will discuss below, the coefficients are determined by differentiating E_2 with respect to each coefficient. Since E_2 depends quadratically on each coefficient, this reduces to a linear least-squares problem. Second, since we are not comparing trajectories, we do not need to find the "correct" initial conditions corresponding to those used to generate the experimental data.

We seek the (global) minimum of (4) by differentiating with respect to the coefficients and setting the results equal to zero, giving a system of $1 + N_m(N_m + 3)/2$ equations *linear* in the coefficients. A key feature is that no initial conditions are needed, and the numerical problem is a linear one.

It is easily shown that unless the number of time points at which the data are sampled satisfies $N_t \geq 1 + N_m(N_m + 3)/2$, the linear equation system described above will be undetermined. However, satisfaction of this inequality does not guarantee that the matrix will have full rank. This is easily seen by considering the situation in which the time series of the measured variables are T -periodic, and are sampled at the period T . In that case, all of the points are sampled at the same point in the phase space, there is only one set of measured variables, and the rank will be one.

Moreover, computational experience, both with ODE systems having known coefficients, as well as with temporal coefficients extracted from a POD decomposition of the pressure distribution

on the surface of a circular cylinder in Karman vortex flow at $Re = 100$, shows that sampling at a large number of distinct points in the phase space does not guarantee that the matrix has full rank. While this might initially seem surprising, there is in fact a good underlying reason. When the underlying ODE system has two long-time solutions, say a steady solution and a limit cycle, each with its own region of attraction in the space of initial conditions, and the experimental data are obtained on a trajectory corresponding to an initial condition lying in the region of attraction of the steady solution, the full dynamics will remain inaccessible, no matter how many points are sampled on that trajectory. In fact, computational evidence shows that when more than one long-time attractor exists, it is necessary to choose initial conditions in the region of attraction of each of them, in order to fully capture the dynamics.

We have tested this approach on several ODE systems, as well as on the temporal coefficients extracted from a POD decomposition of the pressure distribution on the surface of a circular cylinder in Karman vortex flow at $Re = 100$. In the former case, it accurately recovers the coefficients used to computationally generate the numerical "data," while in the former case, it produces ODE systems consistent with the dynamics, and allows good reconstruction of the computed pressure distributions. The method is undergoing continued development, with emphasis on forced (e.g., actuated) systems, as well as systems described by nonlinear differential-algebraic equations (DAEs).

IV.2.4. Summary

Vorticity-based ROMs were developed by performing a proper orthogonal decomposition (POD) on the spanwise vorticity obtained from particle-image velocimetry measurements of the streamwise and cross-stream velocity components in the Georgia Tech wind tunnel. Careful processing of the data revealed that the spanwise nonuniformity of the synthetic jet actuation introduced phase-averaged spanwise velocities large enough to produce 30% "errors" when the two-dimensional continuity equation was applied to the phase-averaged flow in the wake of the nominally two-dimensional airfoil. A second approach used a POD in the frequency domain to develop a reduced-order model of flow over an actuated airfoil. An ROM based on this approach was used to predict the flow past an actuated airfoil, and the results compared favorably with velocity and vorticity data from the Georgia Tech wind tunnel, as well as with CFD results from UT Austin. Finally, an approach was developed in which temporal coefficients of POD modes (extracted from experimental or computational data) can be used to construct a ROM consisting of a set of quadratically-nonlinear ODEs.

V. Computational Fluid Dynamics

To enable reduced-order model development and to characterize the fluid dynamics of the controlled flows, we developed computational fluid dynamic (CFD) models of controlled airfoils using synthetic jet (SJ) actuators. Our CFD model was built on the Stanford CDP code (Ham and Iaccarino, 2004), which is an unstructured finite-volume incompressible flow solver. To support the flow control simulations performed here, several additional elements were required, including:

i. Appropriate turbulence model. The RANS models in CDP were not adequate because of the flow separation phenomena inherent in the actuator design, and the dynamics of the interactions with the SJs. Instead, delayed detached eddy simulation (DDES, Spalart et al. 2006), which is a RANS/LES hybrid based on the Spalart-Allmaras (1994) RANS model, was implemented in CDP, and used in the simulations reported here. For our problem, DDES has the advantage of simulating the large-scale dynamics of separating shear layers.

ii. Model for the synthetic jet actuators. The SJ actuators were modeled by introducing an SJ cavity into the flow domain, with geometry approximating that of the actual actuators. An oscillating blowing and suction boundary condition was then introduced on one wall of the cavity. It was found that the size of the cavity could be substantially reduced if the geometry of the actuator outlet slot was preserved (Lopez, 2009). The strength of the blowing and suction was calibrated to match the changes in lift and moment induced by the actuator (Lopez, 2009) at zero angle of attack in the Georgia Tech experiments. As shown in Figure V-1, once actuator strength was set at zero angle of attack, the change in lift and moment at other angles of attack also agreed with experimental observations.

While accurately representing the physics, this actuator model is computationally intensive since it requires temporal resolution of the actuator time scale, which is an order of magnitude smaller than other

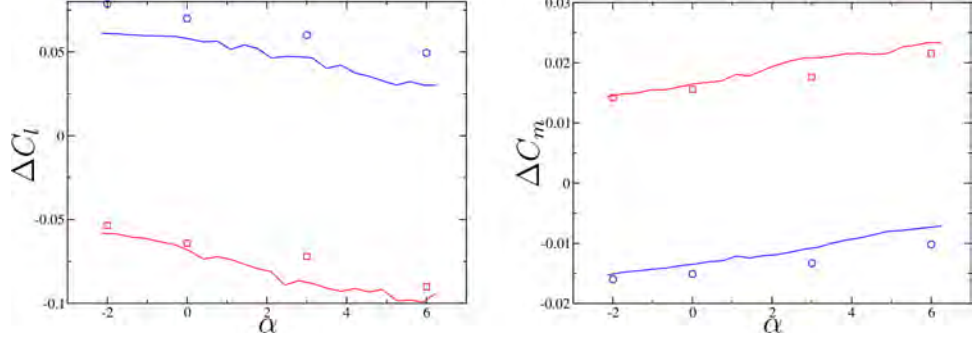


Figure V-1 Change in lift and moment coefficients due to pressure side actuation (red) and suction side actuation (blue) as a function of angle of attack. Symbols are from experiments in the Georgia Tech wind tunnel (section III).

fluid dynamic time scales (e.g., the shedding frequency). To reduce the associated computational burden, an averaged model (the Reynolds stress synthetic jet, or RSSJ, model) was developed (Lopez, 2009), which represents the affects of the actuator on the flow through the Reynolds stresses and momentum fluxes the actuator induces. The RSSJ model is motivated by the very large disparity between the actuator time scale and the maneuvering time scale, which makes simulation of controlled maneuvers very expensive. Use of the RSSJ model allows a time step five times as large to be used. This will be invaluable for simulation of extensive maneuvers, but the control scenarios simulated so far were not so long as to be prohibitive using the detailed SJ model, so the RSSJ model was not used in the results presented here.

iii. Support for a moving airfoil. To simulate the experiments performed in the Georgia Tech facility, it was necessary to represent the airfoil as it executes pitch and plunge maneuvers. This was accomplished using a grid that moved rigidly with the airfoil. Thus, we added to CDP a capability to perform simulations in a noninertial reference frame. The formulation solves for the velocities expressed in a specified “laboratory” inertial reference frame. The finite-volume formulation in CDP was modified so that the flux of mass and momentum through the faces of the finite volume was driven by the fluid velocity relative to the current grid velocity (Jee, 2010), which was determined from the translational and angular velocities of the domain. The resulting scheme preserved the second order energy-conserving properties of the CDP discretization.

iv. Model for the flow controller and airfoil dynamics. To simulate closed-loop flow control of the airfoil, we needed to integrate the CFD model with a model of the flow controller and a model of the inertial dynamics of the airfoil. The flow controller developed here (§II), was written in Matlab Simulink, and to integrate it with the CFD code, a Fortran or C implementation was needed. It was generated using the Matlab Real-Time workshop, which generates a C implementation of the controller expressed by Simulink. This was then coupled to CDP. In this way, as the controller was developed and refined by the controls group, it could be easily updated in the CFD model. Similarly, solution of the ODEs describing the two-degree-of-freedom dynamics of the airfoil were implemented in C and coupled with the controller and CDP. At each time step, the CFD solution was used to compute the lift and moment on the airfoil. The current vertical position and velocity, and the angular position and velocity of the airfoil is then used by the controller to determine the SJ actuator forcing. The lift and moment are fed to the airfoil dynamics model to update the positions and velocities, and finally the positions and velocities, and the SJ forcing are fed to the CFD solver for the next time step. The modified CDP code described above was used to perform a wide range of simulations representing various flow and control scenarios. These were selected to represent the experiments in the Georgia Tech wind tunnel and to model flight scenarios. In the former case, the mass and moment of inertia of the airfoil were given the values measured for the wind tunnel model (§III), and for the flight situation, much lower values representative of a UAV were used.

CFD simulations were performed to validate the models, to provide detailed data for reduced-order modeling (section IV), to investigate geometric sensitivities, to explore different control scenarios and to investigate the character of the controlled flow. Several key results from these simulations are presented below.

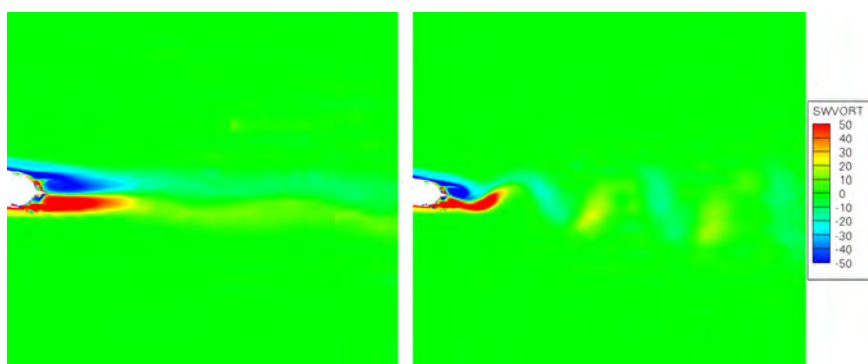


Figure V-2 Instantaneous spanwise vorticity distribution in the wake of the modified NACA 4415 at 3°. angle of attack with pressure side actuation. Left image is for a sharp trailing edge, the right is for a rounded trailing edge.

V.1 Geometric Sensitivities

One of the challenges of performing CFD simulations of the modified NACA 4415 airfoil with SJ actuators for comparison with experimental observations is ensuring that the geometry in the simulation is consistent with that in the wind tunnel (§III). It was found that flows over the modified airfoil configuration were particularly sensitive to small geometric variations. Indeed, the “as built” variations from the design geometry arising from the assembly of the modified airfoil were found to be sufficient to introduce important changes in the flow characteristics. This is not surprising since the trailing edge actuator configuration of the modified airfoils is designed to produce flow separation, in order to increase the sensitivity to SJ actuation. The consequence was that careful measurement of the as-built configuration was required to construct the models. In addition, some of the observed geometric sensitivities are interesting because they suggest ways in which the system geometry might be modified to improve performance. Among the geometric sensitivities observed are sensitivity to a) details of the upstream fairing between the airfoil and the actuator ramp (Jee, 2010), b) the angle of the corner at the downstream end of the actuator ramp, and c) rounding of the airfoil trailing edge (Lopez, 2009).

As an example, the geometric model that we initially used had a mathematically sharp trailing edge. Simulation results for this case showed that PS actuation resulted in strong stabilization of the wake, and virtually eliminated the vortex street that would otherwise be present

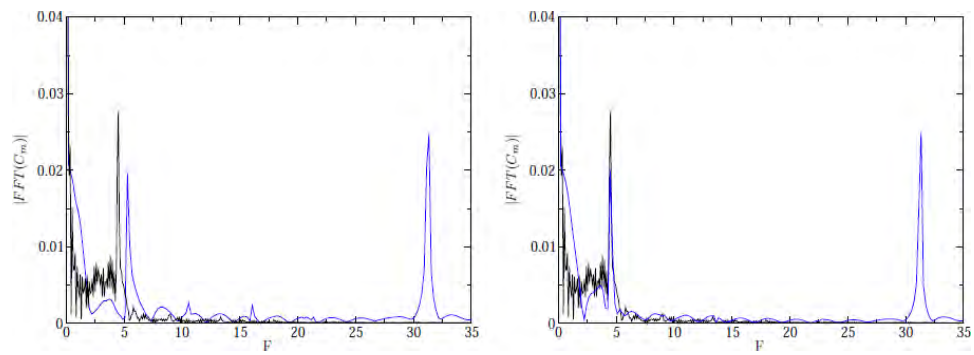


Figure V-3 Temporal spectrum of the moment coefficient of the modified NACA 4415 airfoil with no actuation (black) and with suction side actuation (blue). The image on the left is for a sharp trailing edge, on the right is for a rounded trailing edge.

(Figure V-2). Suction-side actuation, on the other hand, produced a change in the vortex shedding frequency (Figure V-3). Neither of these effects was corroborated experimentally. By introducing a slightly rounded trailing edge (radius of 0.1% chord), which is consistent with the geometry of the wind tunnel model, both of these anomalous effects were eliminated (Figures V-2 and V-3).

V.2 Simulations of Synthetic Jet Actuators

The action of the trailing-edge actuator relies on the sensitivity of a separated flow to excitation, in this case by the SJ. The intent is that the momentum added by the actuator will deflect the separated flow toward the airfoil, affecting a change in both the lift and the moment. As is shown in the streamlines of Figure V-4, this is precisely what happens. When the actuator is active, the mean streamlines are deflected. Note, however, that the mean flow near the actuator is actually quite complicated. Somewhat counter-intuitively, the average flows near the Coanda surface when the actuator is active is *toward* the actuator, whereas without actuation it is *away* from the actuator. The reason is that the in-stroke of the jet draws fluid from all around it, while the out-stroke flow is more unidirectional, forming the jet. Fluid is thus, on average, drawn from close to the surface. It is also clear in these figures that the flow in the jet outlet slot is quite complicated

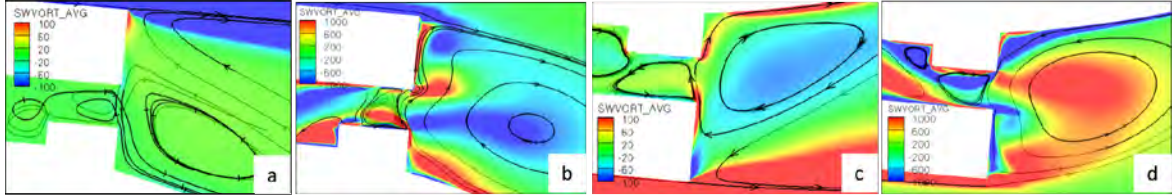


Figure V-4 Mean streamlines and spanwise vorticity near the synthetic jet actuator outlets for the suction side (a,b) and pressure side actuators (c,d) when the actuator is off (a,c) and on (b,d). Airfoil is at $\alpha = 3^\circ$.

(even in the mean). The rms velocity profiles at the outlet of the jet are quite asymmetric, and it is clear that there is significant interaction between the external flow and the flow inside the actuator. For this reason it was necessary to include the jet cavity as part of the simulation.

Because the actuator flows are sensitive to the environment in which they operate, and the operating environment of interest is a rapidly maneuvering airfoil, the effectiveness of the actuators during driven rapid maneuvers was simulated. The airfoil is made to undergo sinusoidal pitching from 0° to 6° angle of attack, with reduced frequency $k = \pi/2$, which has an oscillation period of $2T_{\text{conv}}$. Simulations were performed without actuation and with PS and SS actuation of the trailing-edge actuators. The evolution of the lift and moment coefficients as a function of angle of attack for one cycle are shown in Figure V-5. Note first that, as expected, the lift and moment are different during the pitch-up and pitch-down parts of the cycle, with lift higher during the pitch-up part of the cycle, and moment augmented in the direction opposite the pitching velocity. Also, there is an oscillation both in the lift and moment evolution caused by vortex shedding from the actuators. This oscillation is not present for a unmodified airfoil, nor is it present when using the modified actuator configuration discussed in section V.5. When the actuators are activated, the lift and moment curves are shifted, qualitatively and quantitatively consistent with the change in lift and moment caused by the actuators under static conditions (Figure V-1). Also present is a rapid oscillation in lift and moment at the SJ operating frequency. The effectiveness of the actuators is thus not significantly affected by airfoil maneuver.

V.3 Flow Control Simulations

To confirm that the simulated airfoil and control system is an accurate model of the wind tunnel configuration, several simulations of flow control experiments were performed. Here we consider a pitch-up maneuver to change the angle of attack from 3° to 6° . The simulation begins with the airfoil approximately steady at 3° , with a trim torque applied to balance the aerodynamic moment. The vertical position of the airfoil is fixed. At time zero, the controller is given a step

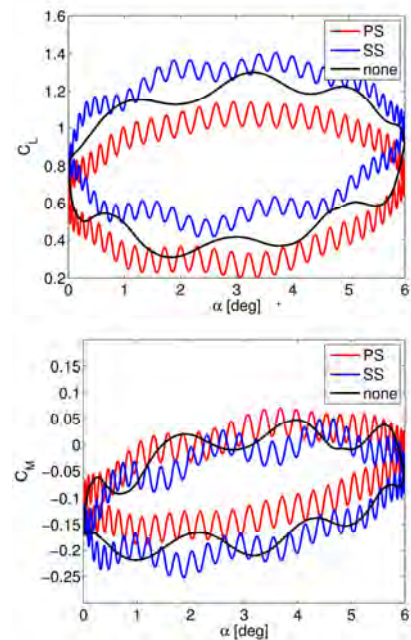


Figure V-5 Variation of aerodynamic lift and moment coefficients with angle of attack during sinusoidal pitch oscillations with reduced frequency of $\pi/2$.

command to increase the angle of attack. As shown in Figure V-6, the *PS* actuator then turns fully on for an extended period (approximately 10 convective time units) to produce the angular acceleration required to change the angle (recall that the moment of inertia is quite high). The airfoil pitches up over about $20 T_{\text{conv}}$, and overshoots. The *SS* actuator is then turned on to slow the pitch-up motion, and eventually the system comes to an equilibrium in which the *PS* actuator is active to balance the

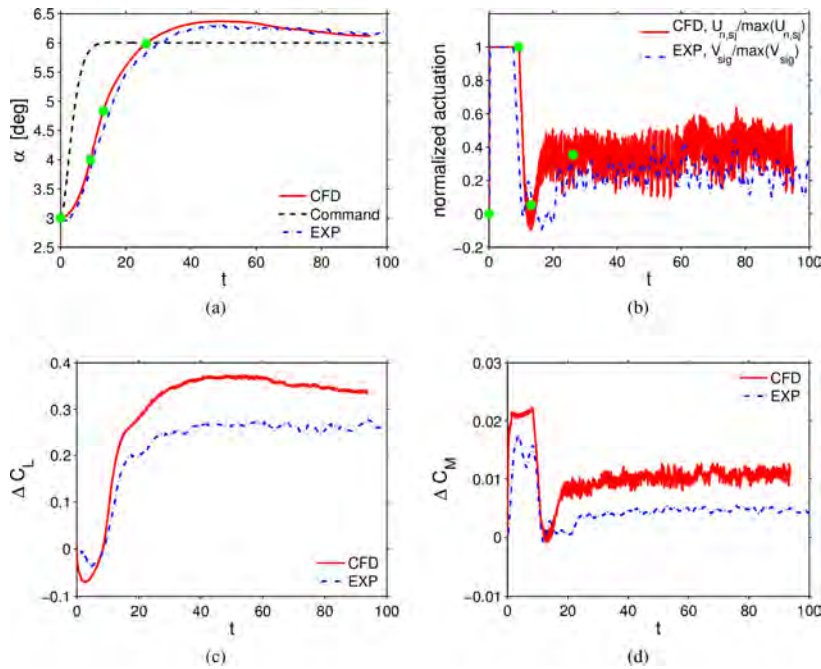


Figure V-6: System response for 1-DOF pitch control with SJ actuators. Shown are the evolution of (a) the angle of attack, (b) the strength of SJ actuation, with pressure side actuation positive, (c,d) increment in lift and moment coefficients due to actuation.

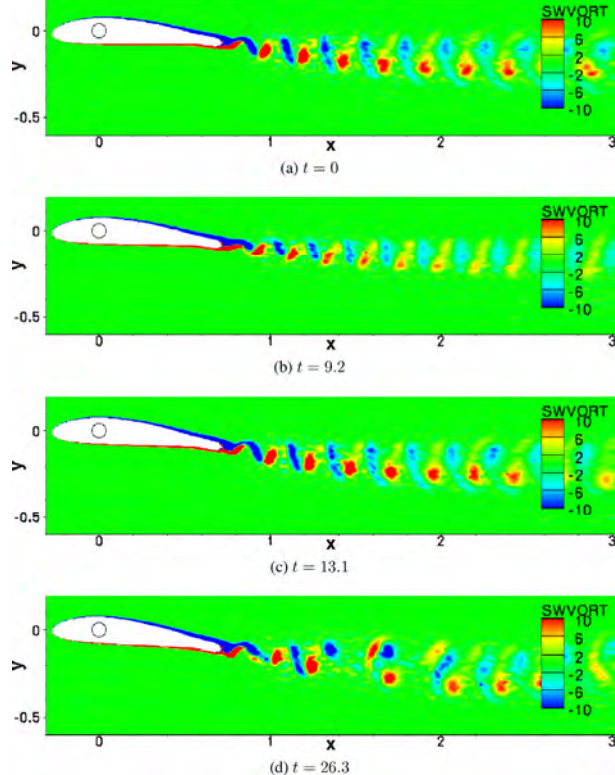


Figure V-7 Spanwise vorticity distribution in the wake of the airfoil undergoing the maneuver.

aerodynamic forces on the airfoil. This system response is qualitatively and, in the case of the angle evolution, quantitatively consistent with the wind tunnel measurements. The quantitative differences in lift and moment variation are attributed to the inherent differences between the simulations and the experiments, particularly, the wind tunnel walls and the slot in the side wall to accommodate the traverse mechanism.

Both the airfoil motion and SJ actuation change the flow field, as shown in Figure V-7, where four sample times are selected from the times indicated by green dots in Figure V-6(a) and (b). The full pressure-side actuation constrains the spread of the wake compared to the initial state (Figure V-7(a) and (b)). As the pitch rate increases and the actuation decreases, the wake spreads more (Figure V-7(c)). The shed vortices close to $\alpha = 6^\circ$ make the widest wake during the maneuver (Figure V-7(d)).

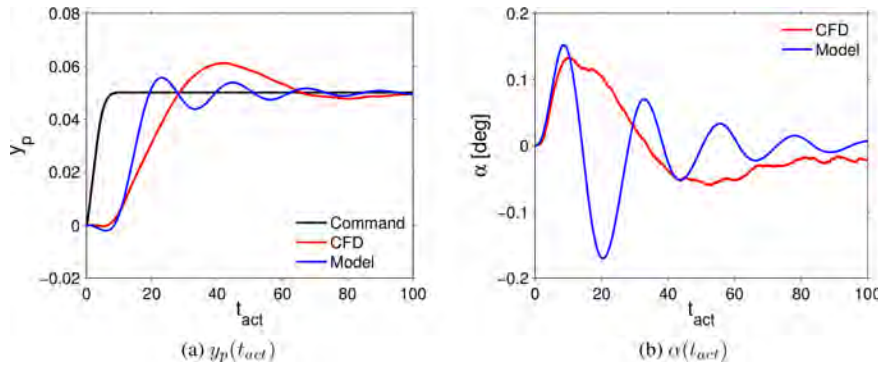


Figure V-8 Evolution of vertical location (left) and angle of attack (right) of the light airfoil with mass and moment of inertia similar to the Dragon Eye UAV undergoing a change in altitude maneuver, with commanded location shown in black (left), and the actual position and angle of the airfoil in red. The blue curve is the response of a linearized reduced model that is used in the adaptive controller.

58% (respectively) of those in the wind tunnel. These values being scaled from the inertial parameters of the Dragon Eye UAV. In this case, at $t = 0$, the controller is given a command to change vertical position slightly by $0.05c$. The response is shown in Figure V-8. The time scale of the response is about 80 convective time units, which is not significantly smaller than the 100 convective times observed for the wind-tunnel airfoil (Figure V-6). The primary reason is that the moments of inertia are similar, though the mass is much less. Notice that in executing this maneuver, the angle of attack changes by only approximately a tenth of a degree, which is all that is needed to quickly move this low-mass airfoil in the vertical direction.

While the airfoil executes an orderly maneuver, the controller response is rapidly oscillating at approximately the shedding frequency (Figure V-9). Similar oscillations were present in the one degree of freedom pitch control with a heavy airfoil representing the wind tunnel model (see Figure V-6), though the amplitude was smaller. Apparently, with this light airfoil, the controller is responding to the oscillation in altitude that occurs due to the lift oscillations caused by vortex shedding. While the controller performs admirably in executing this maneuver, its sensitivity to variations caused by vortex shedding is a disadvantage, and presumably degrades both the energy efficiency and response time of the control. Reducing the sensitivity of the controller to vortex shedding would be useful, and adaptive control based on the discrete-vortex ROM discussed in §IV.1 might be helpful in this regard.

One powerful capability the CFD simulation provides is the ability to explore scenarios not accessible in the wind tunnel. One example is an airfoil whose mass and moment of inertia are consistent with those of a UAV (properly scaled for wing span), rather than the heavier wind tunnel model. Simulations were thus performed with mass and moment of inertia approximately 2% and

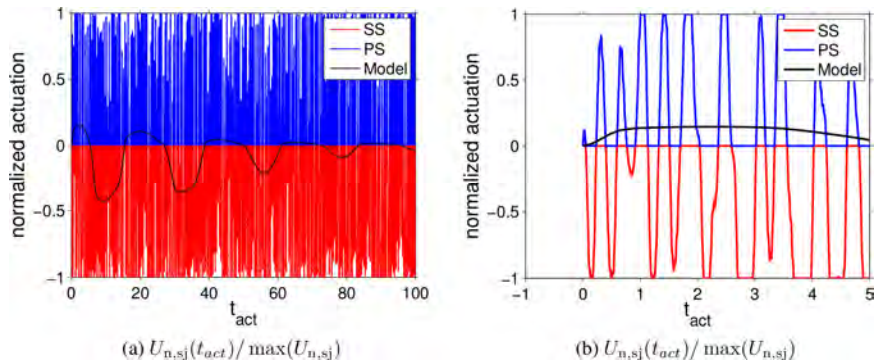


Figure V-9: Evolution of the actuation strength over the entire maneuver (left) and over the first 5 time units (right), for the light airfoil with mass and moment of inertia similar to the Dragon Eye UAV, undergoing a change in altitude maneuver. Pressure and suction side actuation are shown in blue and red respectively.

To investigate the ability of the actuators and control system to execute a rapid maneuver, the moment of inertial of the system was arbitrarily reduced to 1% of that of the wind tunnel model or about 2% of that for the model of UAV dynamics. The system was commanded to execute the same

change-in-altitude maneuver described above, and is evident in Figure V-10, the response is now much more rapid, with the maneuver completed in less than $10 T_{\text{conv}}$, compared to $80 T_{\text{conv}}$ in the previous case (Figure V-8). Again, the control system effectively executes the maneuver, with significantly less overshoot than in the previous case. The lower moment of inertia allows the actuators to pitch the airfoil up to as high as 0.8° angle of attack, and the angle of attack fluctuates significantly due to moment variations caused by vortex shedding. The controller response (not shown) is similar to that shown in Figure V-9, oscillating at the shedding frequency between full actuation for the PS and SS actuators.

V.4 Effects of Actuator Configuration

A new trailing-edge actuator

configuration was introduced, which required that the actuator model be recalibrated and revalidated for the new configuration. Simulations showed

that the dynamics of the trailing-edge flow and its interaction with the actuators are significantly different from before. In the old configuration, where the actuators on both sides were very close to the trailing edge, the unactuated trailing-edge flow had many of the characteristics of the near wake of a cylinder. The dominant dynamics in this configuration was oscillating vortex shedding, leading to a Kármán street. With the suction-side actuator moved significantly back from the trailing edge, the dominant dynamics becomes that of two independent turbulent shear layers that form as the flow separates from the actuators, as shown in Figure V-11a. When, for example, the suction-side actuator is active, it interacts with the turbulent shear layer. It appears from Figure V-11b that the effect is to increase the turbulent mixing across the layer, causing rapid closure of the separation bubble behind the actuator. The Coanda effect characteristic of actuation in the old configuration is not as obviously in play.

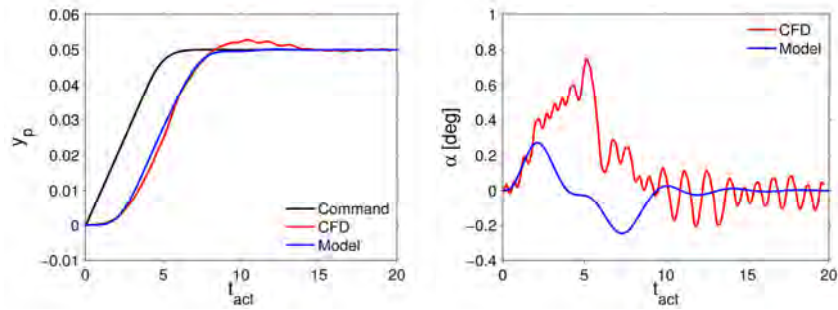


Figure V-10 Evolution of vertical location (left) and angle of attack (right) of the light airfoil, with mass and moment of inertia of 2% and 1% of the wind tunnel model respectively, undergoing a change in altitude maneuver, with commanded location shown in black (left), and the actual position and angle of the airfoil in red. The blue curve is the response of a linearized reduced model that is used in the adaptive controller.

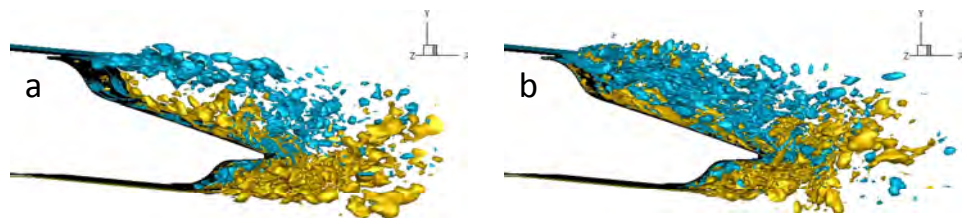


Figure V-11 Spanwise vorticity near the trailing edge of the new actuator configuration, with (a) no actuation and (b) PS actuation.

V.5 Separation Control

In addition to lift and moment control using trailing-edge actuators, stall control using suction-side pulsed actuators near the separation point is of great interest. To simulate this scenario, it was first necessary to validate the models for a stalled airfoil, and this was done with a NACA 4415 at an angle of attack of 20° . Modeling the smooth-wall separation from the suction side of a stalled airfoil is more challenging than separation from the trailing-edge actuators discussed above.

While the DDES turbulence model employed here is designed to represent massively-separated flows such as this stalled airfoil, it is also well known that its separation predictions are grid-dependent, producing such anomalies as grid-induced separation. This occurs because of the explicit appearance of the grid size in the model formulation, particularly in governing the switch between RANS-like behavior and LES-like behavior. For these reasons, to correctly represent the stalled flow, it was necessary to tune the grid to provide the correct length-scale cues to the DDES model. This was done by running a series of simulations with different streamwise resolutions on the suction side of the airfoil. If the grid was too fine, the DDES model switched into LES mode throughout the boundary layer, producing poor results since the simulation was not designed for this. If the grid was too coarse, the model was too dissipative, delaying separation. It was found that the finest grid that did not turn off RANS modeling in the boundary layer produced good agreement with experimental measurements of lift, drag and separation point. This need to tune the grid for the turbulence model is a shortcoming of the current DDES formulation, which is particularly troublesome in these flow control simulations because the actuators place their own, possible contradictory, demands on resolution. These challenges have led us to propose a new approach, in which the length-scale to be used in the DDES turbulence model is specified as a scalar field, unrelated to the grid. This proposal will be pursued as part of a follow-on project.

The spanwise vorticity for this case is shown in Figure V-12a. For stall control, pulsed-jet actuation as employed by Brzozowski et al. (2010) is considered. A short pulse of duration $0.05T_{\text{CONV}}$ and total momentum consistent with the experiments is applied at a point $0.15c$ downstream of the leading edge, and the evolution of the flow is tracked in time. As in the experiments, the separation region over the airfoil collapses during the next T_{CONV} , as shown in Figure V-12b, with an accompanying increase in lift. Then the flow slowly recovers, until approximately $9T_{\text{CONV}}$, when the airfoil is fully stalled again (not shown). The consistency of the simulation results with the experimental observations suggests that the momentum impulse and duration of the pulse are sufficient controlling parameters for the actuator, since other characteristics of the experimental actuator configuration, such as the cavity geometry and the compressibility of the actuator flow, were not represented in the simulations.

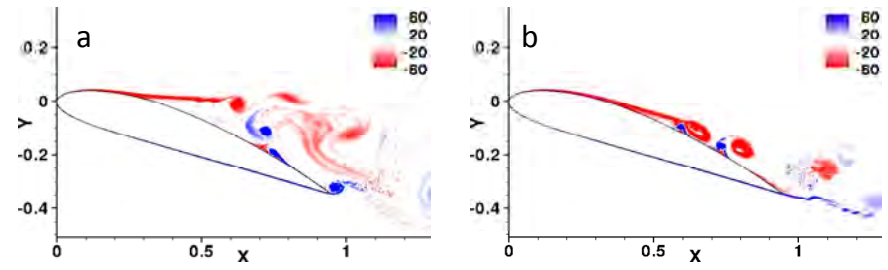


Figure V-12 Spanwise vorticity on a NASA 4415 at 20° angle of attack (a) before actuator pulse and (b) $4c/U$ after pulsed actuation.

The simulation results were used to investigate the dynamics of the actuation and the process by which the separation region collapses. As shown in Figure V-13a, the actuator jet produces a pair of counter-rotating vortices that disrupt the

boundary layer as they move downstream of the actuator. As they approach the separation point, they begin to disrupt the separation shear layer, ultimately causing the vortical region to detach from the surface and begin to roll up (Figure V-13b). The combined effect of the vortex injected by the actuator and the disruption of the separation shear layer is to modify the local pressure environment, accelerating the flow in the (former) separation region, allowing the boundary layer to be re-established there. The dynamics of the interaction outlined above are quite complex, and require further analysis to quantitatively characterize the phenomenon to enable design of even more effective actuators and actuation strategies. This is the topic of continuing research.

V.6 Summary

The combination of an incompressible CFD solver (CDP), the delayed detached eddy simulation turbulence model and a geometric and operational model of the SJ actuators was successful in representing the experimentally observed aerodynamic response to the actuators in the wind tunnel (§III). However, the models displayed a strong sensitivity to geometric details, suggesting both the opportunity to tune performance through minor geometric adjustments, and the requirement to precisely define the geometry, especially for making accurate predictions. This sensitivity should not be surprising, since it is precisely because a separated flow is sensitive to small changes that small SJ actuators can have significant affects. When the computational model is coupled to models of the controller (§II) and wind tunnel traverse, it represents well the response of the controlled airfoil. This allows us to predict the response of the system for dynamic conditions representative of free flight (lower mass and moment of inertia than the wind tunnel model and traverse), from which we found that the controller was responding to small fluctuations caused by vortex shedding from the trailing-edge actuators. Finally, the simulation results provided important insights into the character of the actuated flow and data to support reduced-order modeling (§IV).

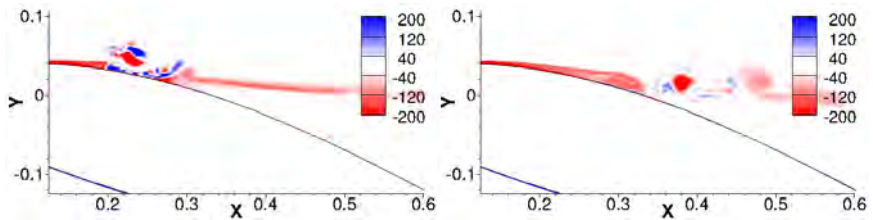


Figure V-13 Spanwise vorticity in the region of the pulsed actuation at (a) $t = 0.1T_{CONV}$, and (b) $t = 0.25T_{CONV}$ following the pulsed actuation.

VI. Large-Area, Polymeric flow Sensors

Here, we discuss design, fabrication, and integration of large-area, flexible arrays of polymeric flow sensors using integrated, multiplexing interconnects for individual sensor addressing. These cilia-based sensors are used to detect the direction, and measure the magnitude, of the velocity on aerodynamic surfaces. An important aspect of the development process was selection of processes for mass-manufacturing by borrowing from MEMS-based technologies.

VI.1 Development of Flow Sensors

Fabrication of a Cilia-Based Sensor using Metal Transfer Molding

Cilia based flow sensors have been demonstrated previously (Chen et al., 2006, Krijnen et al., 2005). The main goals of the present research were to a) improve the cilia manufacturing process to enable large area arrays; and b) develop a simultaneous packaging process for the arrays, allowing them to be used in realistic flows.

Our approach to more easily manufacturable cilia is based on the technique of *metal-transfer molding (MTM)*. Briefly, the MTM process combines the large-area, high-throughput, and low-cost nature of micromolding of structures with an in-situ metal transfer step during the micromolding, by which the simultaneous fabrication of high aspect ratio cilia structures with electrical strain sensors implemented. The 3D-MTM process also inherently allows freedom of material selections for highly compliant cilia, improving sensitivity.

Figure VI-1 shows the cilia fabrication sequence. First an SU-8 epoxy master is fabricated. Then a layer of polydimethyl-siloxane (PDMS) is poured over the mold master and cured to form the daughter mold (Steps 1 and 2). The daughter PDMS mold is then treated in fluorine plasma and fresh PDMS is poured into it, to obtain a reusable PDMS mold master (Step 4). Polymethylmethacrylate (PMMA) is then poured over the PDMS mold master to obtain a PMMA “*sacrificial daughter mold*” (Step 5). Then a 1:20 PDMS-hexane mixture is spray coated onto the PMMA mold in order to provide a protective layer for the slender metal lines. Titanium and Gold are sputtered onto the mold and patterned by micro-transfer printing by bringing a high surface energy plate in contact with the mold to remove gold from the protruding areas (Step 6). Finally, the PMMA mold is filled with PDMS and dissolved in a solvent (N-methyl pyrrolidinone or ethyl lactate) after curing the PDMS (Step 7). Figure VI-2 shows a photomicrograph of the reusable SU-8 mold masters and the final fabricated devices.

Several devices were tested in a benchtop wind tunnel over a range of speeds (up to 10 m/sec, Figure VI-3). The cilia were interconnected with resistance measurement equipment for real-

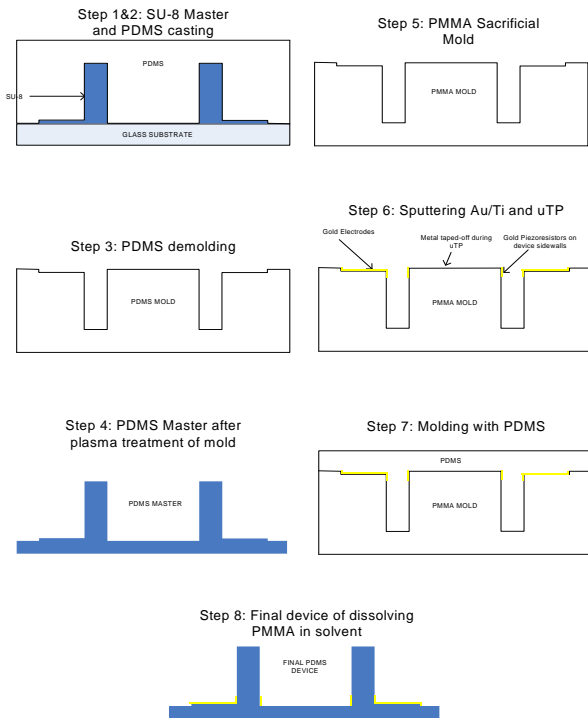


Figure VI-1 Fabrication sequence

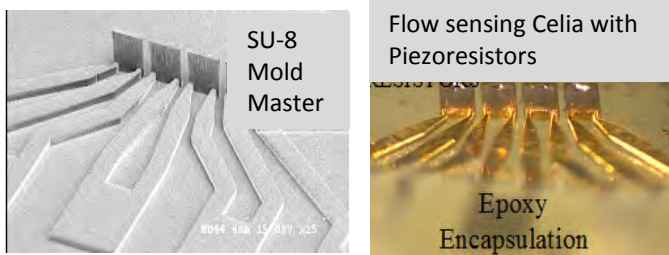


Figure VI-2 Fabricated devices showing SU-8 masters and final cilia sensors

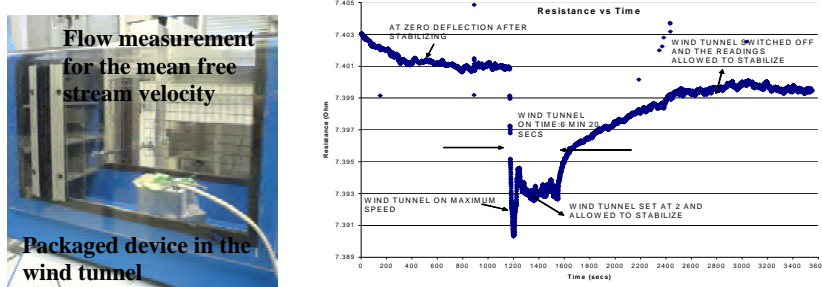


Figure VI-3 Left: benchtop wind tunnel and packaging of cilia in wind tunnel; Right: Cilia output as a function of wind tunnel speed.

time monitoring and placed in the center of the wind tunnel. Since gold has a positive piezoresistive coefficient, the resistance decreases when the sensing element is in compression. Figure VI-3 shows a typical time trace of a cilia output when the current is 4 mA. When the sensor detects air speed, the resistance drops sharply, and following a brief transient settles to a level corresponding to the air speed in the tunnel. Once the wind tunnel is switched off, the sensor responds by showing an increase in resistance, due to the reduction in compressive stress.

Wireless Pressure Sensor

With an eye to wireless readout of the cilia, we developed a second approach involving the use of evanescent resonant cavities (Figure VI-4). In this approach, small cavities with resonances in the GHz range are deformed by flow or pressure, thereby changing the resonant frequency. Knowledge of the force-deformation characteristics of a resonant cavity allows the transduction of flow forces to readout frequency. Such resonators are compatible with polymer metal-transfer micromolding, since due to the skin effect in the GHz range the transferred metal can be used on top of the micromolded component with negligible loss of performance compared to a solid metal cavity (at sensing power levels). Increases in operating frequencies enabled by high-frequency circuitry have reduced required RF radiator sizes, while concomitant advances in fabrication technology have increased achievable thicknesses, such that surface micromachined radiators in the 10-100 GHz range are now feasible using metal transfer micromolding.

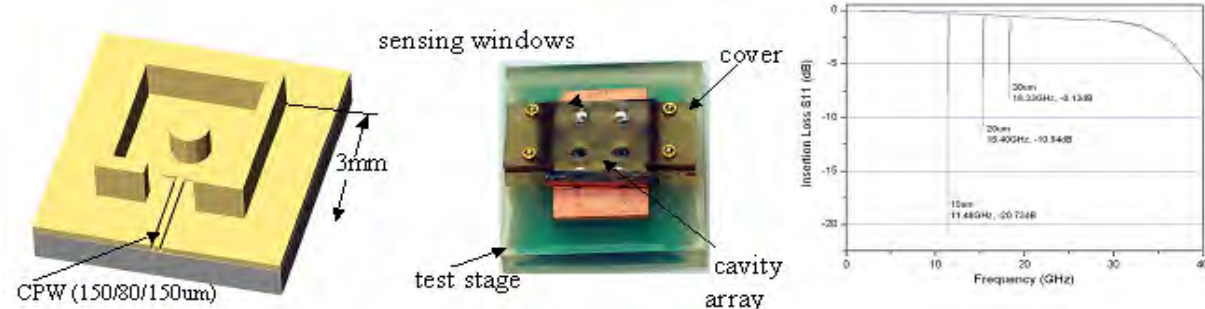


Figure VI-4 Metal-transfer-micromolded pressure sensor based on GHz evanescent cavity sensing. Left: device concept (with upper membrane removed); center: initial prototype device; right: multiple resonances at differing membrane deflection.

An All-Polymer Air Flow Sensor Array

To address several performance and reliability issues with the MTM-based cilia, an all polymer approach to cilia arrays was investigated. The fabrication process shown in Figure VI-4 (left) results in simultaneous fabrication of multiple array elements using a large-area etching process, as well as a reduction of process complexity through elimination of several previous processing steps. A 7.6 μm -thick Kapton® (Dupont) film is patterned using Reactive Ion Etching (RIE) to form an in-plane cantilever [Figure VI-4, left (a)]. A carbon-black-based conductive composite elastomer that displays high piezoresistivity is then coated over the cantilever surface using an inking process through an aligned stencil. Removal of the stencil results in an all-polymer microcilia array [Figure VI-4 left (b)]. Copper electrodes are then e-beam evaporated using a shadow mask [Figure VI-4 left (c)]. Finally, the out-of-plane cantilever is realized using plasma-enhanced chemical vapor deposition (PECVD) of silicon dioxide film deposited on the electrode areas of the device layer (Figure VI-4 left (d)). Figure VI-4 (center) shows a fabricated sensor array mounted on a curved surface as well as an array on Flex-PCB with multiplexer IC addressing components integrated. On the right side of Figure VI-4, we show the sensor structure, comprising out-of-plane Kapton microcilia coated with a carbon-black-loaded polydimethylsiloxane (PDMS) elastomeric piezoresistor.

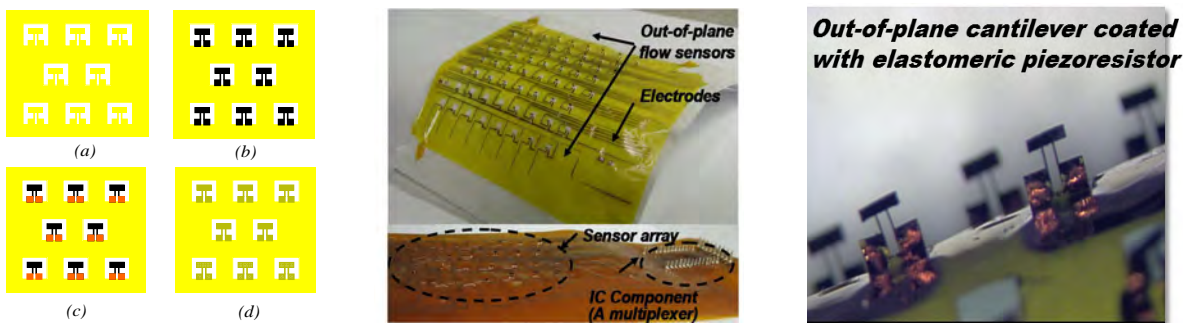


Figure VI-4 An all-polymer air flow sensor array. Left: fabrication sequence; center: fabricated all-polymer air flow sensor array; right: out-of-plane sensor structure.

VI.2 Measurement Methods and Interfacing Circuitry

In addition to development of sensor array fabrication technology, we also developed methods to overcome sensor drift. The new approach was to exploit the aeroelastic response of the sensor in the air stream, and to utilize measurements of its vibration amplitude. Figure VI-5 shows a comparison between a direct resistance measurement and the vibration amplitude measurement. In the resistance measurements, the flow sensor's cantilever is deformed by flow over it, which in turn induces a strain in the piezoresistor. The resistance changes as a function of the strain induced by the air flow. However, the benchtop tests have demonstrated that direct resistance measurement can be vulnerable to DC drift.

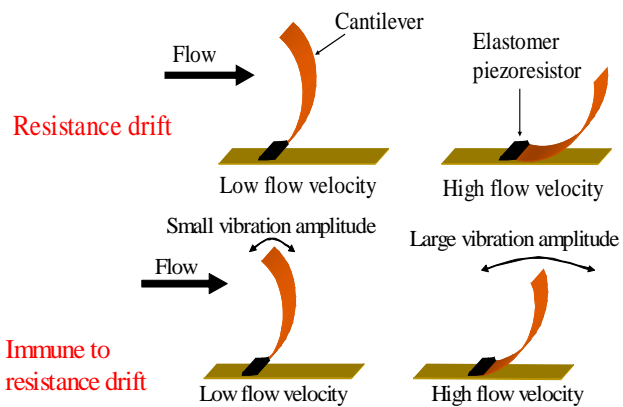


Figure VI-5 Top: Direct resistance measurement method; Bottom: Vibration amplitude measurement

While in the air flow, the sensor experiences not only a quasi-static deformation but also vibration due to aeroelastic ‘flutter.’ The amplitude of the flutter increases with the air speed, and so microcontroller-based circuitry was developed to extract the peak-to-peak vibration amplitude from the sensor output. Since the sensor output is now primarily dependent on the vibration-induced resistance change, the sensor output is relatively insensitive to DC resistance drift. Figure VI-6 shows measurements using the fabricated all-polymer air flow sensor for both direct resistance and vibration amplitude measurements, each acquired in two sets six hours apart. The direct resistance measurements exhibit baseline resistance drift, while the vibration measurements show virtually no drift.

Given these results, a novel drift reduction algorithm was applied to the flow sensor. This approach combines both DC and AC resistance changes in the flow sensor, together with the flow sensor’s calibration results, to compensate for baseline resistance drift. Microcontroller-based circuitry is used to extract both the AC and DC resistance changes from the sensor output. Figure VI-7 compares the new approach to the vibration amplitude measurements, and demonstrates significant improvement of the drift in sensor output. A block diagram of the sensor readout circuit is shown in Figure VI.3-4. The piezoresistor in the flow sensor is connected to a single-element-varying, voltage-driven Wheatstone bridge, which is composed of three non-variable resistors and the piezoresistive sensor as the varying element. The output of the bridge is fed to an instrumentation amplifier as a gain stage. When there is a resistance variation ΔR in the piezoresistor with an initial resistance of R , the output of the instrumentation amplifier is given by:

$$V_o = \frac{1}{2} \left(\frac{\Delta R}{2R_o + \Delta R} \right) V_s \approx \frac{1}{4} V_s \left(\frac{\Delta R}{R} \right) G$$

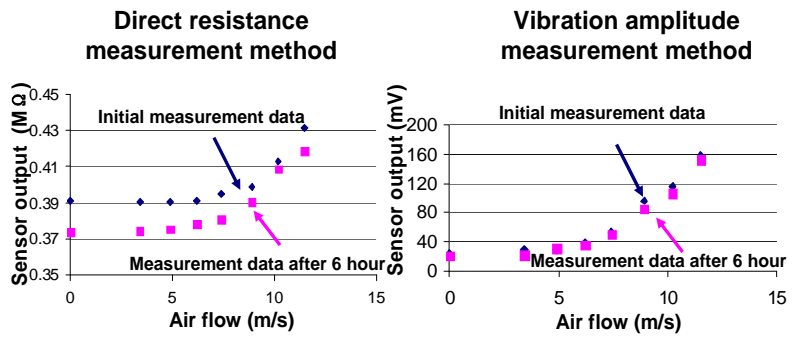


Figure VI-6 Left: Direct resistance measurements; Right: Vibration amplitude measurements (diamonds and square symbols represent data at the onset of the experiment and 6 hrs later).

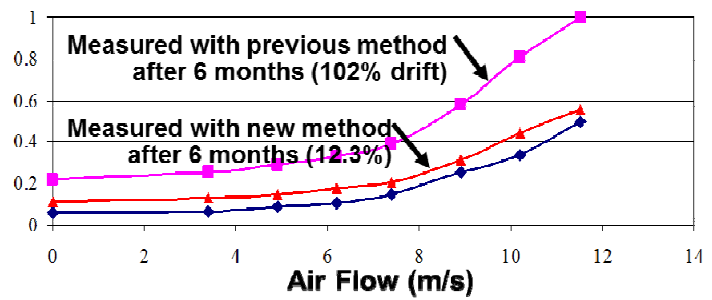


Figure VI-7 Experimental results of a drift- resistant algorithm.

compares the new approach to the vibration amplitude measurements, and demonstrates significant improvement of the drift in sensor output. A block diagram of the sensor readout circuit is shown in Figure VI.3-4. The piezoresistor in the flow sensor is connected to a single-element-varying, voltage-driven Wheatstone bridge, which is composed of three non-variable resistors and the piezoresistive

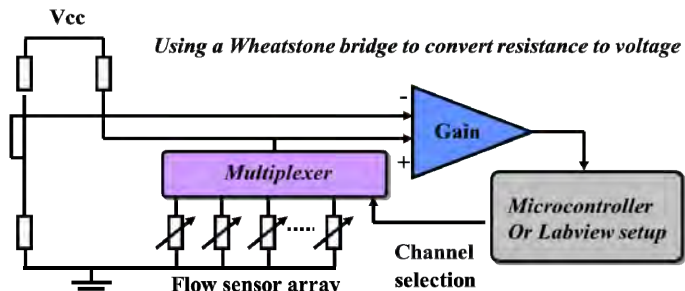


Figure VI-8 Schematic of the sensor array read-out circuitry.

where V_s is the supply voltage of the bridge and G is the gain of the amplifier. In order to convert the resistive output to a voltage output, a microcontroller is used for data acquisition and signal processing.

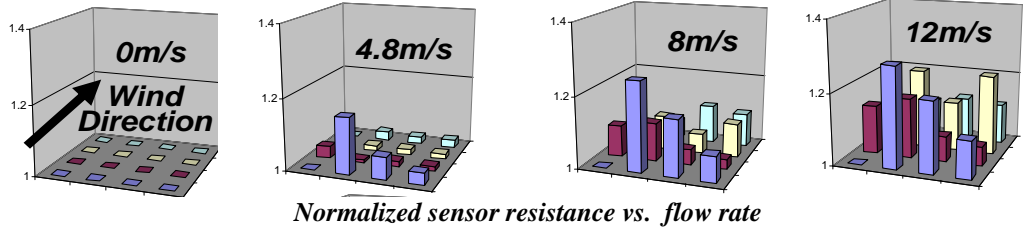


Figure VI-9 Flow mapping over a 40 x 40 mm patch using 16 sensors with array read-out circuitry

To demonstrate the array mapping functionality, a multiplexed 4 x 4 cilia sensor array with multiplexed read-out circuitry was placed on a flat plate in the benchtop wind tunnel. Figure VI.3-5 shows flow mapping over a 40 x 40 mm array. The results demonstrate the flow mapping capability of the array at different flow speeds.

Finally, the array was placed on the suction side of a CLARK-Y airfoil equipped with bleed flow control actuation that enables post-stall flow attachment. The airfoil was stalled at $\alpha = 18^\circ$ at $Re = 250,000$. The polymer sensors were placed downstream from separation (at mid-chord), and as shown in Figure VI-10, their output clearly reflected the changes in the local flow in the absence and presence of actuation.

VI.5 Summary

Several flow sensors were developed and fabricated including a cilia-based gold piezoresistive flow sensor, an RF resonator-based pressure sensor, and an all-polymer air flow sensor. The all-polymer sensor was selected for detailed investigation, owing to a) the inherent flexibility of the substrate material substrate that enables integration into curved surfaces, b) fabrication in parallel using planar micromachining process, c) low-cost, and d) scalability. Along with the development of an array of sensors having characteristic dimensions of 1 mm, a novel measurement technology was developed to mitigate the effects of drift and was implemented and tested successfully. Measurements in a small-scale wind tunnel demonstrated that the sensor arrays can be used for flow mapping on airfoil surfaces and can detect stall and flow reattachment.

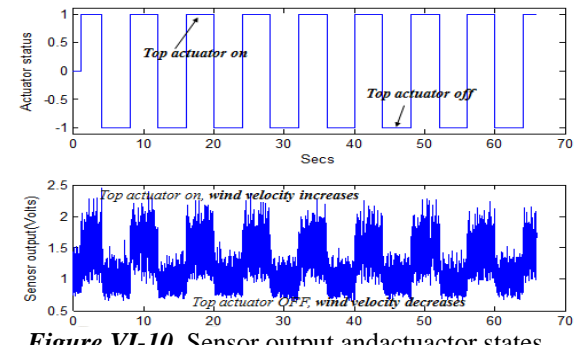


Figure VI-10 Sensor output and actuator states.

VII. Flight Tests

Flight and wind tunnel testing of a modified Dragon Eye UAV were conducted at the Georgia Tech Research Institute (GTRI) to investigate the effectiveness of flow control actuators for flight control. The goal was to demonstrate that flight control can be achieved by controlling the flow physics as described in Section III. The problem is motivated by the need to operate such vehicles in confined areas like urban environments where both rapid maneuvering and gust rejection are important for mission effectiveness. Closed loop flow control offers a unique opportunity to achieve both.

VII.1 The Flight Test Vehicle

The flight tests were conducted with a modified Dragon Eye UAV. Dragon Eye is a small battery-powered UAV developed originally by the Naval Research Laboratory for the U.S. Marine Corps. The aircraft weighs about 5 lbs and typically carries a small video camera as a payload. Figure VII.1 shows the GTRI Dragon Eye in its original standard configuration. Dragon Eye does not have a horizontal tail for stability and control. Instead, the wing has a reflexed trailing edge for pitch stability. The conventional wing trailing edge control surfaces (elevons) collectively provide pitch control and differentially provide roll control. The vertical stabilizer does not have a rudder. The battery pack is positioned in the nose to balance the aircraft for stability.



Figure VII.1 The Dragon Eye UAV

VII.2 Dragon Eye Modifications

Installing the prototype fluidic actuator system represented a significant weight growth for the Dragon Eye. The system consisted of electronic driver boards, power conditioning boards, and the actuator arrays. Figure VII.2 shows the primary components of the actuator array. Power was drawn from the aircraft flight battery. The actuator

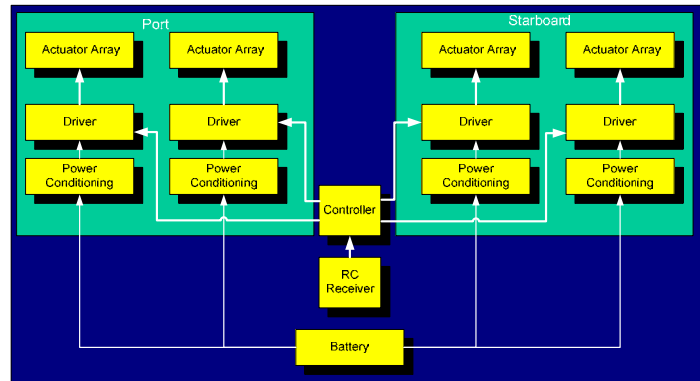


Figure VII.2 Actuator Block Diagram

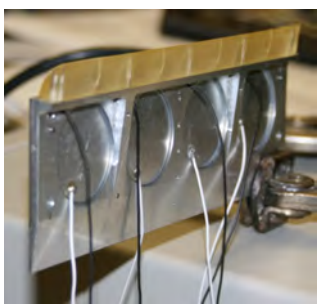


Figure VII.3 SJA array baseplate

array was built on an aluminum baseplate (Figure VII.3). To preserve the baseline performance of the Dragon Eye flight vehicle, wing tip extensions were added to the aircraft to maintain the baseline wing loading. The actuator arrays were located on the most outboard portion of the wing for maximum roll control. This increased the roll and yaw moments of inertia and diminished the lateral-directional stability of the aircraft. To compensate for this, the vertical

stabilizer was enlarged. Finally, because the actuators were located on the wing's trailing edge, they shifted the c.g. of the aircraft aft. This required some lengthening of the nose of the aircraft to allow the batteries to be moved farther forward to rebalance the aircraft. Figures VII.4a and b show the modified Dragon Eye, and a close up of the fluidic actuator installation on the wing tip. Some of the flights included fences on either side of the actuator banks in an effort to channel the flow over the actuators for greater effectiveness.



Figure VII.4 Modified Dragon Eye Test Bed Aircraft (left) and SJA Array Installed at Wing Tip (right)

VII.3 Fluidic Actuators

Owing to programmatic constraints, the hybrid actuators that were used in the flight tests were similar in overall geometry to the actuators that were used in the wind tunnel investigations (Section III.1), rather than developing new actuators that are more nearly optimal for the flight platform. The actuation during the flight tests differed in several respects from the wind tunnel tests. To begin with, the wind tunnel investigations considered primarily a 2-D configuration while in the flight tests the actuation was effected near the wingtips of the Dragon Eye (to enable use of the existing elevons) where three-dimensional effects are clearly more important. Furthermore, power and weight constraints for Dragon Eye platform dictated that the actuators be operated near the fundamental resonance frequency of the piezoelectric drivers (1030 Hz compared to 2050 Hz in the wind tunnel) while limiting the driving voltage to 45 VRMS (compared to 100 VRMS in the wind tunnel) to prevent damage to the disks. As a result, the flight test actuators produced jets having a maximum average peak velocity (about 30 m/sec) that was considerably lower than in the wind tunnel tests.

To generate a nose-up (or nose-down) pitch moment the actuators on the pressure (or suction) surface of the wing were activated. For a roll moment to the right (or left) the upper left (or right) and the lower right (or left) banks of actuators were activated. For proportional control, the driver signal was operated on a 300 msec duty cycle. The amount of time that the driver signal was active was proportional to the position of the pilot's stick on a standard RC controller. Small movements of the stick produced short "chirps" while a full deflection would produce a continuous driver signal. Figure VII.5 illustrates the control actuation scheme. At the flip of a switch, the pilot could toggle between control modes using either the conventional controls or the hybrid fluidic actuators in a mixed mode wherein conventional control of pitch was used when the hybrid actuators were active in controlling roll, or conventional control of roll was used when the hybrid actuators were controlling pitch. Takeoffs and landings were performed using the conventional control surfaces, and the fluidic actuators were used to execute specific flight maneuvers at altitude.

A Crossbow Technology MNAV100CA navigation board was installed along with a data recorder to record the aircraft's motion in flight. The MNAV100CA is a calibrated digital sensor and servo control system designed for use in radio control (R/C) vehicles. The onboard sensor package included accelerometers, angular rate sensors, and magnetometers as well as static pressure (altitude) and dynamic pressure (airspeed) sensors for use in airborne robotics. A GPS sensor was also included for both path planning and navigation.

VII.4 Flight Tests

The flight tests were conducted at the Townsend Bombing Range in southeast Georgia near Savannah. Nine test flights were conducted:

1. Lightweight checkout flight
2. Ballasted checkout flight
3. Fluidic actuator dummies with outboard ballast checkout flight
4. Aborted flight due to propeller/launch issue
5. Active actuator test flight – roll maneuver only
6. Fluidic actuator-controlled pitch maneuver attempted
7. Test actuator-control of roll maneuvers with minor propulsion tweaks for higher speed
8. Test actuator-control of maneuvers with 2-d fences installed
9. Demonstrate actuator-control of pitch and roll maneuvers

The aircraft configuration data for each of the flights is given in the table:

Flight #	Weight (g)	Weight (lbs)	Span (in)	XCG (in)	XCG (% chord)	YCG (in)	ZCG (in)	Ballast Weight (g)	Ballast Weight (g)	SJA Dummies	SJA Installed
1	2726	6.01	63	2.125	17.71	0	-0.375	0	0	X	X
2	3293	7.26	63	2.125	17.71	0	-0.375	567	1.25	X	X
3	3284	7.24	63	2.125	17.71	0	-0.375	558	1.23	✓	X
4	3248	7.16	63	2.125	17.71	0	-0.375	0	0	X	✓
5	3248	7.16	63	2.125	17.71	0	-0.375	0	0	X	✓
6	3248	7.16	63	2.125	17.71	0	-0.375	0	0	X	✓
7	3248	7.16	63	2.125	17.71	0	-0.375	0	0	X	✓
8	3284	7.24	63	2.125	17.71	0	-0.375	0	0	X	✓
9	3302	7.28	63	2.125	17.71	0	-0.375	0	0	X	✓

Several general observations are worth noting for context. First, as discussed in Section VII.3, the flight test actuators were not as powerful as those used in the wind tunnel investigations. As

a result, the flight control authority during the flight tests was fundamentally limited by weight and power budgets for the Dragon Eye aircraft. Furthermore, in order to accommodate the existing elevons, the fluidic actuators were mounted near the wing tips where their effectiveness was further limited by the “quality” (in terms of separation) and direction of the local flow. In essence, the control authority available was comparable to that available from the conventional actuators (elevons) at 2° - 3° of deflection. A more subtle limit also emerged from the tests. There were four individual synthetic jets in each of the four actuator modules used onboard the aircraft. Hence, lack of full function in any one of the synthetic jets could lead to some degree of asymmetry among the four actuators. Thus, for example, activation typically led to the production of a slight yawing moment, always in the same direction (depending on which wing contained the synthetic jet that was not performing fully). In addition, with the large vertical stabilizer, Dragon Eye has fairly strong roll-yaw coupling. Hence, the incidental yawing moment during roll activation typically led to a greater rolling moment in one direction than in the opposite direction. A slight misalignment of the vertical stabilizer could also produce a similar effect. Even though the modified Dragon Eye exhibited weak roll control authority, a complete figure-8 maneuver was successfully demonstrated using only fluidic actuation for roll control.

Figures VII.6-8 present flight data for Test Flight 9. Figure VII.6 shows a macroscopic portrait of altitude, airspeed and magnetic heading for the overall flight duration (about 400 sec). It also shows the intervals during which flight control was achieved with conventional or mixed mode controls. Note that when the conventional control surfaces are

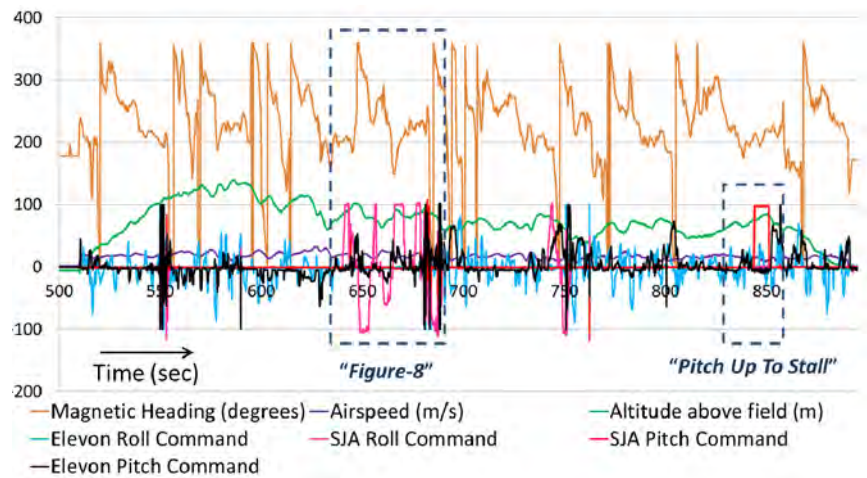


Figure VII.6 Flight data for Test Flight 9.

active, the fluidic actuators are inactive and vice versa. In addition to the pilot’s control inputs, the aircraft responses were also affected by gusts and throttle settings. For this reason and because the control authority of the fluidic actuators was rather limited, interpretation of the aircraft’s response is at times difficult. Nonetheless, comparison of the flight video with the recorded flight data allowed positive identification of the desired maneuvers. The regions where the aircraft executed first a ‘figure-8’ maneuver, and then subsequently a pitch up to a powered stall condition, are shown by the dashed rectangles in Figure VII.6.

Figures VII.7 and VII.8 show these maneuvers in more detail. In Figure VII.7, a 55 second portion of the flight record is shown. Synthetic jet operation in roll mode is shown by the red curve. At the reference time of 640 seconds, the aircraft is commanded by the fluidic actuators to bank left. A 10 second left turn ensues (augmented by a complementary pitch up command to the elevons), shown by the black curve. The aircraft is brought back to straight and level flight after more than 180° of turning. At a reference time of 660 seconds, a command to the fluidic actuators calls for initiation of a right turn for the second loop in the figure eight. The ensuing

right turn also lasts about 10 seconds with the aircraft turning through more than 180° before being brought back to level conditions, completing the figure-eight maneuver. A second figure-8 was initiated at 675 seconds. This time the aircraft banked more steeply to the left, approaching 90° at one point whereupon the pilot elected to switch control back to the conventional elevon mode at about 690 seconds.

Figure VII.8 illustrates the pitch up maneuver in detail. The altitude curve has been shifted downward by 40 m for easy viewing. Note that the vertical axis has been expanded relative to Figure VII.7, and the fluidic actuator command has arbitrarily been scaled down by a factor of 20 from Figures VII.6 and VII.7. The 20 second record is interpreted as follows. The aircraft clearly climbs a total of 20 m altitude in about 12 seconds. The climb is initiated by conventional elevon pitch up commands which are shown by the black curve in the lower part of the graph. The pitch angle response is shown by the brown curve, reaching greater than 20°

three times, followed each time by a brief stall lasting about a second. The airspeed is relatively constant during this time. At a reference time of 844 seconds, pitch control is switched to the fluidic actuators. The aircraft responds by retarding the pitch down rate that followed the third stall, and then restoring an increasing pitch angle that resulted in resumed climb. The fluidic actuators could bring the pitch attitude up to about 16° degrees, holding that attitude until the aircraft stalled oneThis control authority last time, followed by a rapid pitching down of the nose and a loss of altitude while the airspeed increased. Control was returned to the elevon system at a reference time of 852 seconds whereupon stall recovery followed.

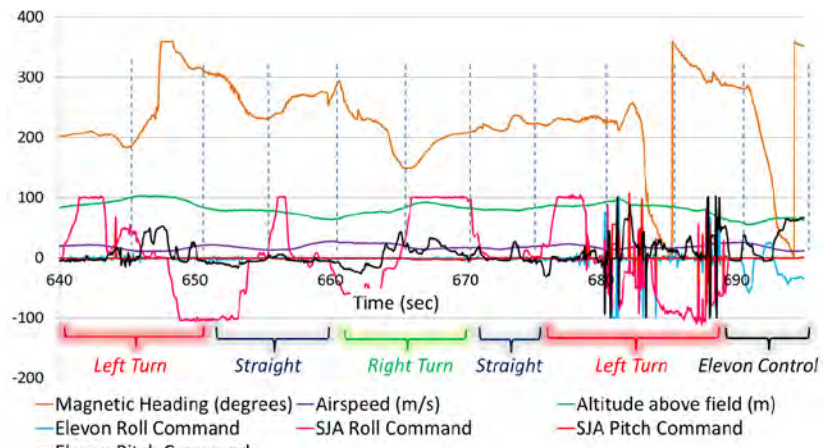


Figure VII.7 Longitudinal response to conventional control in figure-8

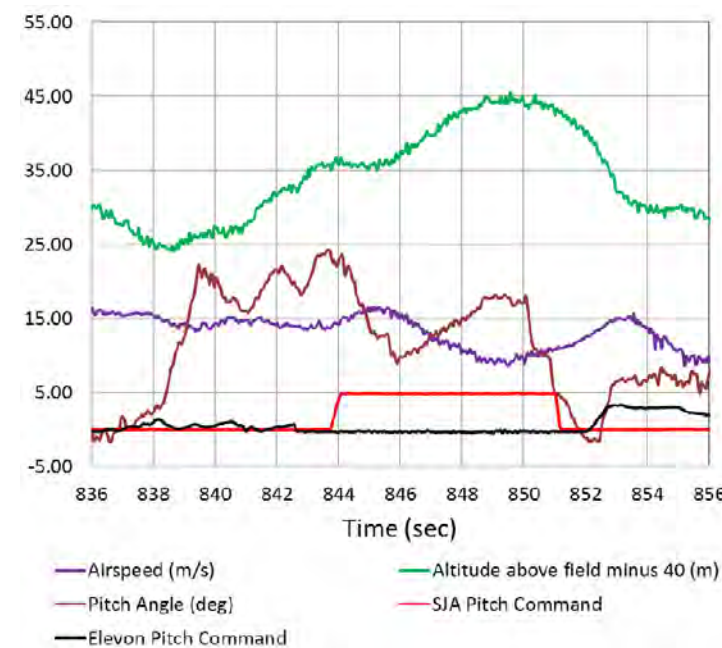


Figure VII.8 Longitudinal response to flow control actuation (pitch up to power stall)

VII.5 Wind Tunnel Testing of the Dragon Eye UAV

In order to further assess the performance of the flight model, wind tunnel tests of the full aircraft configuration were conducted following the flight tests. These tests were conducted with both powered and unpowered (without propellers installed) configurations. To accommodate the full aircraft, the wind tunnel was configured in an open jet mode as shown in Figure VII.9. The span of the tunnel's open section is 160 cm. For the angle of attack sweeps the nominal dynamic pressure was 2 lb/ft².

The operation of the fluidic actuators has a slight effect on the lift, as shown in Figure VII.10a, enhancing the maximum lift coefficient somewhat, but has a greater effect on drag coefficient (Figure VII.10b) which decreases for all modes of fluidic actuation. The changes in the pitching and rolling moment coefficients are shown in Figures VII.10c and d. Clearly, these coefficients are affected by fluidic actuation, providing a measure of control authority for pitch and roll control. The pitch control authority was comparable with that achieved with +1.3° or -1.8° of elevon deflections. Similarly, the roll control effectiveness using the fluidic oscillators was comparable to about 2.5°-3° of aileron deflection. Despite the limited authority of the actuators installed on the modified Dragon Eye, they were nonetheless sufficient to control the aircraft



Figure VII.9 Dragon Eye model tested in wind tunnel.

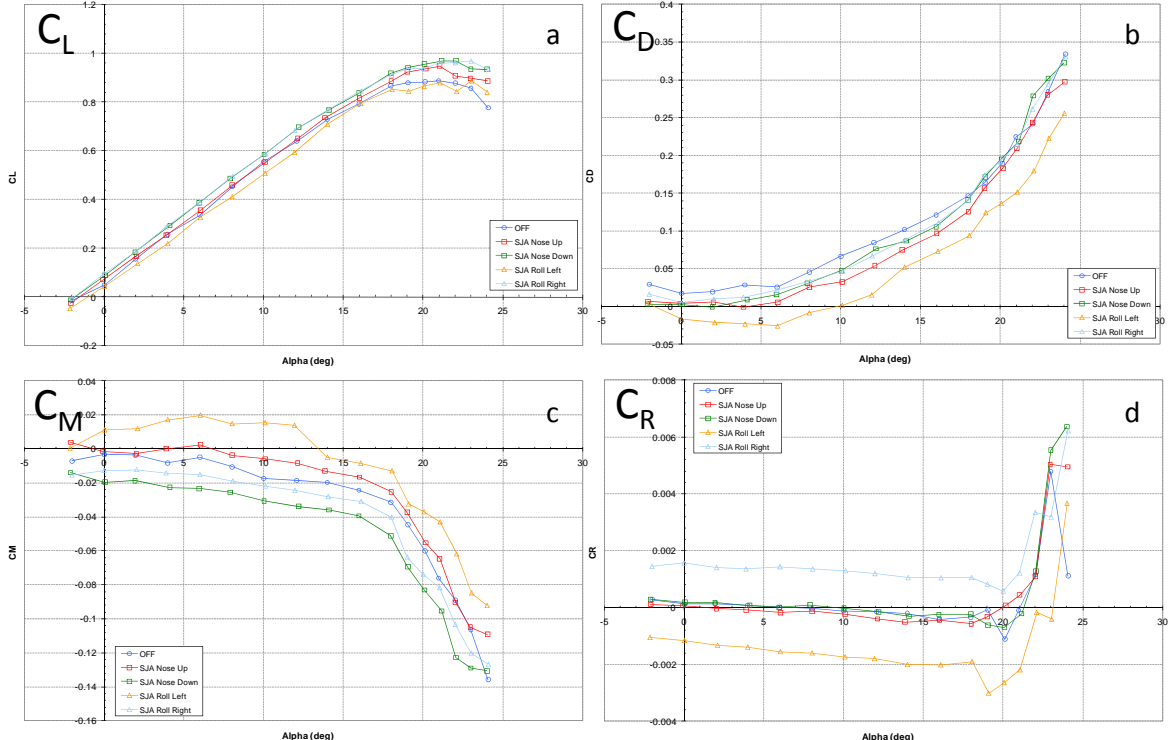


Figure VII.10 Variation with angle of attack of: (a) C_L , (b) C_D , (c) C_M (c), and (d) C_R for the unpowered model

during mild flight maneuvers. Based on these results with the unoptimized actuators, *it is anticipated that further development of the actuator technology specifically for integration on flight platforms would significantly enhance their control authority.*

VII.6 Summary

The flight tests conducted illustrated that flight control can be achieved by controlling the flow physics in the vicinity of trailing edges of the wing of a Dragon Eye UAV. The flight maneuvers demonstrations of the fluidic based flow control actuators included a figure-eight maneuver using synthetic jet-based roll control, and a pitch-up to a powered stall. It should be noted that owing to programmatic budgetary and time constraints, the fluidic actuators were adapted from wind tunnel testing of a 2-D model without further optimization of their aerodynamic performance. Furthermore, weight and power limitations forced significant compromises in the performance of these actuators compared to the devices that were used in the wind tunnel investigations. Nevertheless, even with these limitations, the flight tests demonstrated the utility and potential of fluidic-based flow control.

It is clear that a basic research program such as this MURI Program cannot provide for optimization of new concept configurations, but necessarily focuses primarily on the flow physics. As a basic research complement to the fundamental studies of flow physics and the integrated studies of adaptive control concepts, the flight test experiments conducted during this research program served to provide a constant reminder to all the team members of the necessity of integrating the pursuit of basic research issues with the constraints always imposed by real world and system level realities. This serves to clarify and sharpen the research questions being addressed, as well as to provide constant awareness that the fundamental understanding derived from the research is essential to future optimization efforts.

Finally, it is important to recognize that the present flight test results were achieved by modifying an existing platform rather than by designing a flow control-based flight control system from the ground up. The research team feels that the latter approach will ultimately be the key to the realization of the full potential of flow control for real world applications.

VIII. References

- Abbott, I. and A. Deonhoff, *Theory of Wing Sections*, Dover Publications, Inc. (2006).
- Bisplinghoff, R.L., H. Ashley, and R. L. Halfman, *Aeroelasticity*, Wesley Publishing Company, Inc., Reading, MA. (1955).
- Brzozowski, D. "Rapid modification of the flow field about a free moving airfoil by controlled, trapped vorticity concentrations," 5th AIAA Flow Control Conference (2009).
- Chen, N., J. Chen, J. Engel, S. Pandya, C. Tucker, and C. Liu, "Development and characterization of high-sensitivity bioinspired artificial haircell sensor," Tech. Dig. Solid-State Sensor, Actuator, and Microsystems Workshop, 280 (2006)
- DeSalvo, M. and A. Glezer, "Aerodynamic control at low angles of attack using trapped vorticity concentrations," 3rd AIAA Flow Control Conference. (2006)
- DeSalvo, D. M. & Glezer, A. "Control of Airfoil Aerodynamic Performance using Distributed Trapped Vorticity," AIAA Paper 07-0708 (2007).
- Edwards, J.W., H. Ashley, J. V. Breakwell, J.V. "Unsteady aerodynamic modeling for arbitrary motions," *AIAA J.* **17**, 365-374 (1979).
- Glezer, A. and M. Amitay, "Synthetic jets," *Ann. Rev. Fluid Mech.* **34**, 1-36 (2002).
- Ham, F. and G. Iaccarino, "Energy conservation in collocated discretization schemes on unstructured meshes," *Center for Turbulence Research Annual Research Briefs*, 3-14 (2004).
- Jee, S. K. "Flow Control Simulation with Synthetic and Pulsed Jet Actuator," PhD thesis, The University of Texas at Austin (2010).
- Krijnen, G., R. Boer, T. Lammerink, R. Wiegerink, M. Dijkstra, and J. Baar J., "Arrays of cricket-inspired sensory hairs with capacitive motion detection," 18th IEEE International Conference on Micro Electro Mechanical Systems, 646 (2005).
- Lewin, G. C., H. Haj-Hariri, "Reduced-order modeling of a heaving airfoil," *AIAA J.* **43**, 270-283 (2005).
- Lopez, O. D. "Computational Study of a NACA4415 airfoil using synthetic jet control," PhD thesis, The University of Texas at Austin (2009).
- Lopez, O. D., D. Brozozowski, A. Glezer, and R. D. Moser, "Aerodynamic performance of airfoils with tangential synthetic jet actuators close to the trailing edge," AIAA paper 2009-3674 (2009).
- Muse, J. A., A. T. Kutay, and A. J. Calise, "Novel force control traverse for simulating UAV flight in wind tunnel," AIAA Atmospheric Flight Mechanics Conference (2008).
- Muse, J. A., A. A. Tchieu, A. T. Kutay, R. Chandramohan, A. J. Calise, and A. Leonard, "Vortex model based adaptive flight control using synthetic jets," AIAA Guidance, Navigation, and Control Conference, AIAA, Chicago, Illinois (2009).

- Peters, D.A. “Two-dimensional incompressible unsteady airfoil theory - an overview,” *J. Fluids Struct.* **24**, 295-312 (2008).
- Sears, W.R., “Some aspects of non-stationary airfoil theory and its practical applications,” *J. Aero. Sciences*, **8**, 104-108 (1941).
- Spalart, P. R., S. Deck, M. L. Shur, K. D. Squires, M. K. Strelets, and A. Travin, A. “A new version of detached-eddy simulation, resistant to ambiguous grid densities.” *Theoretical and Computational Fluid Dynamics*, **20**, 181– 195 (2006).
- Spalart, P. R. and S. R. Allmaras, “A one-equation turbulence model for aerodynamics flows,” *La Recherche Aerospatiale*, **1**, 5–21 (1994).
- Tchieu, A. A., A. Leonard, A. T. Kutay, J. A. Muse, and A. J. Calise, “Validation of a low-order model for closed-loop flow control enable flight,” 4th AIAA Flow Control Conference (2008).
- Tchieu, A. A. and A. Leonard, “A discrete-vortex model for the arbitrary motion of a thin airfoil with fluidic control,” *J. Fluids Struct.* (2011, to appear).
- Theodorsen, T., “General theory of aerodynamic instability and the mechanism of flutter,” NACA Technical Report 496 (1935).
- von Kármán, T., Sears, W.R., “Airfoil theory for non-uniform motion,” *J. Aero. Sciences*, **5**, 379-390 (1938).
- Wagner, H., “Concerning the dynamic ascending force formation of aerofoils,” *Z. Angew. Math. Mech.* **5**, 17-35 (1925).

IX. Ancillary Information

IX.1 Personnel Supported

Avishek Aiyar, Graduate Research Assistant, Chemical and Biomolecular Engineering, Georgia Tech

Guy Ben-Dov, Postdoctoral Research Associate, Mechanical Science and Engineering, University of Illinois

Dan Brzozowski, Graduate Research Assistant, Mechanical Engineering, Georgia Tech

Rajeev Chandramohan, Graduate Research Assistant, Aerospace Engineering, Georgia Tech

John Culp, Research Engineer, Mechanical Engineering, Georgia Tech

Michael DeSalvo, Graduate Research Assistant, Mechanical Engineering, Georgia Tech

Uday Godse, Graduate Research Assistant, Mechanical Engineering, UT Austin

Gary Gray, Senior Research Engineer, GTRI

Mike Heiges, Principal Research Engineer, GTRI

Sol Keun Jee, Graduate Research Assistant, Mechanical Engineering UT Austin

Kilsoo Kim, Graduate Research Assistant, Aerospace Engineering, Georgia Tech

Warren Lee, Research Engineer II, GTRI

Seong-Hyok Kim, Research Engineer, Electrical Engineering, Georgia Tech

Ali Kutay, Research Engineer, Aerospace Engineering, Georgia Tech

Omar Lopez, Graduate Research Assistant, Mechanical Engineering UT Austin

Andre Lovas, Senior Research Engineer, GTRI

Jonathan A Muse, Graduate Research Assistant, Aerospace Engineering, Georgia Tech

Julie Siloti Graduate Research Assistant, Institute for Computational Engineering and Sciences, UT Austin

Chao Song, Graduate Research Assistant, Electrical Engineering, Georgia Tech

Andrew A. Tchieu, Graduate Research Assistant, Aeronautics, Caltech

Emile Touber, Graduate Research Assistant, Mechanical Engineering, UT Austin

Nick Traverner, Graduate Research Assistant, Institute for Computational Engineering and Sciences, UT Austin

Steve Williams, Research Engineer I, GTRI

Tansel Yucelen, Graduate Research Assistant, Aerospace Engineering, Georgia Tech

Yanzhu Zhao, Graduate Research Assistant, Electrical Engineering, Georgia

IX.2 Publications

1. A. R. Aiyar, C. Song, S.-H. Kim and M. G. Allen, "An All-Polymer Air-Flow Sensor Array using a Piezoresistive Composite Elastomer," *Smart Materials and Structures*, 18, 115002 (2009)
2. A.R. Aiyar, C. Song, S.H. Kim, M.G. Allen "An All Polymer Air-Flow Sensor Array Using a Piezoresistive Composite Elastomer," in Digest Tech. Papers IEEE MEMS'09 Conference, Sorrento, January 25-29, 2009, pp. 447-450.
3. Brzozowski, D. P., G. Woo, J. R. Culp, and A. Glezer, "Transient Separation Control using Pulse-Combustion Actuation," *AIAA Journal* **48**, 2482-2490 (2010)
4. Brzozowski, D. P. & Glezer, A., "Aerodynamic Closed-Loop Flow Control of A Free-Moving Airfoil Using Trapped Vorticity," Int. Conf. on Jets, and Wakes Berlin, Germany, 2008.
5. Brzozowski, D. P., Culp, J. R., Kutay, A. T., Muse, J. A. & Glezer, A. " Closed-Loop Aerodynamic Flow Control of a Free Airfoil," AIAA Paper 08-4323, 2008.
6. Chandramohan, R., K. Kim, A. J. Calise, and J. Craig, "Modeling of a 3-DOF Dynamic Wind Tunnel Traverse," AIAA Guidance, Navigation, and Control Conference, Toronto, Canada, August 2-5, 2010.
7. Choi, S-O, S. Rajaraman, Y-K. Yoon, X. Wu, and M. G. Allen, "3-D Metal Patterned Microstructure using Inclined UV Exposure and Metal Transfer Micromolding Technology," Tech. Dig. Solid-State Sensor, Actuator, and Microsystems Workshop (Hilton Head 2006), June 2006.
8. Glezer, A., "Aspects of Aerodynamic Flow Control using Synthetic Jet Actuation," *Accepted for publication in the Proceedings of the Royal Society-A*.
9. Haselbacher, A., F. M. Najjar, L. Massa, and R. D. Moser, "Slow-time Acceleration for Modeling Multiple-Time-Scale Problems," *J. Comput. Phys.* **229**, 325-342 (2010).
10. Jee, S. K. "Flow Control Simulation with Synthetic and Pulsed Jet Actuator," PhD thesis, The University of Texas at Austin, 2010.
11. Jee, S. K., O. Lopez, D. P. Brzozowski, A. Glezer, and R. D. Moser, "Delayed Detached Eddy Simulation of Aerodynamic Control with Synthetic Jets," V European Conference on Computational Fluid Dynamics, Lisbon, Portugal, June 14-17, 2010.
12. Jee, S. K., O. Lopez, R. Moser, A. Kutay, J. Muse, and A. Calise, "Flow Simulation of a Controlled Airfoil with Synthetic Jet Actuators," AIAA Paper 2009-3673, 2009.
13. Jee, S. K., O. D. Lopez, R. D. Moser, A. T. Kutay, J. A. Muse, J. and A. J. Calise, "Flow Simulation of Actively Controlled Airfoil with Synthetic Jet Actuators," *AIAA J.*, in preparation 2010.
14. Kim, K., T. Yucelen, and A. J. Calise, "K-Modification Based H2 Adaptive Control," AIAA Guidance, Navigation, and Control Conference, Toronto, Canada, August 2-5, 2010.
15. Kutay, A. T., A. J. Calise, and J. A. Muse, "A 1-DOF wind tunnel experiment in adaptive flow control," AIAA Guidance, Navigation, and Control Conference, 2006.

16. Kutay, A. T., J. R. Culp, J. A. Muse, D. P. Brzozowski, A. Glezer, and A. J. Calise, "A closed-loop flight control experiment using active flow control actuators," 45th AIAA Aerospace Sciences Meeting, 2007.
17. Kutay, A., A. Calise, A. Tchieu, J. Muse, J., and A. Leonard, "Validation of a Low- Order Model for Closed Loop Flow Control Enabled Flight," AIAA-2008-3863, 4th Flow Control Conference, Seattle, Washington, June 23-26, 2008.
18. Lopez, O. D. "Computational Study of a NACA4415 airfoil using synthetic jet control," PhD thesis, The University of Texas at Austin, 2009.
19. Lopez, O. D., D. Brozozowski, A. Glezer, and R. D. Moser, "Aerodynamic Performance of Airfoils with Tangential Synthetic Jet Actuators Close to the Trailing Edge," AIAA paper 2009-3674, 2009.
20. Moser, R. D., N. P. Malaya, H. Chang, P. S. Zandonade, P. Vedula, A. Bhattacharya, A., and A. Haselbacher, "Theoretically Based Optimal Large-Eddy Simulation," *Phys. Fluids*, **21**, 105104, 2009.
21. Muse, J.A., and A. J. Calise, "Vortex Model Based H_∞ Adaptive Flight Control Using Synthetic Jets," AIAA Guidance, Navigation, and Control Conference, Toronto, Canada, August 2-5, 2010.
22. Muse, J.A., and A. J. Calise, " H_∞ Adaptive Control of the Generic Transport Model," AIAA InfoTech Conference, Atlanta, GA, April 20-22, 2010.
23. Muse, J.A., and A. J. Calise, " H_∞ Neural Network Adaptive Control," American Control Conference, Baltimore, MD, June 30-July 2, 2010.
24. Muse, J. A., R. Chandramohan, A. J. Calise, "Vortex Model Based H_∞ -Norm Minimization Approach for Adaptive Flight Control Using Synthetic Jets," AIAA Guidance, Navigation, and Control Conference, Toronto, Canada, August 2-5, 2010.
25. Muse, J. A., A. T. Kutay, D. P. Brzozowski, J. R. Culp, A. J. Calise, and A. Glezer, "Dynamic flight maneuvering using trapped vorticity flow control," 46th AIAA Aerospace Sciences Meeting and Exhibit, 2008 .
26. Muse, J. A., A. T. Kutay, and A. J. Calise, "Adaptive longitudinal control of aircraft using synthetic jets". AIAA Guidance, Navigation, and Control Conference 2007.
27. Muse, J. A., A. T. Kutay, and A. J. Calise, "Experimental Trapped Vorticity Flight Control using an Augmenting Error Minimization Adaptive Law," AIAA Guidance, Navigation, and Control Conference, Honolulu, Hawaii, Aug. 18-21, 2008.
28. Muse, J. A., A. T. Kutay, and A. J. Calise, "A Novel Force Control Traverse for Simulating UAV Flight In A Wind Tunnel," AIAA Atmospheric Flight Mechanics Conference, Honolulu, Hawaii, Aug. 18-21, 2008.
29. Muse, J. A., A. A. Tchieu, A. T. Kutay, R. Chandramohan, A. J. Calise, and A. Leonard, "Vortex model based adaptive flight control using synthetic jets," AIAA Guidance, Navigation, and Control Conference and Exhibit, Chicago, Illinois, August 10-13, 2009.
30. Pan, B., Y.-K. Yoon, G. E. Ponchak, M. G. Allen, J. Papapolymerou, and M. M. Tentzeris,

- “Analysis and Characterization of a High-Performance Ka-Band Surface Micromachined Elevated Patch Antenna,” *Antennas and Wireless Propagation Letters*, **5**, 511–514 (2006)
31. Rajaraman, S., S.-O Choi, R. H. Shafer, J. D. Ross, J. Vukasinovic, Y. Choi, S. P. DeWeerth, A. Glezer, and M. G. Allen., “Microfabrication technologies for a coupled three-dimensional microelectrode, microfluidic array,” *Journal of Micromechanics and Microengineering*, **17**, 163-171 (2007)
 32. Rajaraman, S., Y. Zhao, X. Wu, S.-H. Kim, and M. G. Allen, “Metal Transfer Micromolding (MTM) Process for High-Aspect-Ratio 3-D Structures with Functional Metal Surfaces,” presented in International Symposium on Flexible Automation (ISFA 2008), Atlanta, USA, June 2008.
 33. Song, C., A. R. Aiyar, S.-H. Kim and M. G. Allen “Exploitation of Aeroelastic effects for Drift Reduction in an All-Polymer Air Flow Sensor,” in Digest Tech. Papers IEEE TRANSDUCERS 09 Conference, Denver, Colorado, June 21-25, 2009, pp1545-1548.
 34. Song, C., A. R. Aiyar, S.-H. Kim, and M. G. Allen, “Exploitation of Aeroelastic Effects for Drift Reduction, in an All-Polymer Air Flow Sensor,” in press, *Sensors and Actuators A*
 35. Tchieu, A. A., A. Kutay, J. A. Muse, A. J. Calise, and A. Leonard, "Validation of a Low-Order Model for Closed-Loop Flow Control Enable Flight," 38th AIAA Fluid Dynamics Conference and Exhibit AIAA, 2009.
 36. Volyanskyy, K. Y., W. M. Haddad, and A. J. Calise, “A New Neuroadaptive Control Architecture for Nonlinear Uncertain Dynamical Systems: Beyond σ - and e -modifications,” *IEEE Transactions on Neural Networks*, **20**, 1707-1723 (2009).
 37. Yoon, Y.-K., and M. G. Allen, “Proximity Mode Inclined UV Lithography,” Tech. Dig. Solid-State Sensor, Actuator, and Microsystems Workshop (Hilton Head 2006), June 2006.
 38. Yoon, Y.-K., J.-H. Park, and M. G. Allen, “Multidirectional UV lithography for complex 3-D MEMS structures,” *IEEE Journal of Microelectromechanical Systems*, **15**, 1121-1130 (2006)
 39. Yucelen, T. and A. J. Calise, “Derivative Free Model Reference Adaptive Control,” AIAA Guidance, Navigation, and Control Conference, Toronto, Canada, August 2-5, 2010.
 40. Zhao, Y., S.-H. Kim, Y. Li, B. Pan, X. Wu, E. M. Tentzeris, J. Papapolymerou, and M. G. Allen, “A Micromachined Airflow Sensor Based on RF Evanescent-Mode Cavity Resonator,” presented in Tech. Dig. International Microwave Symposium (IMS 2008), Atlanta, USA, June 2008.
 41. Zhao, Y., Y. Li, B. Pan, S.-H. Kim, Z. Liu, M. M. Tentzeris, J. Papapolymerou, and M. G. Allen, “RF evanescent-mode cavity resonator for passive wireless sensor applications,” *Sensors and Actuators A*, **161**, 322-328 (2010)
 42. Zhao, Y., Y.-K. Yoon, and M. G. Allen, “Metal-Transfer-Micromolded RF Components for System-On-Package (SOP),” Proc. 57th IEEE Electronic Components and Technology Conference, Reno, NV, May 2007.
 43. Zhao, Y., Y.-K. Yoon, X. Wu, and M. G. Allen, “Metal-Transfer Micromolding of Air-Lifted RF Components,” Proc. 14th International Conference on Solid-State Sensors, Actuators and Microsystems (Transducers '07), Lyon, France, June 2007.

IX.3 AFRL Points of Contact

Greg Abate AFRL/MNGN, Eglin AFB

Gary Dale, AFRL/VAAA, Wright-Patterson AFB

Johnny Evers, AFRL/MNGN, Eglin AFB

Michael Ol, AFRL/AV, Wright-Patterson AFB

Richard Rivir, AFRL/PR, Wright-Patterson AFB

IX.4 Transitions

None

IV.5 Honors & Awards Received

Calise, A. J., 2010 AIAA Guidance, Navigation and Control Award

Leonard, A., 2010 Member, the National Academy of Engineering